Politecnico di Milano
Department of Aerospace Science and Technology
Doctoral Programme in Aerospace Engineering

Enhanced autonomy in GNC for spacecraft with limited observability operating in lunar environment

Doctoral Dissertation of:
Giovanni Zanotti

Supervisor:
Prof. Michèle Lavagna

Tutor:
Prof. Sergio Ricci

Coordinator:
Prof. Pierangelo Masarati

Year 2022 – Cycle XXXV

Abstract

Autonomy in spacecraft Guidance, Navigation & Control (GNC) is an ever-growing topic in both academic and industrial research, due to the vast possibilities that it can enable in terms of mission concepts and operational costs. The work presented in this thesis explores different strategies to support the enhancement of on-board autonomy in the GNC tasks in view of the future challenges that the lunar environment will present, considering scenarios without complete observability imposed by reduced sensor utilisation or by the constraints of a small-sized navigation constellation. Three different scenarios are investigated, studying, implementing and testing GNC architectures to address the problem of spacecraft autonomy in various dynamical conditions of proximity manoeuvring, natural motion and landing.

The objective of pushing towards spacecraft autonomy is indeed a key point to unlock the exploitation of more intelligent and adaptive platforms, which, related to the tendency to move more and more towards distributed and smaller systems, needs to be deeply investigated. Such approach, entailing small satellites in constellations or formation flying contexts, provide cheaper and more versatile solutions in general, but not in the operational costs, unless a higher level of autonomy is given to the systems. The GNC tasks are deeply involved in this considerations, recalling that the state-of-the-art for most of the spacecraft is to completely rely on ground intervention to run the Flight Dynamics routines, i. e. performing the Orbit Determination (OD) and scheduling and commanding the required orbital manoeuvres. The exploitation of small platforms however is accompanied, in general, with reduced sensor

suites and computational power, reason for which specific low-observability navigation techniques are to be targetted, relevant also for larger platforms in contingency scenarios.

The next decades of space exploration will also be deeply influenced by the renewed interest in the Moon, target of many international programmes aiming at providing the basis for a stable human presence in this environment. Such activities will provide both scientific and technological advancements in the understanding of our natural satellites and in our capability to survive and remain on its surface. Two promising infrastructures that are currently being studied with joint international efforts are the Lunar Orbital Platform - Gateway (LOP-G) and a communication and navigation constellation around the Moon.

The former project will be a new orbital outpost to host astronauts in the cislunar environment. In particular the chosen trajectory on a Near Rectilinear Halo Orbit (NRHO) will represent an interesting playground for the validation of some autonomous relative GNC algorithms needed by possible chasing spacecraft looking to either reach the Gateway or fly in formation cooperatively with it. A lunar constellation will instead be a great opportunity in particular to increase the autonomy from ground-based navigation for both surface and orbital users, resulting in a lunar-centric Global Navigation Satellite System (GNSS) service.

The work presented in this thesis focuses on considering these two infrastructure as opportunities to study Earth-autonomous GNC strategies, which can contribute to the exploitation of such potential. Two scenarios of spacecraft flying in proximity to the LOP-G are presented first, where two missions of autonomous rendezvous and manoeuvring in formation flying are considered. The associated GNC schemes have been analysed considering a limited observability scenario where only relative angular measurements are retrieved to perform navigation. The recorded performance is promising and showing the boundaries of applicability of performing complex and mission critical tasks with such estimation architecture. The third scenario instead provides first a strategy to help the design of a small-sized lunar constellation, entailing different objectives and users to assist. Then, various optimised constellations are tested including the orbital and landing users' filtering architectures, extracting insights on the state estimation achievable and its capability to support critical GNC tasks. The results obtained showed navigation capabilities good enough to enable correct execution of missions in the low lunar orbital region including the complex task of performing a controlled landing at the South Pole. To provide a higher formulation robustness, the filters involved have been also deployed and run on embedded hardware, validating their implementation through Processor-In-the-Loop (PIL) testing.

Table of Contents

List of Figures

List of Tables

List of Acronyms

BO Bearing Only

CAM Collision Avoidance Manoeuvre

CR3BP Circular Restricted Three-Body Problem

CW Clohessy-Wiltshire Model

DOF Degrees of Freedom

DOP Dilution of Precision

DRO Distant Retrograde Orbit

EKF Extended Kalman Filter

ELFO Elliptical Lunar Frozen Orbit

FF Formation Flying

FoV FoVField of View

GNC Guidance, Navigation & Control

GNSS Global Navigation Satellite System

h-FoV half Field of View

IMU Inertial Measurement Unit

INS Inertial Navigation System

IP Image Processing

ISS International Space Station

KF Kalman Filter

KOZ Keep-Out Zone

LEO Low Earth Orbit

LLO Low Lunar Orbit

LOP-G Lunar Orbital Platform - Gateway

LoS Line-of-Sight

MIL Model-In-the-Loop

MOO Multi Objective Optimisation

MPC Model Predictive Control

NLP Nonlinear Programming

NRHO Near Rectilinear Halo Orbit

OBC On-Board Computer

OD Orbit Determination

ODE Ordinary Differential Equation

Ph.D. Philosophiae Doctor

pdf probability density function

PID Proportional Integral Derivative

PIL Processor-In-the-Loop

PVT Position Velocity Timing

QP Quadratic Programming

QPT Quasi Periodic Torus

RF Radio Frequency

RKF78 Runge-Kutta-Fehlberg 7(8)

RMSE Root Mean Squared Error

RSS Root of the Sum of the Squares

SoC System on Chip

SQP Sequential Quadratic Programming

SRP Solar Radiation Pressure

STM State-Transition Matrix

ToA Time of Arrival

ToF Time of Flight

TRL Technology Readiness Level

UKF Unscented Kalman Filter

UT Unscented Transformation

CHAPTER 1

Introduction

Relieving the effort required by the Ground Segment in future space missions leads to the necessity of moving some tasks of the Guidance, Navigation & Control chain, typically performed by Flight Dynamics operators, to the On-Board Computers (OBCs) of the Space Segment. Indeed increasing spacecraft on-board autonomy is a prominent step forward for the research community, finding much room for improvement in particular for the navigation tasks, still heavily relying on Earth support for OD. More specifically, the reduction of Ground Segment dependence can provide increased flexibility and versatility to space missions, improving both performance and responsiveness of the spacecraft while reducing the operational costs. Providing this level of autonomy means integrating different factors together, comprising mathematical, algorithmic and also hardware concepts, which represent a complex challenge to be faced from multiple standpoints.

In particular this is accompanied by a strong interest in the exploitation of distributed space systems, witnessed also by the more and more arising mission concepts relying on proximity operations. Among these we find both multiple *cooperative* spacecraft and single probes orbiting *uncooperative* objects, such

as a small solar system body or a space debris. Moreover, the opportunity to exploit smaller, thus cheaper, platforms acting together as agents unleashes multiple mission concepts possibility for constellations [1] or formations [2, 3, 4]. To benefit from such high versatility, the on-board avionics shall be capable of handling the complexities that the harsh environment poses to the system, reacting in coordination with the other agents involved. The conditions of reduced observability is also another relevant aspect to consider, when e. g. small satellites are involved or in contingency scenarios, where the sensing capabilities may be limited.

Among the mission scenarios that have regained considerable attention in the last decade by the international community the lunar environment is surely one of the most promising and studied. The 20s and 30s of the 21st century will be characterised by a huge quantity of missions involving the Moon, with the goal of advancing both scientific and engineering understandings of this environment. In particular, an international effort is being invested on the Lunar Orbital Platform - Gateway [5], the future human outpost in the cislunar space, which will have a critical role as a long-term modular infrastructure, to support many different missions both around and on the Moon. The lunar Gateway will fly a Near Rectilinear Halo Orbit, which is considered as the most suitable orbital regime due to many different aspects, as reported in [6], such as a high stability against perturbation, high accessibility from Earth and towards Moon surface and continuous Earth visibility.

The foreseen activities involving the LOP-G will entail various space transportation systems to deliver cargo, experiments, logistics and also humans. To allow accomplishment of such assembly and re-supply missions, the capability to perform autonomous rendezvous and docking/undocking manoeuvres in the most safe manner is of primary importance. Particularly, a strong effort in the development of the GNC subsystem is required, in order to transport the knowledge and experience gained for similar missions in Low Earth Orbit (LEO), as heritage of the International Space Station (ISS) programme, to the more complex dynamics of the cislunar space. The multi-body gravitational regime provides indeed more complexities with respect to the simpler two-body relative dynamics both dynamically and mathematically considering the governing equations which, in general do not present closed form solutions and presents also chaotic behaviours [7, 8, 9] for which small deviations in the initial conditions of a spacecraft grow exponentially, leading to completely different outcomes. Studies on relative GNC in such multi-body gravitational environment have been started only recently (see e. g. [10, 11, 12]), and the need to further extend this topic is paramount, investigating both rendezvous and formation flying scenarios.

A complementary scenario in the challenging roadmap of the Moon exploration entails many different missions that will visit the lunar proximity, with particular attentions to LLO spacecraft and surface assets such as landers, rovers and even humans [13]. Moreover, due to some specific features of the orography and mineralogy, the South Pole region will be for certain one of the most targeted spots on the surface [14, 15]. In such perspective, another interesting infrastructure that may rely on a joint international effort consists in a constellation of lunar orbiters to provide communication and navigation services to the just mentioned missions. Such constellation would be revolutionary in enabling many concepts requiring either real-time communication with Earth or continuous precise positioning on-board. In particular providing good Earth-independent navigation functions to the orbital users or to landers is one of the major challenges that may enhance the level of autonomy for such class of missions, reducing also the associated costs. Previous studies in similar topics evaluated the benefits of exploiting Earth based GNSS infrastructures for lunar missions (see [16, 17, 18]), but the objective of designing a dedicated lunar constellation is only recently emerging. Many studies in this context are being funded by the space agencies, with the goal of validating this concept and supporting its realisation, involving two different topics. First, the orbital design of the constellation to fulfil different constraints and different performance associated to the various users involved (e. g. orbital and surface users) is a fundamental step. To this end, given the still early stage in which such studies are, the overall requirements are not fully defined, meaning that this step requires a high flexibility. Secondly, considering the navigation service required for the autonomy enhancement, the associated technology both hardware and software are to be designed, targetting specific performance for both servicers [19] and users. As such, it is important to study the best navigation architecture to consider on-board the potential users, fusing information coming from different likely sensors to be found on-board.

1.1 Research objectives

In the presented context, this thesis' work humbly tries to perform advancements in the GNC strategies to move steps forward in the definition of the required building blocks for the challenges posed by the Moon exploration roadmap. In particular the following high-level question is posed.

Which are the navigation performance of autonomous GNC algorithms in the lunar gravitational environment achievable relying on *reduced observability* and *computational demand*?

The research objective is thus the definition and integration of GNC architectures that exploit limited observability and computational capabilities, to be applied to different dynamically challenging scenarios.

- Rendezvous (Scenario A) and formation flying (Scenario B) with LOP-G employing Line-of-Sight (LoS) only measurements.
- Moon Orbiter and Lander with a small-sized lunar GNSS constellation (Scenario C).

The first two scenarios analysed involve the proximity dynamics with respect to the LOP-G platform, considering two different missions to accomplish that require complex understanding of the system under investigation. In both cases a cooperative approach is forsaken, involving the lunar Gateway passing its current state through a communication link between the two systems. To accomplish the execution of the required manoeuvres, the navigation task of the chaser is performed autonomously on-board involving only LoS angular measurements obtained by a simple camera.

Exploiting only two scalar measurements, such as the angle- (or *bearing-*) only does, the complete state of a spacecraft is not observable, thus the application of a navigation filter in a completely free dynamics does not provide acceptable results. Recent studies [20, 21] proved the concept of a BO guidance and navigation scheme as applied for rendezvous in the LEO environment. Such strategy rely on the concept that by introducing some thrusting actions it is possible to modify the angular measurement history and thus to resolve the state ambiguity. One of the first goal of this research, pursued through Scenario A is to investigate the validity of such strategy in the more complex dynamical regime of the cislunar space, entailing a rendezvous problem with the LOP-G platform.

Scenario A

- How does the basic BO guidance and navigation formulation perform in the LOP-G scenario?
- Is it possible to improve the basic scheme by enhancing the observability in a more effective and efficient way?
- Can the computational demand be reduced?
- Can this concept be extended also to heterogeneous orbits? Which is the relevance of the relative geometry of the problem with respect to the navigation performance?

The analysis of Scenario A tries to answer such questions, analysing different mathematical formulations of the algorithms involved in the GNC scheme and gaining relevant insights on the BO strategy.

The second scenario, Scenario B, wants to expand the already obtained knowledge to a more general case, where the relative dynamics does not impose a reducing distance, but the two platforms remain in a bounded relative motion. In particular, the first block of the analysis regards the definition of an optimal autonomous guidance and control scheme, used to perform reconfiguration manoeuvres in a formation flying scenario. The objective is to derive a strategy that pushes farther the set of analysed cases in autonomous formation flying strategy for GNC. The resulting controlled trajectory is relatively challenging from the dynamical point of view, involving a higher complexity that requires more stringent navigation performance. The step forward is thus to include the BO guidance strategy also in this scenario, understanding if it may be feasible to correctly finalise the manoeuvres. The associated research questions are here summarised.

Scenario B

- Which set of guidance and control algorithms can be applied to perform efficient rephasing manoeuvring in a formation flying scenario with the LOP-G?
- Can this framework be expanded to be more versatile and adaptive for a large set of transfers?
- Can it include also constraints involving platform related and safety aspects?
- Can we use BO guidance to reach the targetted navigation requirements if employing only angular measurements?

The two previous scenarios analysed the problem of relative navigation, employing indeed relative measurements with respect to the leader spacecraft identified as the LOP-G. The last analysed scenario tries to deal with the complementary problem of absolute navigation in the lunar environment. The employed technique of a GNSS constellation presented here wants to expand the very well consolidated knowledge of the navigation algorithms used with the Earth GNSS assets, a different setup, where not only the environment is dynamically more complex, but also the constellation size in extremely reduced, imposing an overall reduction of the continuous visibility that the Earth-based constellation is capable of. The goal here is to explore the set of possibilities within the search space of Keplerian orbiters to obtain good performance for both surface and orbital users, presenting a optimisation strategy to perform the constellation design, keeping in mind also operational constraints.

The additional complexity associated in computing the navigation performance of orbital users is given by the fact that the typical Dilution of Precision (DOP) indexes are not sufficient in this case to give a complete overview of the scenario. Indeed orbital users, specifically landers, due to the dynamics their are subject

to, in order to provide on-board state estimation rely on navigation filters. The objective of this scenario is thus to develop the navigation scheme used by generic potential orbital users to exploit robustly and at the most the GNSS services provided by the lunar constellation. To this end, standard navigation filters are here exploited in a GNSS/INS configuration, with the aim of gaining a high sensitivity in their behaviour for the unexplored scenario under evaluation, where long period windows without measurements are present. Such sensitivity is forsaken for both orbital user in natural dynamics first, considering only the N part of the GNC scheme and then increasing the complexity with a more challenging landing mission, where the full GNC chain is excited.

An additional research objective is to compare different filter formulations in order to understand how the performance is affected by the filter formulation and how they compare from a computational standpoint. More in detail, the latter consideration is performed by performing PIL tests, in order to compare the filter on a relevant embedded computational environment, aiming also at validating the proposed architecture and considering the feasibility to exploit it on relevant space-representative hardware.

Scenario C

- How to design a Lunar GNSS constellations with reduced size and with different users to assist?
- How can this be translated to final users on-board performance? Which is the best formulation of an objective function to provide good orbital users navigation?
- Can the user navigation benefit by including optical measurements of the servicers' LoS?
- How does this strategy perform for a landing spacecraft? Is the navigation good enough to obtain a good controlled trajectory?
- Which is the best formulation in terms of filter and integration method to be implemented on-board, considering the navigation performance and the computational demands?
- Is this formulation viable for the embedded execution on relevant hardware? Are there any limitations in the resources utilisation?

All these questions are addressed deeply with the analyses proposed in the following chapters.

1.2 Thesis Overview

The roadmap with the different case studies involved is presented in Fig. 1.1, where the three scenarios investigated are detailed in the different analysis steps.

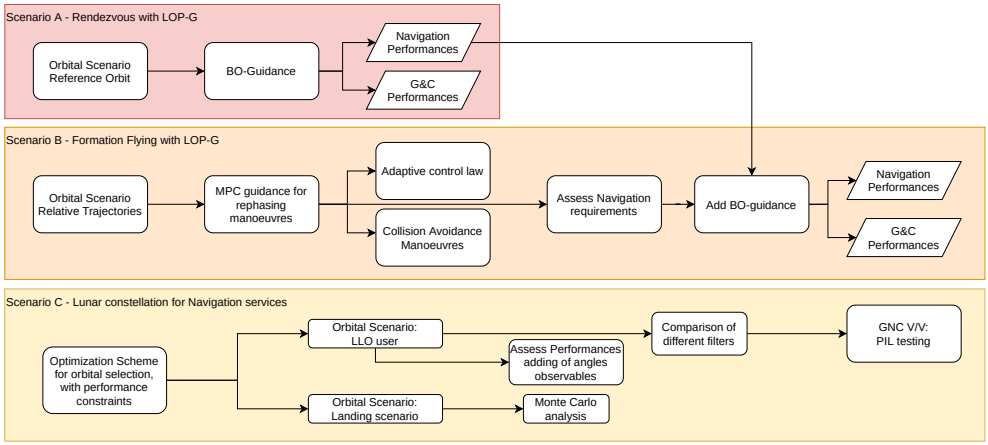

Figure 1.1: Analysed scenarios roadmap.

The presentation of the topics, the mathematical and algorithmic implementation they require and the results obtained are organised in this thesis with the following structure.

Chapter 2 has as main objective the definition of the basic foundations that are needed in the rest of the thesis. First of all, different dynamical representations are presented, including gravitational models, perturbation terms and both absolute and relative formulations. Then after providing a brief overview of the basics of general GNC architectures, some background in the domains of Navigation first and Guidance & Control after are given, with reference on state-of-the-art techniques and with emphasis on the strategies that are the employed in this work.

The basic problem of state estimation filtering is analysed in Chapter 3, where after introducing the different alternatives available to design a navigation filter, the formulation to derive filters of the Kalman family is presented, together with the algorithmic representation of the most relevant ones. Then the different measurement models employed over the analysed scenarios are described.

The two following chapters represent the main core of the thesis' work, presenting the three scenarios analysed. Chapter 4 comprehends the two GNC studies in the cislunar environment, i. e. the rendezvous case and the formation flying one, where two similar strategies to include the BO GNC are highlighted. The operational conditions are first presented and then, for both scenarios, the implementation of the respective algorithms is detailed, providing the rationale behind the different choices. The results are then showed and critically analysed, drawing relevant conclusion on the applicability of such strategies.

Chapter 5 provides instead the details of the analysis proposed by the third scenario concerning the GNSS constellation to support the navigation of LLO users. The strategy of the constellation orbital design through an optimisation procedure is presented and the results shown. The multiple resulting optima are compared first in orbital geometry, and then in the performance able to provide to different users, both orbiting and landing. After that, different filter formulations are compared in navigation and computational performance employing also PIL tests.

The final Chapter 6 tries to sum-up the relevant contributions that this work has provided, recalling the research questions and objectives that this introductory chapter posed. Additional insights on possible extensions of this research are also discussed, in order to spread what could drive new interesting ideas to be explored.

1.3 Bibliographic Disclaimer

The work presented in this thesis is the results of three years of Ph.D., during which different research activities were carried out. When the opportunity made it possible, the products of these activities have been published either on conference or journal papers. As such, some parts of this thesis have already been presented in previous articles, reported in the following list.

- **Giovanni Zanotti**, Andrea Pasquale, Jacopo Prinetto, and Michèle Lavagna. *High performance lunar constellation for navigation services to Moon orbiting users.* Advances in Space Research, 2022 (under review).
- Andrea Capannolo, **Giovanni Zanotti**, Michèle Lavagna and Giuseppe Cataldo. *Model predictive control for formation reconfiguration exploiting quasi-periodic tori in the cislunar environment.* Nonlinear Dynamics, 2023. doi: `https://doi.org/10.1007/s11071-022-08214-8`
- Andrea Pasquale, **Giovanni Zanotti**, Jacopo Prinetto, Michele Ceresoli and Michèle Lavagna. *Cislunar Distributed Architectures for Communication and Navigation Services of Lunar Assets.* Acta Astronautica, 2022. doi: `https://doi.org/10.1016/j.actaastro.2022.06.004`
- Michele Ceresoli, **Giovanni Zanotti** and Michèle Lavagna. *Bearing-only Navigation for Proximity Operations on cislunar non-Keplerian orbits.* 72nd International Astronautical Congress – IAC 2021, Dubai, UAE, 2021. url: `https://hdl.handle.net/11311/1191262`
- Michele Ceresoli, **Giovanni Zanotti** and Michèle Lavagna. *Bearing-Only Navigation to Support Proximity Operations on Cislunar Non-Keplerian Orbits.* 16th International Conference on Space Operations –

SpaceOps 2021 Virtual Edition, 2021. url: https://hdl.handle.net/11311/1196946

- **Giovanni Zanotti** and Michèle Lavagna. *Science opportunities in the Didymos binary: the role of post-impact ejecta long-term dynamics in the proximity operations definition.*. 71st International Astronautical Congress – IAC 2020, Cyber Space Edition, 2020. url: https://hdl.handle.net/11311/1166180

CHAPTER 2

Background & State of Art

The study of Guidance Navigation and Control algorithms for spacecraft requires many different blocks to be designed, implemented and tested. Such techniques rely indeed on a strong mathematical construct, covering different physics and engineering topics.

First, given that the systems under study evolves in a specific dynamical environment, it is necessary to gain the capability to model the orbital motion of spacecraft. In particular it is fundamental to have reliable models for the motion at different levels of complexity and accuracy. Indeed, high-fidelity representations of the dynamical system are needed to simulate the trajectories and other system-related parameters to act as the reference *real world* representation or, as called in navigation jargon, the *ground truth*. These models are however usually very complex and computationally demanding, reason for which their implementation on the GNC algorithms may be prohibitive, considering also the on-board capabilities. As such, it is necessary also to use simpler models to this purpose, knowing solidly which are their accuracies and limitations.

Concerning the engineering aspects instead, a deep knowledge in *Control System Theory* is also required for the design, evaluation and testing of the techniques used in the GNC domain. The success of the overall implementation rely profoundly on aspects such as effectiveness, stability and robustness of the algorithms implemented.

The goal of this chapter is to provide the foundations onto which the three analysed scenarios of the thesis are based, both in terms of mathematical modelling and of the different GNC strategies used. The chapter is organized as follows: Section 2.1 presents the dynamical models that are used in the analysis of motion within the lunar environment. After that, Section 2.2 presents a background of the main GNC techniques used by lunar missions, considering both standard and well investigated schemes and more advanced and young technique, dividing the Navigation task in Subsection 2.2.1 from the Guidance and Control tasks 2.2.1.2. Peculiar attention is posed to the BO problem, the GNSS based navigation and the MPC algorithm, given the strong utilisation of such techniques in the current work.

2.1 Dynamical Models

In the following the main physical formulations of the dynamical models used throughout the thesis are presented.

2.1.1 Gravitational models

To describe the motion of a spacecraft with a negligible mass with respect to some central body, $\mathcal{P}_k$ accounting for multiple gravitational sources, the relative formulation of the *Restricted N-Body Problem* (RnBP) is expressed as

$$\ddot{\mathbf{r}}_{ki} = -\frac{\mu_k}{r_{ki}^3}\,\mathbf{r}_{ki} + \sum_{\substack{j=1 \\ j\neq i,k}}^{\mathrm{N}} \mu_j \left(\frac{\mathbf{r}_{ij}}{r_{ij}^3} - \frac{\mathbf{r}_{kj}}{r_{kj}^3} \right) \tag{2.1}$$

where the motion of the spacecraft $\mathcal{P}_i$, with respect to the central body $\mathcal{P}_k$, under the gravitational influence of the point masses $\mathcal{P}_j$ is modelled.

If the relative position vector $\mathbf{r}_{kj}$, that represents the location of the j-th perturbing body with respect to the central body is obtained from high fidelity ephemerides, the RNBP is reduced to the *Ephemeris Restricted N-Body Problem* (ERNBP). In this work, NAIF's SPICE library [22] is exploited and DE440 ephemerides are used, whereas the relative position vector $\mathbf{r}_{ij}$ is computed by vector subtraction as

$$\mathbf{r}_{ij} = \mathbf{r}_{kj} - \mathbf{r}_{ki} \tag{2.2}$$

and represents the location of the perturbing body $\mathcal{P}_j$ with respect to the object of interest, $\mathcal{P}_i$.

Particular scenarios arise from specific (low) values for the number of attractors. For $N = 2$ we retrieve the simple Keplerian solution of the *Restricted Two-Body Problem* (R2BP), with the classical closed form solution of the orbital trajectories.

If the number of attractor increases, to gain more useful insights on the resulting trajectories, the exploitation of a non-inertial reference frame comes to help. The best choice is to use the *Synodic Reference Frame* co-rotating with the two

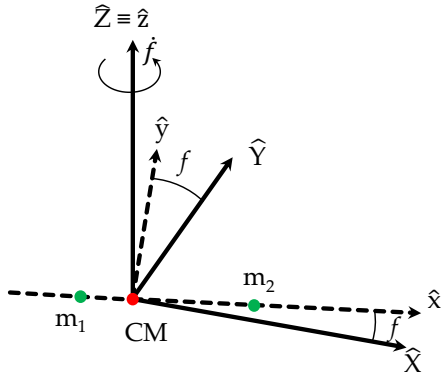

Figure 2.1: Representation of the Inertial reference frame $\hat{X}\hat{Y}\hat{Z}$ and the Synodic reference frame $\hat{x}\hat{y}\hat{z}$.

bodies as shown in Fig. 2.1. In the figure, $\hat{X}\hat{Y}\hat{Z}$ is the inertial frame, while $\hat{x}\hat{y}\hat{z}$ is the synodic frame. m_1 and m_2 are the masses of the two considered attractors and CM is their centre of mass, origin of both reference frames. The synodic frame is constructed with the $\hat{x}$-axis aligned with the m_1 to m_2 direction, the $\hat{z}$-axis parallel to the angular velocity vector of the system and the $\hat{y}$-axis to complete the right-hand frame.

Besides the most general case, the two bodies may be considered to follow a Keplerian motion with a fixed angular velocity direction and f corresponding to the true anomaly of the orbit.

Additional insights are obtained by performing the following adimensionalisation procedures.

- The unitary length is defined as the current distance between the two bodies, $L^* = d_{12}(t)$.
- The unitary mass as the total mass of the two bodies, $m^* = m_1 + m_2$.

- The unitary time as inverse of the mean motion, $t^* = 1/n_{12}$, such that the period of the orbit is equal to 2π.

2.1.1.1 Circular Restricted Three-Body Problem

The most known formulation exploiting this setup is the CR3BP, where the two bodies follow a circular motion about their barycentre. The angular velocity of the synodic frame is constant, equal to n_{12}, and the true anomaly f grows linearly with time, whose adimensional quantity represents the independent variable.

The geometry of the system in the $\hat{x}\hat{y}$ plane of the synodic frame is reported in Fig. 2.2. Here $\mathbf{r} = [x \quad y \quad z]^T$, $\mathbf{r_1}$ and $\mathbf{r_2}$, are the position vectors from the barycentre, the primary and the secondary respectively.

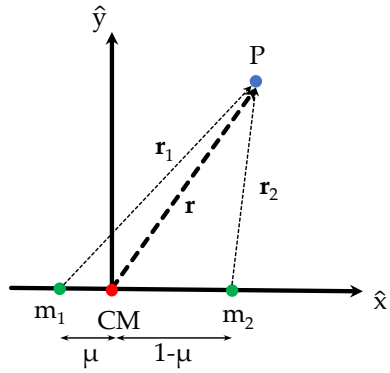

Figure 2.2: Geometric representation of the CR3BP in the $\hat{x}\hat{y}$ plane of the synodic frame. The notation is trivially self-explained.

Following the work in [23], the equations of motion can be simply cast into Eq. (2.3), where the dots represent derivatives with respect to the adimensional time, r_1 and r_2 are the distances from the particles to the primary and secondary attractors, as in Eq. 2.3,

$$\begin{cases} \ddot{x} - 2\dot{y} = U_x \\ \ddot{y} + 2\dot{x} = U_y \\ \ddot{z} = U_z \end{cases} \tag{2.3}$$

with the definition of the gravitational potential function given in Eq. (2.4), useful to define its partial derivatives.

$$U(x, y, z) = \frac{1}{2}(x^2 + y^2) + \frac{1-\mu}{r_1} + \frac{\mu}{r_2} + \frac{1}{2}\mu(1-\mu) \tag{2.4}$$

The only parameter characterising the system is the mass parameter μ and no explicit dependence on time is present in the equations of motion, thus classifying the CR3BP as an *autonomous system*.

2.1.1.2 Irregular gravity fields

A relevant perturbation that may play a role in the dynamical system is caused by the non-uniformity of the gravitational potential. This effect may be fundamental in scenarios considering irregular bodies such as asteroids, but also for low altitude orbits around larger planetary bodies, such as a Moon scenario. Indeed, near the surface of the body, the point mass gravity model introduces high and not negligible errors.

To include such effects, different approaches are possible for the modelling of, entailing various levels of accuracy and consequently computational expensiveness. The most relevant models are here recalled.

- *Ellipsoid.* This model presented in [24] assumes the attractor as a triaxial ellipsoid with constant density. This method requires only the three axes of the ellipsoid and the mean density of the body.
- *Harmonic Expansion.* The shape of the body, or directly the gravitational potential function, is represented using spherical harmonic functions of increasing order. The coefficients of the expansion and the mass are the required parameters. Good references of the method are found in [25, 26]. The mathematical representation of the gravitational potential can be expressed as per Eq. 2.5.

$$U_{\text{she}} = \frac{\mu}{r} + \frac{\mu}{r} \sum_{n=2}^{N} \sum_{m=0}^{n} \left(\frac{R_0}{r} \right)^n \Big[C_{nm} \cos(m\lambda) + S_{nm} \sin(m\lambda) \Big] P_{nm}(\cos\theta) \tag{2.5}$$

  where here μ is the gravitational parameter of the central body, r the distance to the centre of mass of the body, λ the longitude, θ the co-latitude, R_0 a reference radius, $P_{nm}(x)$ are Associated Legendre Functions, while C_{nm} and S_{nm} are Stokes coefficients.
- *Polyhedron.* In this method, the shape of the attractor is based on a single, or a set of, constant density polyhedron, defined by an arbitrary number of nodes and faces. The procedure can be seen in [27, 28], where the presented algorithm needs the polyhedron shape model of the object and the associated mass or density.

To include this effects in the equations of motion, the obtained gravitational potential can be directly used in the right-hand side of the dynamics.

Comparing the three methods it is important to state that the number of faces/nodes and of orders included for the polyhedron and spherical harmonics methods respectively are fundamental in the accuracy vs speed trade-off.

For the Moon scenario relevant for this thesis, the harmonic expansion model provides good accuracy for a discretely high order (e. g. truncation errors $< 1\,\mathrm{mm\,s^{-2}}$ for a 30x30 model), requiring reasonably low computation times to easily simulate the environment.

2.1.2 Solar Radiation Pressure

The only non-gravitational perturbation term that is considered in the work is the Solar Radiation Pressure (SRP). Its acceleration, directed in the anti-Sun direction, shows a magnitude that can be described as presented in [29], as in Eq. 2.6.

$$a_{SRP} = \frac{S_\odot}{c}\frac{(1\mathrm{AU})^2}{d_\odot^2}c_R\frac{A_\odot}{m} \tag{2.6}$$

In this equation, $S_\odot = 1367\,\mathrm{W\,m^{-2}}$ is the Sun mean flux at 1AU, $c = 299\,792\,458\,\mathrm{m\,s^{-1}}$ the speed of light, $d_\odot$ the Sun-point distance, c_R the reflectivity and $A_\odot$ the cross-sectional area of the body exposed to the SRP. The reflectivity coefficient vary from 0 for a completely transparent object to 2 for a fully reflective one. Note that this acceleration depends on both the mass and the geometrical extension of the body, differently from gravitational terms.

This simplified *cannonball* model for SRP is useful since it avoids the dependence of orbital dynamics on the spacecraft attitude which would have coupled the system in a full 6-DOF dynamical state. In this way, it is not necessary to assume any peculiar pointing profile for the spacecraft and a detailed model for all the reflective surfaces of the platform is not needed. Given the prototyping and investigative analyses presented in this thesis, the loss of accuracy brought by this model is not relevant since catching the correct order of magnitude for this perturbation is the main goal.

2.1.3 Absolute and Relative cislunar dynamics

Specialising the above presented formulations in the environment under study, we can define the following absolute and relative dynamics, to be exploited in the upcoming analyses.

An object in the cislunar space domain is influenced by the gravitational potential of both Moon and Earth and by the perturbing effects of the Sun's gravitational force and the Solar Radiation Pressure (SRP). Considering an

inertial formulation, the absolute dynamics of the cislunar domain can be approximated in the inertial frame as:

$$\mathbf{f}(\mathbf{x}) = \begin{cases} \ddot{x} = -\dfrac{(1-\mu)(x+\mu)}{r_1^3} - \dfrac{\mu(x-1+\mu)}{r_2^3} + a_{4th_x} + a_{SRP_x} \\ \ddot{y} = -\dfrac{(1-\mu)y}{r_1^3} - \dfrac{\mu y}{r_2^3} + a_{4th_y} + a_{SRP_y} \\ \ddot{z} = -\dfrac{(1-\mu)z}{r_1^3} - \dfrac{\mu z}{r_2^3} + a_{4th_z} + a_{SRP_z} \end{cases} \tag{2.7}$$

The equations have been expressed in non-dimensional form through the mass parameter of the Earth-Moon system. The terms r_1 and r_2 are the spacecraft distances from Earth and Moon, respectively.

To obtain the relative translational dynamics, we can simply use the dynamics of differentiation of the target to chaser relative state $\delta\mathbf{r}$ and using Eq. 2.7:

$$\ddot{\delta\mathbf{r}} = \ddot{\mathbf{r}}_c - \ddot{\mathbf{r}}_t \tag{2.8}$$

where $\ddot{\mathbf{r}}_c$ and $\ddot{\mathbf{r}}_t$ represent absolute accelerations of chaser and target. To allow the exploitation of traditional linear control theory techniques for the design of the trajectory profile, the relative dynamics in Eq. (2.8) can be linearised with a first-order Taylor expansion, assuming that the target-chaser relative distance is negligible compared to the target-primaries distances, as shown in [30]:

$$\begin{bmatrix} \dot{\delta\mathbf{r}} \\ \ddot{\delta\mathbf{r}} \end{bmatrix} \approx \begin{bmatrix} \mathbf{0} & \mathbf{I}_3 \\ \boldsymbol{\Xi}(t) & \mathbf{0} \end{bmatrix} \begin{bmatrix} \delta\mathbf{r} \\ \dot{\delta\mathbf{r}} \end{bmatrix} + \begin{bmatrix} \mathbf{0} \\ \mathbf{I}_3 \end{bmatrix} (\mathbf{u} + \delta\mathbf{a}) = \mathbf{A}(t) \begin{bmatrix} \delta\mathbf{r} \\ \dot{\delta\mathbf{r}} \end{bmatrix} + \mathbf{B}(\mathbf{u} + \delta\mathbf{a}) \tag{2.9}$$

where $\mathbf{I}_3$ a 3×3 identity matrix, $\mathbf{u}$ and $\delta\mathbf{a}$ the acceleration of the control and perturbations respectively. The matrix $\boldsymbol{\Xi}(t)$ is function of time through its dependence on the target absolute position. It is defined as:

$$\boldsymbol{\Xi}(t) = -\left(\frac{1-\mu}{r_{t_1}^3} + \frac{\mu}{r_{t_2}^3}\right)\mathbf{I}_3 + 3\frac{1-\mu}{r_{t_1}^3}\left[\hat{\mathbf{r}}_{t_1}\hat{\mathbf{r}}_{t_1}^\top\right] + 3\frac{\mu}{r_{t_2}^3}\left[\hat{\mathbf{r}}_{t_2}\hat{\mathbf{r}}_{t_2}^\top\right] \tag{2.10}$$

where $\hat{\mathbf{r}}_{t_1}$ and $\hat{\mathbf{r}}_{t_2}$ are the unit position vectors of the target with respect to the primaries in the inertial frame. Such propagation requires the knowledge of the position vectors in absolute frame and relative to the primaries of either target or chaser. This implies a major difference with respect to the single-attractor relative dynamics such as the Clohessy-Wiltshire Model (CW) equations. Moreover, Eq. (2.10) does not assume any formulation for the motion of the primaries and can thus be applied to either the CR3BP or the ephemeris model just by considering a different model for the primaries positions.

2.2 GNC techniques for the lunar environment

The goal of designing a GNC system is to define a set of routines and tasks able to estimate the spacecraft current state, compute an evolution of the state to follow and the associated control actions in order to reach a certain dynamical condition. Figure 2.3 depicts a generic GNC schematics with the different bricks providing the logical block diagram of its interaction with the external environment. This scheme represents also the logical breakdown of a possible implementation of the overall system in a simulation environment.

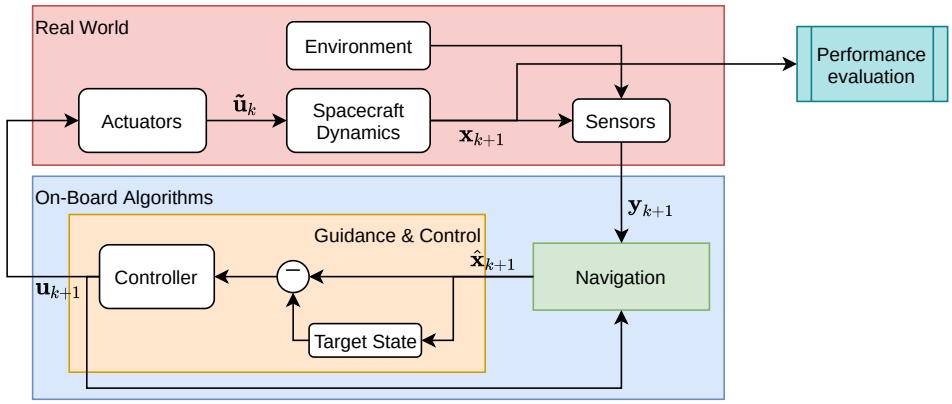

Figure 2.3: General scheme of an autonomous GNC architecture and its connections with the external environment.

The scheme is divided into two regions: one simulating the *real world* state evolution and the other consisting of the algorithms to be implemented on the spacecraft avionics. Starting from the former, the logical scheme follows the lifecycle of the execution of a simple time-step from t_k to t_{k+1}. The spacecraft dynamics is propagated for a single time step considering the high-fidelity model, including also the control action computed by the controller at the previous step and executed by the on-board actuators, providing the new state of the spacecraft. On-board sensors acquire measurements which depends on the surrounding environment and on the actual state. Sensor readings are ingested by the OBC and used in the *Navigation* step to perform the state estimation, employing also the previous control action. The state estimate is passed to the *Guidance* which defines (or retrieves) the target state evolution, i. e. the trajectory to follow. The difference among such trajectory and the estimated state is used as error to feed a *Control* block, which is in charge of defining the next control actions provided to the actuators.

To retrieve a deep understanding and explanation of the three different tasks of a GNC system can be found in [31]. In the following subsections a background

of some relevant methods used for the different tasks are proposed, with more advanced analyses for the techniques applied in this thesis.

2.2.1 Navigation

The most basic and exploited absolute Orbit Determination is based on using radiometric tracking data from Earth-based antennae. With this approach, range and Doppler measurement are acquired over scheduled communication windows above the ground station. The observations are used, usually in a single batch, to fit the evolution of the orbital state and possibly additional nuisance parameters, such as SRP modelling coefficients, on-board clock biases, but even orbital manoeuvres in case they are performed during the observation. The radiometric data can in some cases be exploited together with angular measurements as well. This approach is the standard for non-autonomous OD used, independently on the platform size-class, in a very wide variety of scenarios and, such as Earth, lunar and cislunar environment [32], deep space[33, 34] and outer planets [35]. The navigation accuracies obtainable with such technique vary widely, in the range from few metres up tens of kilometres, depending strongly on the length of the tracking windows and the trajectory geometry.

Regarding autonomous techniques, in the past years many different approaches to achieve this result have been proposed, exploiting measurements coming from sensors already exploited to perform attitude determination, such as Sun, Earth horizon sensors or magnetometers (see [36, 37, 38]). Other studies focussed on employing LoS measurements from different celestial or planetary objects, such as detecting X-ray radiations from pulsars [39] or optical measurement from either a single or multiple visible planets [40], reaching possibly accuracy orders of magnitude in the range between $10^2 \div 10^4$ km, which can be considered acceptable for certain interplanetary phases.

Another interesting proposed technique to perform autonomous absolute navigation is to exploit relative radiometric data of range and range-rate between two cooperating satellites. This technique, named *LiAISON*, works in presence of gravitational field asymmetry, such as that experienced in multi-body gravitational regimes, since the symmetry of simpler 2-body environments presents infinite possible OD solutions given a certain observables history. The first applications [41] showed promising performance in the Earth-Moon system, with values below 1 km. Other studies applied this approach also in the Martian environment [42, 43] and for lunar surface assets [44].

Looking instead at the problem of relative navigation, there are many different approaches exploiting optical sensors and extracting relevant observables, by means of Image Processing (IP) techniques, through feature detection and relative LoS exploitation [11]. Such techniques are able to provide metres-level

relative navigation errors, but need to keep a resolved target in the camera, in order to have a resolution good enough to distinguish the different features. Similar approaches can be exploited also for lunar landers, performing crater detection on surface images and extracting thus the LoS observables to feed a navigation filter [45, 46].

The three scenarios of these thesis investigates the problem of both relative and absolute navigation, considering a wide range of relative distances, from the close proximity (in the final steps of the rendezvous case) slightly above the kilometre, to the larger distances of the initial conditions in the orders of hundreds of kilometres for the formation flying scenario to the even larger ones of the LLO scenario. The relative BO navigation is considered as a suitable condition for far range approach in the rendezvous and formation flying scenarios, while the GNSS approach for the LLO user could be an extremely simple and effective approach to support that specific class of spacecraft users.

Excluding indeed all the interplanetary autonomous technique (for the different environment and distances involved), and the vision-based relative navigation relying on IP for feature detection (for the smaller ranges required), the possible remaining technique among the former presented is the LiAISON one, but also that showed not so promising results for spacecraft on the same orbit, such as the first two scenario. For the third one instead it may represent a possible alternative to evaluate, even though it collides partially due to the high ranges involved if an LLO to halo orbit link is considered, given a possible goal of keeping the user receiver terminal simple and without very high sensitivity.

The two navigation techniques chosen for the scenarios of this thesis are thus presented in the next subsections.

2.2.1.1 Bearing-Only Navigation

The concept of BO navigation has been proved by recent studies on relative motion in the simple 2-Body gravitational regime. In particular Woffinden [47] and Grzymisch [48] defined a necessary and sufficient condition for the observability the alteration of the measurement history with respect to the natural trajectory, which can be achieved by performing orbital manoeuvres. If such perturbation of the motion provides a different evolution of LoS angles, the trajectory becomes unique, and its observability, mathematically speaking, is obtained.

Practically speaking, however, due to the uncertainty of the measurements and of the dynamics the navigation filter may not be completely able to converge to a solution simply. This fact requires the definition of an observability metric which can be used to design proper trajectories that enhance the estimation performance. In this direction in [20] a metric based on relative range and

observability angle was investigated, but provided analytical solution of very simple scenarios only. In [49] instead the observability was found to be well defined by the positive linear independence between the relative position vector with and without the propulsive action. Then this observability metric was combined by the same author to a fuel minimisation objective within an optimal control problem [21] in a weighted sum approach. Further studies [50] tried instead to exploit the Fisher Information Matrix to evaluate the observability metric and use it in a closed-loop guidance scheme.

Figure 2.4 presents easily the geometry behind the BO strategy, focusing on the range uncertainty $\delta\rho$. The fixed target (grey dot) and the chaser (red dot) are depicted, with the latter in its unperturbed $\hat{\mathbf{r}}$ and perturbed $\mathbf{r}$ relative state. The observability angle θ is defined as the angular distance among the two LoS vectors, while the perturbation angle γ is the one between the natural LoS and the position perturbation provided by the manoeuvre. On the left an ideal scenario is plotted, where no measurements error are considered. In this case it is possible to directly obtain the relative distance r as in Eq. 2.11.

$$r = \delta r \frac{\sin(\theta + \gamma)}{\sin\theta} \tag{2.11}$$

In real scenarios however, the bearing measurement is affected by a noise term ε (due to sensors misreading or errors in the image processing), which provide a certain uncertainty $\delta\rho$ also in the relative distance estimate.

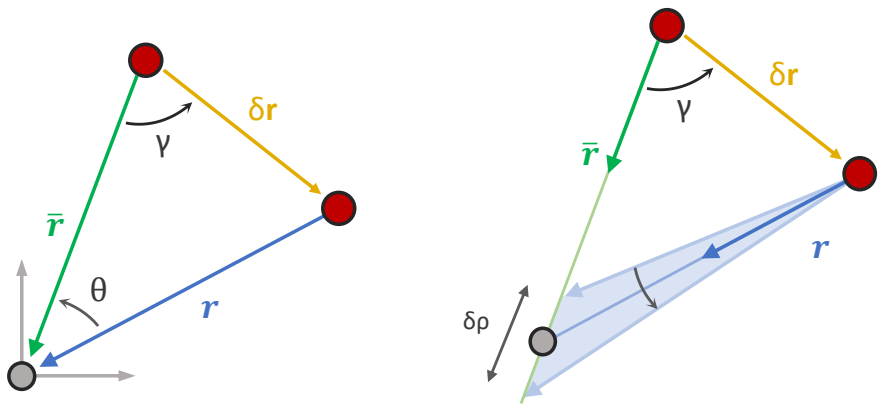

Figure 2.4: Range detectability geometry in the ideal (*left*) and real (*right*) scenario. $\mathbf{r}$ is the position vector of the real trajectory whereas $\bar{\mathbf{r}}$ represents the natural dynamics. Image readapted from [20].

Woffinden in [20] showed that under small measurement error assumptions, as typically sensible, the relative range uncertainty $\delta\rho$ can be approximated as in Eq. 2.12.

$$\frac{\delta\rho}{r} = \frac{\varepsilon}{\sin\theta} \tag{2.12}$$

By looking at this expression we see that to improve the relative uncertainty we can act only on the sensor accuracy ε or on the observability angle θ. Since the former solution is not always applicable and has some technology limitations, the only viable option is to design trajectories that maximise the observability angle.

It is important also to highlight that if multiple manoeuvres are performed, the observability angle is in any case defined with respect to the natural motion when no manoeuvre at all is executed. Consequently we can employ this concept to design rendezvous trajectories starting from initial conditions whose unperturbed trajectory ends almost perpendicularly to the desired final state. In such a way, the natural evolution maximises the angle θ if the rendezvous is correctly executed and driven to the desired end condition.

The concept of BO guidance has however been used only in the Keplerian 2-Body gravitational regime. The goal of chapter 4 is to exploit these ideas into two different proximity dynamics scenarios posed in the more complex multi-body dynamical regime.

2.2.1.2 GNSS navigation

The concept of a GNSS constellations is based on the goal to provide navigation accurate and continuous positioning and timing estimation to a set of users equipped with receiving terminals. The Position Velocity Timing (PVT) determination of the user is performed exploiting range and range-rate observables obtained from the satellites of the constellation (servicers) that are currently in its visibility. Given the necessity of servicing an extremely wide number of users, the latter shall be completely passive in the RF link, reason for which they need only a receiver. The ranging strategy thus adopted is called *One-Way* since it is based on the estimation of the range measuring the signal Time of Arrival (ToA) from the servicer to the user. The signal sent by the servicer entails both the time of transmission as measured from a precise atomic clock, and the servicer ephemerides as reconstructed by its own navigation system.

The most relevant GNSS constellations currently present around the Earth are four: the GPS (USA), GLONASS (Russia), GALILEO (Europe) and BeiDou (China). The resulting navigation errors for Earth surface users can reach accuracy from tens of metres to centimetres levels, when a number of around 10 servicers are visible. The exploitation of the GNSS navigation for LEO users provide in general lower performance, but in any case in the order of metres to tens of metres.

To provide navigation to the Moon users, different analyses are being carried out in the recent years, considering the exploitation of Earth-based GNSS constellations and also to study the design of a Moon-orbiting constellation of

satellites. Regarding the former concept, different studies are being conducted, with also planned missions to test this technology [16], showing navigation errors generally below 10 km and reaching values even lower than 1 km. The study of providing a lunar constellation on its own has started from both NASA, ESA and JAXA projects, with the aim of providing an increasing performance in the years, starting from a South Pole targetting and upscaling that also to orbital users. The preliminary performance assessments started just recently with works trying to assess the performance of lander and orbital missions with simple kinematic estimation algorithms [51, 52].

In order to formalise the GNSS navigation simulation framework, the orbit-to-orbit visibility needs to be presented, together also with the concept of DOP, which will become useful for the optimisation problem setup.

Visibility Consider the relative geometry of a satellite constellation element S_i and a user U_j on a different orbit. For simplicity, let's consider the planar case to illustrate the concepts associated to the reciprocal visibility between the satellites, whose geometry is illustrated in Fig. 2.5. First the point to point

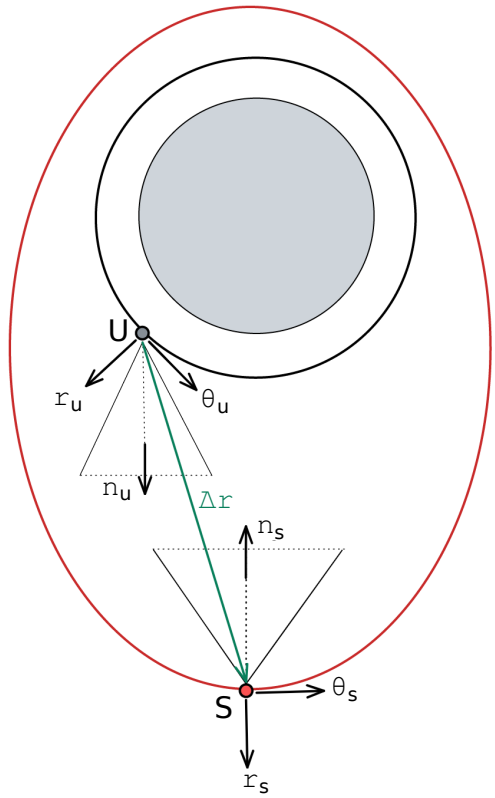

Figure 2.5: User-servicer relative geometry.

visibility between the two elements can be computed considering that, given the Moon-centric position of S_i and U_j as $\mathbf{r}_S$, $\mathbf{r}_U$ respectively, the relative position vector may be computed as:

$$\Delta\mathbf{r} = \mathbf{r}_S - \mathbf{r}_U \tag{2.13}$$

Therefore, the point-to-point visibility is achieved if $\Delta\mathbf{r}$ does not intersect the Moon, i.e., based on the approach proposed in [53], analysing the values of the following angles, where the the radius $R_{\text{☽}}$ of the occulting spherical body is used.

$$\theta_{ij}(t) = \arccos \frac{\mathbf{r}_U \cdot \mathbf{r}_S}{\|\mathbf{r}_U\| \, \|\mathbf{r}_S\|} \tag{2.14}$$

$$\theta_i(t) = \arccos R_{\text{☽}} / \|\mathbf{r}_S\| \tag{2.15}$$

$$\theta_j(t) = \arccos R_{\text{☽}} / \|\mathbf{r}_U\| \tag{2.16}$$

Thus $\mathcal{V}_{ij}^p(t)$, the point-to-point (hence the superscript p) visibility function from the i-th satellite to the j-th user, can be defined by:

$$\mathcal{V}_{ij}^p(t) = \begin{cases} 0 & \text{if} \quad \theta_i(t) + \theta_i(t) \leq \theta_{ij}(t) \\ 1 & \text{elsewhere} \end{cases} \tag{2.17}$$

Then a FoV (FoV) is associated to both the user and the servicers. In general, these could be oriented in any direction in the Local Vertical Local Horizon frame. Then, it is assumed that the pointing direction is represented by means of a direction vector $\mathbf{n}_U$ and $\mathbf{n}_S$ for the user and the servicer respectively, as well as each spacecraft has a circular FoV with half-cone angle α_U and α_S. Therefore the visibility between the servicer i and the user j could be computed exploiting the condition:

$$\begin{aligned} f_{ij}(t) = \mathcal{V}_{ij}^p(t) \cdot \left(\arccos \frac{\mathbf{n}_U(t) \cdot \Delta\mathbf{r}(t)}{\|\Delta\mathbf{r}(t)\|} < \alpha_U \right) \cdot \\ \cdot \left(\arccos \frac{-\,\mathbf{n}_S(t) \cdot \Delta\mathbf{r}(t)}{\|\Delta\mathbf{r}(t)\|} < \alpha_S \right) \end{aligned} \tag{2.18}$$

so that the visibility function can be computed as:

$$\mathcal{V}_{ij}(t) = \begin{cases} 1 & f_{ij}(t) = 1 \\ 0 & f_{ij}(t) = 0 \end{cases} \tag{2.19}$$

In case the coverage function of a j-th point is computed with respect to the whole satellite constellation, the satellite visibility functions $\mathcal{V}_{ij}(t)$ of the constellation must be combined [54]. In particular, having defined the multi-sat coverage function, $\mathcal{N}_j(t)$:

$$\mathcal{N}_j(t) = \sum_{i}^{N} \mathcal{V}_{ij}(t) \quad \text{s.t.} \quad \mathcal{N}_j : \mathbb{R} \to \mathbb{N} \tag{2.20}$$

the *n-fold continuous coverage index* can be defined as:

$$\mathcal{F}_j(t, n) = \begin{cases} 1 & \mathcal{N}_j(t) \geq n \\ 0 & \mathcal{N}_j(t) < n \end{cases} \tag{2.21}$$

Dilution of Precision The concept of DOP is the idea that the position error that results from measurement errors depends on the user relative geometry. The DOP figures therefore represents a key parameter for the evaluation of satellite constellation's navigation performance. The formal derivation of the DOP relations begins with the linearisation of the pseudorange equation [55]. This linearisation provides the Jacobian $\mathbf{\Pi}$, which relates changes in the user position and time bias to changes in the pseudorange values. If this relationship is inverted, it can be used to relate the covariance of the user position and time bias to the covariance of the pseudorange errors.

$$\mathbf{\Delta x} = \mathbf{\Gamma}\, \Delta\boldsymbol{\rho} \quad \text{with} \begin{cases} \mathbf{\Gamma} = \mathbf{\Pi}^{-1} \text{ if } n = 4 \\ \mathbf{\Gamma} = \left(\mathbf{\Pi}^{\top}\mathbf{\Pi}\right)^{-1}\mathbf{\Pi}^{\top} \text{ elsewhere} \end{cases} \tag{2.22}$$

The DOP parameters are then defined as geometry factors that relate parameters of the user position and time bias errors to those of the pseudorange errors. The components of the matrix $\mathbf{\Theta} = \left(\mathbf{\Pi}^{\top}\mathbf{\Pi}\right)^{-1}$ quantify how pseudorange errors translate into components of the covariance of $\mathbf{\Delta x}$. The different DOP measures can be defined exploiting the different components of $\mathbf{\Theta}$, as per Eq.s 2.23, 2.24, 2.25, 2.26 and 2.27 indicating *geometric*, *position*, *horizontal*, *vertical* and *time* DOP respectively.

$$\texttt{GDOP} = \sqrt{\mathbf{\Theta}_{11} + \mathbf{\Theta}_{22} + \mathbf{\Theta}_{33} + \mathbf{\Theta}_{44}} \tag{2.23}$$

$$\texttt{PDOP} = \sqrt{\mathbf{\Theta}_{11} + \mathbf{\Theta}_{22} + \mathbf{\Theta}_{33}} \tag{2.24}$$

$$\texttt{HDOP} = \sqrt{\mathbf{\Theta}_{11} + \mathbf{\Theta}_{22}} \tag{2.25}$$

$$\texttt{VDOP} = \sqrt{\mathbf{\Theta}_{33}} \tag{2.26}$$

$$\texttt{TDOP} = \sqrt{\mathbf{\Theta}_{44}} \tag{2.27}$$

If only 3 satellites are in view, it is possible to assume that the vertical component is known a-priori (e.g. for a surface user this is given by the local topography) and compute the horizontal component of the DOP only, namely the `2DHDOP`. This is done by removing the third column (associated to the z-direction) from the $\mathbf{\Pi}$ matrix.

Moreover, in this study are considered of interest also the following quantities:

- $\texttt{DOPAV}_j = \mathcal{F}_j(t, 4)$ is used to identify the regions where the `GDOP` exists, and then its value is computed with Eq. 2.23.
- $\texttt{2DHDOPAV}_j = \mathcal{F}_j(t, 3)$ is used to identify the regions where the `2DHDOP` exists, and then its value is computed with Eq. 2.25 on the $\mathbf{\Pi}$ matrix eroded by the third column.

2.2.2 Guidance and Control

The guidance law main objective is to determine the necessary trajectory and its potential correction to successfully arrive at the target position or orbit. The control is instead in charge of computing the correct actions that drive the error with respect to the targetted trajectory to zero. In some specific cases, when the orbital transfer relies on ground optimization of impulsive manoeuvres, a simple guidance algorithm with strong flight heritage is represented by the *bi-impulse guidance* or *Fixed Time of Arrival* (FTOA), where the control action is determined to target and reach a specific point in a given Time of Flight (ToF). This approach has the advantage of being computationally light, as it does not require any closed loop logic, and has also a high flight heritage; however, it relies on linearised models and assumes impulsive manoeuvres, thus limiting the range of possible applications. Since the resulting control action is trivial, it does not necessitate any feedback control algorithm, other than the actual execution of the thrusting action for the small time window envisioned by the guidance.

In case of continuous or quasi-continuous control across the transfer arcs, a different approach must be adopted. The typical approach is the on ground computation of a reference trajectory, which is then targeted by the on-board controller. A very common type of on-board scheme is represented by the PID. This kind of strategy relies as well on linearised models, but possesses also good reliability and versatility, additionally improved by the very high understanding and legacy obtained in a wide range of industrial applications. In turn, the scheme does not rely on an optimality-driven approach, hence the overall cost tends to be higher than other more recent techniques.

Indeed, control techniques can embed the mathematical description of the dynamical model, or parameters related to it, to approach a more optimal solution. Among them, well known controllers are the *Linear Quadratic Regu-*

lators (LQR) [56] and the *Floquet-Based Controllers* [57]. The aforementioned controllers, although computationally light, rely on linear expression of the dynamics, preventing their usage in cases where dynamics nonlinearities can be relevant. A well-known scheme to deal with nonlinear dynamics is represented by *Sliding Mode Control*, which demonstrated to be also a robust approach if properly designed [58]. Nevertheless, it typically provides non-optimal solutions, leading to overall higher costs. Recent studies explored the concept of *zero-effort-miss/zero-effort-velocity* (ZEM/ZEV) controller which has been successfully employed for optimal spacecraft formation control. The main drawbacks are the loss of optimality in non uniform gravitational fields [59], and the lack of parameters to tune (reducing the adaptation margins to different scenarios). A good compromise is represented by the *State Dependent Riccati Equation* (SDRE) controller [60], where a linearisation at each time step allows to leverage the LQR formulation and approach its optimality, while limiting the increase of computational cost. As a drawback, the scheme itself does not allow a direct implementation of state nor control constraints.

2.2.2.1 Model Predictive Control

The MPC can, in general, entail both the guidance and control task of the autonomous system, providing a model-informed adaptive strategy to reach specific goals in terms of objectives and constraints.

A control action is computed, in such scheme, through the minimisation of a specific cost function that is discretised within a time window and whose solution is obtained via numerical optimisers. A detailed reference for the model predictive schemes can be found in [61].

At each discrete time step, the time window is defined and the evolution of the controlled state is predicted, searching for the optimal control sequence. The basic idea of the scheme is to execute only part of the predicted control actions (generally only the first term), and then in order to repeat the cycle a new finite-horizon window is defined. In such a way the MPC is capable of adapting its response to the possible deviations of the real world dynamics from that used onboard in the prediction. Moreover, dealing with a numerical optimisation, it is generally possible to include constraints on the state or on the control, providing a much higher versatility with respect to other simpler guidance and control scheme, such as an LQR. The MPC was demonstrated to be effective in different applications within the autonomous GNC branch, both for Unmanned Aerial Vehicles and spacecraft [62, 63, 64].

In order to design an MPC scheme it is necessary to deal with three aspects

1. Formulation of the *time horizon* window at each step
2. Definition of *objective and constraint*

3. Calibration and tuning of the *weights* present in the optimisation problem

On the time horizon, there are mainly two alternatives to manage the prediction window, i. e. the *Receding Horizon* and the *Shrinking Horizon*.

Employing the *Receding Horizon* scheme, the window is fixed in size and at each step it shifts both the start and the end point by a number of samples equal to the number of control actions that are executed [64], as represented in Figure 2.6. Looking at the k^{th} time step, the algorithm works in the following

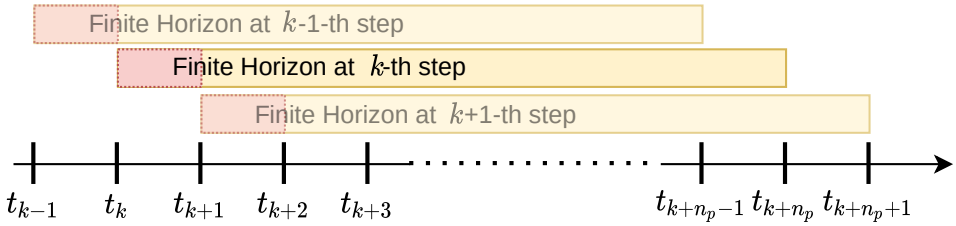

Figure 2.6: Receding horizon MPC guidance scheme.

way.

1. Consider the finite-horizon window with the prediction of n_p discrete time-steps. The time step boundaries are thus $[t_k,\ t_{k+n_p}]$.
2. Predict the dynamics using the on-board model and the best estimate available of the initial state $\hat{\mathbf{x}}_k$. Using an estimate obtained after the latest control action executed, instead of the prediction of $\hat{\mathbf{x}}_k$ obtained in the previous step, ensures the feedback and adaptive behaviour of the MPC, for which the new control actions are evaluated after having observed the results of the actions in the real dynamics.
3. Define and solve the optimal control problem which minimises a cost function J, exploiting the evolution predicted in the finite horizon. The new control actions are obtained, which are $\mathbf{u}_k,\ \mathbf{u}_{k+1},\ \ldots,\ \mathbf{u}_{k+n_p-1}$.
4. Command the execution of the first control (or controls) only, discarding the other computed terms.
5. Update the finite horizon, by *receding* the window by the one (or more) time-step and restart the cycle from point 1, where the new time extrema will be $[t_{k+1},\ t_{k+n_p+1}]$.

This loop is repeated for the required application time, which vary mission by mission. A possibility is also to define some stopping criteria whose occurrence cause the loop to be concluded, such as when reaching a specific state. With the receding horizon approach we do not have a direct control on the ToF, but there is a control on the accuracy and speed of the process, which can be

achieved bt tuning the duration of the receding horizon and the number of discretisation points in it.

Figure 2.7 presents instead the *Shrinking–Horizon* model, where the time window has a variable dimension since the only time boundary that moves at each step is the initial time (moving together with the on-board time), while the final time of the window is kept fixed to a desired end epoch.

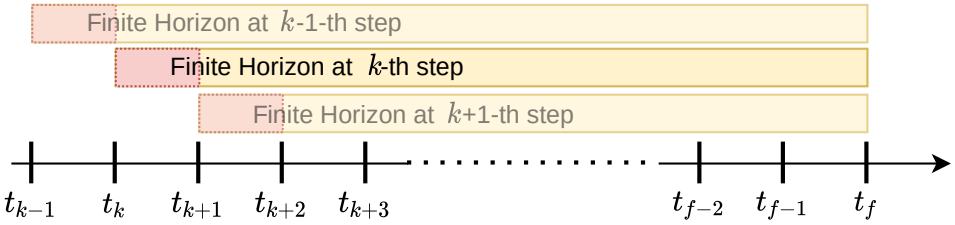

Figure 2.7: Shrinking horizon MPC guidance scheme.

The ToF is thus imposed by design and the time window at each iteration contains each time step from t_k to the final time t_f. The same steps followed by the receding horizon are executed also in this case, with the only difference that the time window's final step is not shifting with the initial one and as a consequence the horizon keeps *shrinking* at each iteration. This second alternative has the advantage of dealing with much larger windows that cover all the transfer. In such a way, generally, the resulting control actions are more optimal with respect to a shorter and less foreseeing window (as for the receding horizon). The drawback of this approach is clearly that the resulting optimisation problems are large and heavier computationally speaking. In addition to that, longer prediction times for a highly nonlinear system may results in higher propagation errors, thus providing control sequences which are less reliable.

The choice among the two schemes has to be done case by case, since any scenario may have completely different requirements. In this thesis work both approaches are used, one for the rendezvous scenario and the other for the formation flying one.

CHAPTER 3

State Estimation Filtering

PROVIDING navigation functionalities to a robotic system such as a spacecraft means dealing with estimation techniques able reconstruct the dynamical state of the system. Such problem has been treated deeply in the aerospace field literature and requires both deep statistical understandings and algorithmic implementation considerations. This chapter wants to provide hints on both aspects, defining first a set of possible alternatives in the selection of the architecture, as in Section 3.1, and then providing the mathematical formulations of the most common filters belonging to the Kalman family, in Section 3.2. Finally, Section 3.3 provides an overview of the different measurement models needed for the systems under study, regarding optical and radiometric observables but also altimeters and accelerometers. The last Subsection 3.3.4 recalls also the methodology used to propagate measurements uncertainty in nonlinear formulations, a required feature for the applications under study, where different stochastic variables contribute to the definition of the measurement.

3.1 Estimator architecture alternatives

Before jumping into the mathematical definition of the different filters considered in this thesis, this section presents two specific trade-offs that need to be sorted out when the design process of a spacecraft navigation algorithm is started. The first one deals with the strategy to treat the measurements, the second with the coupling of translational and rotational dynamics in the state to be reconstructed. The algorithms implemented in this research consider both trade-offs solved towards a specific alternative in both cases, as pointed out during the treatment.

3.1.1 Batch vs Sequential Filters

The primary differentiation put in place in designing a navigation filter is provided be the way the measurements are handled. It is possible indeed to process each measure as soon as it is available or wait for a set of different ones to be collected before executing the filtering algorithm. The algorithms acting as in the former case are called *Sequential Filters*, while those in the latter case are defined *Batch Filters*.

There are both intrinsic and indirect differences in the two formulations. First, given that sequential filters process instantaneous measurements, they require their execution at each time step but due to the processing of a single sensors reading, the computational demand is lower. On the other side batch filter have the advantage of being executed just once, or in any case with a much lower frequency, and exploiting a much higher number of measurements they are able to provide higher overall accuracies and generally less affected by the *a-priori* state guess. Their downside, directly related to the higher number of measurements, is the computational heaviness, which rises with the square of the number of measurements.

Batch filters are generally used for applications where the state update frequency is low, such as for OD performed on-ground, where the computational resources are not constrained and the results are used for schedule prediction and manoeuvres prediction. The sequential formulations are instead more suited for autonomous operational scenarios, where an instantaneous and frequent estimate of the state is needed to be included in the complete GNC loop for both the orbital and attitude dynamics. For such reasons, sequential formulations are taken into considerations in the rest of the work.

3.1.2 6-DOF coupled vs de-coupled estimation

A second choice to be performed in the definition of GNC architectures regards how to deal with both attitude and orbital state estimation. If the complete 6-Degrees of Freedom (DOF) dynamics of the spacecraft needs to be retrieved,

it is possible either to rely on the same estimator for both translational and rotational motion or to separate the two dynamics.

It is relevant to consider that there are certain effects to be considered in the orbital navigation that actually depends on the current attitude. Such connection between the two domains is achieved e. g. when the complete attitude-dependent SRP model is used within the orbital dynamics, or when the information on an accelerometer are included.

Consequently the estimation of the attitude shall be generated either contemporaneously (through a 6-DOF coupled filter) or beforehand (through a separated estimator). Choosing a fully coupled formulation, the statistical correlation among the two dynamics is explicitly active in the state and covariance estimation, providing generally a higher accuracy and robustness of the results. However, considering Kalman-like filters, the computational cost in the order of $\mathcal{O}(n^3)$, with n is the dimension of the state vector. Thus, assuming the same number of states for the two domains, a 6-DOF coupled filter requires four times the computational burden of a decoupled solution.

This requires trading-off, as usual, computational costs with accuracy and robustness of the solutions. In the rest of the present work however, the attitude estimation problem is never tackled, since the research objectives are heavily associated to the orbital state estimation only.

For the scope of the current thesis, the rotational dynamics is not objective of the study, as such, the filters investigated consider only the translational DOFs.

3.2 Kalman-based Filters

The most common class of navigation filters employed in the space domain is represented by the family of Kalman Filters (KFs). The basic formulation of the KF was presented in 1960 by the Hungarian mathematician Rudolf Kalman [65], whence the name of the algorithm, which provided an estimator, optimal in minimising the *mean squared error* (MMSE) and maximising the *a-posteriori* probability (MAP). In the following a summary of the derivation of a Bayesian tracking estimator are presented, reporting the steps presented in [66, 67, 68], considering the problem of providing an estimate of the state vector $\mathbf{x}$ based on a certain observations vector $\mathbf{y}$ and the knowledge of the input action vector $\mathbf{u}$. In the following the estimated quantities will be identified by a hat symbol ($\hat{}$), while apexes symbols are used to indicate a-priori ($-$ sign) and a-posteriori ($+$ sign) estimates. Any normally distributed probability density function (pdf) characterised by a mean μ and a covariance $\mathbf{\Sigma}$ is indicated as $\mathcal{N}(\mu, \mathbf{\Sigma})$.

The basic approach of a recursive optimal estimator consists in defining the estimation of the state as the conditional mean, considering all the measurements gathered from the initial step 0 up to the current step $k+1$, i. e. $\mathbf{Y}_0^{k+1}$, as in Eq. 3.1.

$$\hat{\mathbf{x}}_{k+1} = \mathbb{E}[\mathbf{x}_{k+1}|\mathbf{Y}_0^{k+1}] \tag{3.1}$$

In order to compute this mean, following a Bayesian approach, the goal is to get $p(\mathbf{x}_{k+1}|\mathbf{Y}_0^{k+1})$, i. e. the a-posteriori pdf, which can be expressed at each step $k+1$ with Bayes' formula of Eq. 3.2.

$$p(\mathbf{x}_{k+1}|\mathbf{Y}_0^{k+1}) = \frac{p(\mathbf{x}_{k+1}|\mathbf{Y}_0^{k})p(\mathbf{y}_{k+1}|\mathbf{x}_{k+1})}{p(\mathbf{y}_{k+1}|\mathbf{Y}_0^{k})} \tag{3.2}$$

The dynamics of the evolving process under study and the measurement function ($\mathbf{x}_{k+1} = \mathbf{F}_k^{k+1}(\mathbf{x}_k, \mathbf{u}_k, \mathbf{w}_k)$ and $\mathbf{y}_{k+1} = \mathbf{H}_{k+1}(\mathbf{x}_{k+1}, \mathbf{v}_{k+1})$, with process and measurement noise vectors $\mathbf{w} \sim \mathcal{N}(\mathbf{0}, \mathbf{Q})$ and $\mathbf{v} \sim \mathcal{N}(\mathbf{0}, \mathbf{R})$) provide additional blocks needed to determine the pdfs of $p(\mathbf{x}_{k+1}|\mathbf{x}_k)$ and $p(\mathbf{y}_{k+1}|\mathbf{x}_{k+1})$, from which, given the initial conditions $p(\mathbf{x}_0|\mathbf{y}_0)$, it is possible to initialise the procedure.

The overall logic is thus based on recursively alternating the two stages of *prediction* and *update* at each step $k+1$. In the prediction stage, the a-posteriori pdf at step k is used, coupled with the state evolution process, to provide the a-priori pdf at step $k+1$, i. e. $p(\mathbf{x}_{k+1}|\mathbf{Y}_0^{k})$. The update is instead used to include the the information on the new observation, by exploiting Eq. 3.2. In general, the pdfs present in this equation do not have closed form solutions, but under the assumptions of Gaussian pdfs only, it is possible to deal simply with the estimate of the mean and covariance matrix of the state, i. e. $\hat{\mathbf{x}}_{k+1}$ and $\hat{\mathbf{P}}_{\mathbf{x}_{k+1}}$. The prediction step thus proceeds by exploiting the dynamical and measurements models and defines the a-priori state $\hat{\mathbf{x}}_{k+1}^-$ and observation $\hat{\mathbf{y}}_{k+1}^-$ as in the following Eq.s 3.3 and 3.4, obtaining similarly also the associated state covariance estimate, $\hat{\mathbf{P}}_{\mathbf{x}_{k+1}}^-$.

$$\hat{\mathbf{x}}_{k+1}^- = \mathbb{E}[\mathbf{F}_k^{k+1}(\mathbf{x}_k, \mathbf{u}_k, \mathbf{w}_k)] \tag{3.3}$$

$$\hat{\mathbf{y}}_{k+1}^- = \mathbb{E}[\mathbf{H}_k^{k+1}(\hat{\mathbf{x}}_{k+1}^-, \mathbf{v}_{k+1})] \tag{3.4}$$

With these expression for the a-priori quantities, it is possible to perform the update step defining the so-called *Kalman Gain* matrix, $\mathbf{K}_{k+1}$ as in the following,

$$\mathbf{K}_{k+1} = \mathbf{P}_{\mathbf{xy}}\mathbf{P}^{-1}_{\delta\mathbf{y}\delta\mathbf{y}} \tag{3.5}$$
$$\hat{\mathbf{x}}^{+}_{k+1} = \hat{\mathbf{x}}^{-}_{k+1} + \mathbf{K}_{k+1}(\mathbf{y}_{k+1} - \hat{\mathbf{y}}_{k+1}) \tag{3.6}$$
$$\hat{\mathbf{P}}^{+}_{\mathbf{x}_{k+1}} = \hat{\mathbf{P}}^{-}_{\mathbf{x}_{k+1}} + \mathbf{K}_{k+1}\mathbf{P}_{\delta\mathbf{y}\delta\mathbf{y}}\mathbf{K}^{\top}_{k+1} \tag{3.7}$$

where reasonable expressions to evaluate the covariance matrices $\mathbf{P}_{\mathbf{xy}}$ and $\mathbf{P}_{\delta\mathbf{y}\delta\mathbf{y}}$ are needed, with $\delta\mathbf{y}_{k+1} = \tilde{\mathbf{y}}_{k+1} - \hat{\mathbf{y}}_{k+1}$ called *innovation* vector, i. e. the difference between the sensors observation and its a-priori estimate.
The formulations of the filters in the Kalman family differ in which assumptions are made and thus how Eq.s 3.3 and 3.4 are treated and how the different a-priori covariance matrices are estimated.

3.2.1 Kalman Filter

The simplest formulation within this framework is provided by the *linear* Kalman Filter, which is used when that state space formulation can be considered as a fully linear system. The dynamics and measurement functions, in discrete-time are expressed as in Eq.s 3.8 and 3.9, as used by the prediction step to generate the a-priori mean quantities, together with the state covariance in Eq. 3.10. Note the introduction of the different matrices used to describe the linear dependence of the state evolution and the measurement from the instantaneous state ($\mathbf{F}^{k+1}_{k}$ and $\mathbf{H}_{k+1}$), the control action ($\mathbf{B}_{u,k}$), and the noise terms ($\mathbf{B}_k$ and $\mathbf{D}_{k+1}$).

$$\hat{\mathbf{x}}^{-}_{k+1} = \mathbf{F}^{k+1}_{k}\hat{\mathbf{x}}^{+}_{k} + \mathbf{B}_{u,k}\mathbf{u}_k + \mathbf{B}_k\mathbf{w}_k \tag{3.8}$$
$$\hat{\mathbf{y}}^{-}_{k+1} = \mathbf{H}_{k+1}\hat{\mathbf{x}}^{-}_{k+1} + \mathbf{D}_{k+1}\mathbf{v}_{k+1} \tag{3.9}$$
$$\mathbf{P}^{-}_{k+1} = \mathbf{F}^{k+1}_{k}\mathbf{P}^{+}_{k}(\mathbf{F}^{k+1}_{k})^{\top} + \mathbf{B}_k\mathbf{Q}\mathbf{B}^{\top}_{k} \tag{3.10}$$

The update step is then defined by the following set of equations.

$$\mathbf{K}_{k+1} = \mathbf{P}^{-}_{k+1}\mathbf{H}^{\top}_{k+1}(\mathbf{H}_{k+1}\mathbf{P}^{-}_{k+1}\mathbf{H}^{\top}_{k+1} + \mathbf{D}_{k+1}\mathbf{R}\mathbf{D}^{\top}_{k+1})^{-1} \tag{3.11}$$
$$\hat{\mathbf{x}}^{+}_{k+1} = \hat{\mathbf{x}}^{-}_{k+1} + \mathbf{K}_{k+1}(\tilde{\mathbf{y}}_{k+1} - \hat{\mathbf{y}}^{-}_{k+1}) \tag{3.12}$$
$$\mathbf{P}^{+}_{k+1} = (\mathbf{I} - \mathbf{K}_{k+1}\mathbf{H}_{k+1})\mathbf{P}^{-}_{k+1} \tag{3.13}$$

In such a way the algorithm exploits the fact that the Gaussian random variables are linearly mapped through the dynamics and measurement functions, thus preserving their statistical nature. As a consequence, the KF results as the optimal estimator for linear models and fully Gaussian processes. The KF has a numerical complexity of $\mathcal{O}(n^3)$, with n the size of the state.

3.2.2 Extended Kalman Filter

Let's consider now a nonlinear dynamical system, whose state and measurement functions can be expressed as in the following Eq.s 3.14 and 3.15

$$\dot{\mathbf{x}} = \mathbf{f}_{\text{cont}}(\mathbf{x}, \mathbf{u}, t) + \mathbf{w} \tag{3.14}$$
$$\mathbf{y} = \mathbf{h}(\mathbf{x}, t) + \mathbf{v} \tag{3.15}$$

with vectorial forms of state dynamics and measurement function, $\mathbf{f}_{\text{cont}}$ and $\mathbf{h}$. Assuming these two functions to be known and modelled up to a certain confidence degree, additional unmodelled effects of stochastic components and are here condensed into additive Gaussian random variables, namely $\mathbf{w}$ and $\mathbf{v}$. These two components follow normal distribution as $\mathbf{w} \sim \mathcal{N}(\mathbf{0}, \mathbf{Q})$ and $\mathbf{v} \sim \mathcal{N}(\mathbf{0}, \mathbf{R})$. To bring the equations into the discrete-time domain, the integration of the dynamics between the two samples k and $k+1$ can be performed either analytically or numerically, leading to Eq.s 3.16 and 3.17.

$$\mathbf{x}_{k+1} = \mathbf{f}(\mathbf{x}_k, \mathbf{u}_k, \mathbf{w}_k) \tag{3.16}$$
$$\mathbf{y}_{k+1} = \mathbf{h}(\mathbf{x}_{k+1}, \mathbf{v}_{k+1}) \tag{3.17}$$

The EKF assumes that the state is a Gaussian random variable and, in the prediction step, adopt these equations to evaluate the a-priori of the state and measurement. For all the covariances, instead the linearised version of these equations is employed, defining the following Jacobian matrices for the state dynamics, process noise, measurement and measurement noise.

$$\mathbf{F}_k^{k+1} = \left.\frac{\partial \mathbf{f}}{\partial \mathbf{x}}\right|_{\hat{\mathbf{x}}_k^+} \qquad \mathbf{B}_k = \left.\frac{\partial \mathbf{f}}{\partial \mathbf{w}}\right|_{\mathbf{w}_k} \tag{3.18}$$
$$\mathbf{H}_{k+1} = \left.\frac{\partial \mathbf{h}}{\partial \mathbf{x}}\right|_{\hat{\mathbf{x}}_{k+1}^-} \qquad \mathbf{D}_{k+1} = \left.\frac{\partial \mathbf{h}}{\partial \mathbf{v}}\right|_{\mathbf{v}_{k+1}} \tag{3.19}$$

The realisation of Eq.s 3.3 and 3.4 and the a-priori state covariance, for the EKF, are then defined as in Eq.s 3.20, 3.21 and 3.22,

$$\hat{\mathbf{x}}_{k+1}^- = \mathbf{f}(\hat{\mathbf{x}}_k^+, \mathbf{u}_k, \mathbf{0}) \tag{3.20}$$
$$\hat{\mathbf{y}}_{k+1}^- = \mathbf{h}(\hat{\mathbf{x}}_{k+1}^-, \mathbf{0}) \tag{3.21}$$
$$\mathbf{P}_{k+1}^- = \mathbf{F}_k^{k+1} \mathbf{P}_k^+ (\mathbf{F}_k^{k+1})^\top + \mathbf{B}_k \mathbf{Q} \mathbf{B}_k^\top \tag{3.22}$$

Finally the *Update Step* can be executed, providing the *a-posteriori* state and covariance matrix estimates.

$$\mathbf{K}_{k+1} = \mathbf{P}^{-}_{k+1}\mathbf{H}^{\top}_{k+1}(\mathbf{H}_{k+1}\mathbf{P}^{-}_{k+1}\mathbf{H}^{\top}_{k+1} + \mathbf{D}_{k+1}\mathbf{R}\mathbf{D}^{\top}_{k+1})^{-1} \tag{3.23}$$

$$\hat{\mathbf{x}}^{+}_{k+1} = \hat{\mathbf{x}}^{-}_{k+1} + \mathbf{K}_{k+1}(\tilde{\mathbf{y}}_{k+1} - \hat{\mathbf{y}}^{-}_{k+1}) \tag{3.24}$$

$$\mathbf{P}^{+}_{k+1} = (\mathbf{I} - \mathbf{K}_{k+1}\mathbf{H}_{k+1})\mathbf{P}^{-}_{k+1} \tag{3.25}$$

Note, that Eq.s 3.23, 3.24 and 3.25 are exactly the same as Eq.s 3.11, 3.12 and 3.13 for the linear KF case, with the matrices obtained as first-order linearisation of the nonlinear equations. In case the effects of the nonlinearities are high, these linearisation can introduce relevant errors in the estimation, leading even to divergence of the filter. Anyway, if the nonlinear dynamics is not so sensitive, the EKF is an extremely powerful tool for the navigation task.

A numerical issue that could rise in the update of the state covariance performed in Eq. 3.25 due to the approximations in the covariance expression is that $\mathbf{P}^{+}_{k+1}$ may become non-positive definite. To reduce the likelihood of this issue, the covariance update can be performed with the so-called *Joseph Formula* in Eq. 3.26.

$$\mathbf{P}^{+}_{k+1} = (\mathbf{I}-\mathbf{K}_{k+1}\mathbf{H}_{k+1})\mathbf{P}^{-}_{k+1}(\mathbf{I}-\mathbf{K}_{k+1}\mathbf{H}_{k+1})+\mathbf{K}_{k+1}\mathbf{D}_{k+1}\mathbf{R}\mathbf{D}^{\top}_{k+1}\mathbf{K}^{\top}_{k+1} \tag{3.26}$$

This expression is algebraically identical to Eq. 3.25, but with this symmetric additive form, the insurgence of this issue is less likely.

As pointed out previously, passing from Eq. 3.14 to Eq. 3.16 an integration step is performed, and dealing with nonlinear equations of motion, it is likely that a numerical solution is forsaken, particularly considering on-board embedded application. Depending on the scenario, it is possible to rely on different methods to perform this step, providing a trade-off between numerical efficiency and accuracy. The same consideration can be found also in the representation of the dynamics Jacobian matrix in Eq. 3.18. Extensive and detailed considerations on this topic are found in [69, 70].

Moreover, recall also that, once defined the dynamics and measurement models, two quantities remain to be provided, i. e. the process and measurement noise covariances, namely $\mathbf{Q}$ and $\mathbf{R}$. If the latter is practically constrained by the sensor accuracy, the former is more complex to be estimated for a given dynamical system, remaining a tunable parameter. Similarly the initial condition of the state covariance $\mathbf{P}_0$ is another parameter that can be slightly adjusted to drive the filter to the convergence.

3.2.3 Unscented Kalman Filter

To overcome the possible problems encountered by the EKF in presence of large nonlinearities, the Unscented Kalman Filter (UKF) provides a viable

alternative. Also here the state is considered with a Gaussian distribution, but instead of describing it only through the propagation of the mean and covariance, the conditional means of Eq.s 3.3 and 3.4 are obtained on a set of sampling points called *sigma points*. The propagation of the state distribution is obtained through the Unscented Transformation, which is able to approximate the a-posteriori mean and covariance up to the 3^{rd} order, also in case of large nonlinearities if the random inputs are Gaussian, up to the 2^{nd} otherwise.

The Unscented Transformation (UT) is thus used in the filter to retrieve a more accurate estimate of the a-priori state and measurement, $\hat{\mathbf{x}}_{k+1}^{-}$ and $\hat{\mathbf{y}}_{k+1}^{-}$, and all the associated covariance matrices, thus $\mathbf{P}_{k+1}^{-}$, $\mathbf{P}_{\mathbf{xy}}^{-}$ and $\mathbf{P}_{\delta\mathbf{y}\delta\mathbf{y}}^{-}$. Note that in this formulation an additive noise model is considered for the process and measurement noise terms.

A total of $2n + 1$ sigma points is defined as in Eq. 3.27, 3.28 and 3.29.

$$\mathbf{x}_0 = \hat{\mathbf{x}}_k^{+} \tag{3.27}$$

$$\mathbf{x}_i = \hat{\mathbf{x}}_k^{+} + \left(\sqrt{(n+\lambda)\mathbf{P}_k^{+}}\right)_i \qquad \text{i} = 1, \ldots, \text{n} \tag{3.28}$$

$$\mathbf{x}_i = \hat{\mathbf{x}}_k^{+} - \left(\sqrt{(n+\lambda)\mathbf{P}_k^{+}}\right)_{i-n} \qquad \text{i} = \text{n+1}, \ldots, 2\text{n} \tag{3.29}$$

The notation $(\sqrt{\mathbf{A}})_i$ denotes the *i-th* column of the squared root of matrix $\mathbf{A}$. Some constants are introduced as well: two scaling parameters are used, $\lambda = \alpha^2(n + \kappa)$ and κ set to $3 - n$ or alternatively to 0. α influences how the sigma points are spread on the state space and belongs to the $[10^{-4}, 1]$ range, β is used to include information of the initial state distribution, with the best value of $\beta = 2$ for Gaussian distribution.

To reconstruct the a-priori estimates of the quantities, a weighted sum approach is followed employing different weights for the various sigma points, defined by the following set of equations.

$$W_0^{(m)} = \lambda/(n+\lambda) \tag{3.30}$$

$$W_0^{(c)} = \lambda/(n+\lambda) + 1 - \alpha^2 + \beta \tag{3.31}$$

$$W_i^{(m)} = W_i^{(c)} = 1/(2n+2\lambda) \qquad \text{i} = 1, \ldots, 2\text{n} \tag{3.32}$$

With this in mind we can formulate the prediction step as in the following. First the sigma points are all propagated through the nonlinear processes of the dynamics and measurement functions of Eq.s 3.16 and 3.17 expressing them as per Eq.s 3.33 and 3.34.

$$\mathbf{x}^-_{i,k+1} = \mathbf{f}(\mathbf{x}_i, \mathbf{u}_k, \mathbf{0}) \tag{3.33}$$

$$\mathbf{y}^-_{i,k+1} = \mathbf{h}(\mathbf{x}^-_{i,k+1}, \mathbf{0}) \tag{3.34}$$

The new two sets of sigma points are then used for the a-priori quantities exploiting the following weighted sums.

$$\hat{\mathbf{x}}^-_{k+1} = \sum_{i=0}^{2n} W_i^{(m)} \mathbf{x}^-_{i,k+1} \tag{3.35}$$

$$\hat{\mathbf{y}}^-_{k+1} = \sum_{i=0}^{2n} W_i^{(m)} \mathbf{y}^-_{i,k+1} \tag{3.36}$$

$$\mathbf{P}^-_{k+1} = \sum_{i=0}^{2n} W_i^{(c)} (\mathbf{x}^-_{i,k+1} - \hat{\mathbf{x}}^-_{k+1})(\mathbf{x}^-_{i,k+1} - \hat{\mathbf{x}}^-_{k+1})^\top + \mathbf{BQB}^\top \tag{3.37}$$

Moreover, to compute the Kalman gain, the remaining a-priori covariance matrices are computed also with the UT.

$$\mathbf{P}^-_{\mathbf{xy}} = \sum_{i=0}^{2n} W_i^{(c)} (\mathbf{x}^-_{i,k+1} - \hat{\mathbf{x}}^-_{k+1})(\mathbf{y}^-_{i,k+1} - \hat{\mathbf{y}}^-_{k+1})^\top \tag{3.38}$$

$$\mathbf{P}^-_{\delta\mathbf{y}\delta\mathbf{y}} = \sum_{i=0}^{2n} W_i^{(c)} (\mathbf{y}^-_{i,k+1} - \hat{\mathbf{y}}^-_{k+1})(\mathbf{y}^-_{i,k+1} - \hat{\mathbf{y}}^-_{k+1})^\top + \mathbf{DRD}^\top \tag{3.39}$$

Finally the update step is completed with the very same formulations of Eq.s 3.5, 3.6 and 3.7, reported for sake of completeness also in the following.

$$\mathbf{K}_{k+1} = \mathbf{P}_{\hat{\mathbf{x}}\mathbf{y}} \mathbf{P}^{-1}_{\delta\mathbf{y}\delta\mathbf{y}} \tag{3.40}$$

$$\hat{\mathbf{x}}^+_{k+1} = \hat{\mathbf{x}}^-_{k+1} + \mathbf{K}_{k+1}(\mathbf{y}_{k+1} - \hat{\mathbf{y}}_{k+1}) \tag{3.41}$$

$$\mathbf{P}^+_{k+1} = \mathbf{P}^-_{k+1} + \mathbf{K}_{k+1} \mathbf{P}_{\delta\mathbf{y}\delta\mathbf{y}} \mathbf{K}^\top_{k+1} \tag{3.42}$$

The numerical complexity of the UKF is the same as that of the KF and the EKF, i. e. $\mathcal{O}(n^3)$, provided also in this case by the state a-priori covariance generation. It shall be noted however, that here the prediction of $2n+1$ sigma points is needed and if highly complex integration methods are used, the overall computational demand increase.

3.3 Measurement Models

Dealing with a navigation filter, it is fundamental to analyse correctly the measurements that are exploited by the estimation algorithm, in order to be capable of simulating the behaviour of the sensors providing such observables and to find proper ways to define the measurement function used within the filter itself.

3.3.1 Optical measurements

The optical observables are in general obtained by a camera which is able to provide two angular measurements of the relative LoS $\mathbf{u}$ associated to target object. Such measures are generally defined via the two homographic coordinates, defining the projection of the LoS unit vector on the camera plane, as represented by Eq. 3.43.

$$\mathbf{u} = \begin{bmatrix} u_x \\ u_y \end{bmatrix} = f/l_{C,z} \begin{bmatrix} l_{C,x} \\ l_{C,y} \end{bmatrix} \tag{3.43}$$

$$\text{with} \quad \mathbf{l}_C = \mathbf{A}_{C/I}\mathbf{l} = \mathbf{A}_{C/I} \frac{\mathbf{r} - \mathbf{r}_{tgt}}{\|\mathbf{r} - \mathbf{r}_{tgt}\|} \tag{3.44}$$

The introduced parameters are: the focal length f, the LoS vector expressed both in camera and inertial frames $\mathbf{l}_C$ and $\mathbf{l}$, the matrix used to rotate vectors between these to frames $\mathbf{A}_{C/I}$ and $\mathbf{r}_{tgt}$ which is the target inertial position vector.

This just presented is a general formulation fundamental if a complete 6-DOF navigation system is considered, since the matrix $\mathbf{A}_{C/I}$ represent a coupling between the centre of mass and attitude kinematics. If instead, as in the scenarios under study here, the attitude is considered to be perfectly known, it is possible to consider the two angular measurements as simply the two angles that defines the LoS direction. These two are the Azimuth Az and the Elevation El coordinates, respectively in- and out-of-plane angles with respect to the inertial reference frame, and defined as in Eq.s 3.45 and 3.46.

$$Az = \arctan\left(l_y/l_x\right) + \begin{cases} \pi & \text{if} \quad l_x < 0 \\ 0 & \text{else} \end{cases} \tag{3.45}$$

$$El = \arctan\left(l_z/\sqrt{l_x^2 + l_y^2}\right) \tag{3.46}$$

In order to include measurement errors in the retrieved signals, zero mean additive white Gaussian noise is included in the simulated measurements, as in Eq. 3.47

$$\begin{cases} \tilde{A}z = Az + \varepsilon_{Az} \\ \tilde{E}l = El + \varepsilon_{El} \end{cases} \tag{3.47}$$

with the two noisy terms ε_{Az} and ε_{El} defined by a standard deviation σ_{Az} and σ_{El}.

3.3.2 RF-based measurements

Exploiting a GNSS constellation with a *One-Way* navigation strategy, the user receiver terminal retrieves from any i^{th} visible element of the constellation the range ρ, the range-rate, $\dot{\rho}$, and the servicer ephemeris under the form of the state vector $\mathbf{x}_{s,i}$. When dealing with such measurements, it is usual to define the observable data as *pseudorange* $\tilde{\rho}$ and *pseudorange-rate* $\tilde{\dot{\rho}}$, in order to indicate that the two measurements are affected by errors. In particular, looking at the range measurement, the geometric range obtained from the i^{th} servicer can be defined as per Eq. 3.48

$$\rho_i = c\Delta t_i = \|\mathbf{r}_{s,i} - \mathbf{r}\| \tag{3.48}$$

where c is the speed of light and Δt_i the time required for the signal to travel from the servicer position $\mathbf{r}_{s,i}$ to the user one $\mathbf{r}$. In a *One-Way* ranging, this time difference is obtained by subtracting the servicer clock-time at signal emission from the user clock-time at reception, i.e. $\Delta t_i = t_u - t_{s,i}$. The two clocks are however not measuring the exact time, but they will present some offsets, which will in general be different one to the other. As such the measured time difference from the user terminal will bring to the pseudorange as per Eq. 3.49.

$$\tilde{\rho}_i = c\left(t_u + \delta t_u - t_{s,i} - \delta t_{s,i}\right) = \rho_i + c\delta t_u + \varepsilon_{\delta t_{s,i}} \tag{3.49}$$

From this equation, it is clear that a bias in the measurements is present. In addition to that, there is a huge number of other possible sources of error in the pseudorange, due to RF interference effects, distortions of the signals both within the terminals or caused by interaction with the propagation medium, multipath losses, and also relativistic effects, leading to a final pseudorange formulation as per Eq. 3.50, where all the previous contributions (including $\varepsilon_{\delta t_{s,i}}$) are collapsed in a single component ε_ρ.

$$\tilde{\rho}_i = \rho_i + c\delta t_u + \varepsilon_\rho \tag{3.50}$$

The same kind of reasoning can be done for the pseudorange-rate observable, which can be derived directly from the observed frequency Doppler shift Δf_D, but again is inherently affected by the same effects as in the previous case, summed up in a $\varepsilon_{\dot{\rho}}$ term in addition to the time bias derivative.

$$\tilde{\dot{\rho}}_i = c\frac{\Delta f_D}{f_{s,i}} + c\dot{\delta t}_u + \varepsilon_{\dot{\rho}} \tag{3.51}$$

To enter the details of GNSS systems a good reference can be found in [55].

For this work, in order to simulate these effects, we implemented the model in Eq.s 3.52 and 3.53 to generate the measurements fed to the filter.

$$\tilde{\rho}_i = \|\tilde{\mathbf{r}}_{s,i} - \mathbf{r}\| + b_c + \varepsilon_\rho \tag{3.52}$$

$$\tilde{\dot{\rho}}_i = (\tilde{\mathbf{v}}_{s,i} - \mathbf{v}) \cdot (\tilde{\mathbf{r}}_{s,i} - \mathbf{r})/\rho + d_c + \varepsilon_{\dot{\rho}} \tag{3.53}$$

$$\tilde{\mathbf{x}}_{s,i} = \left[\tilde{\mathbf{r}}_{s,i}^\top, \quad \tilde{\mathbf{v}}_{s,i}^\top\right]^\top = \mathbf{x}_{s,i} + \left[\varepsilon_r^{1\times 3}, \quad \varepsilon_v^{1\times 3}\right]^\top \tag{3.54}$$

For both the observables, all the effects are directly collected in single noisy Gaussian terms, except for the receiver clock bias b_c and drift d_c contributions, which are treated as an additional parameter to be estimated. The standard deviations associated to ε_ρ and $\varepsilon_{\dot{\rho}}$ are $\sigma_\rho = 10\,\mathrm{m}$ and $\sigma_{\dot{\rho}} = 0.1\,\mathrm{m\,s^{-1}}$, values assumed in accordance to the ongoing studies [51, 52].

The receiver clock bias and drift, which represent $c\delta t_u$ and $c\dot{\delta t}_u$ respectively, are simulated with the dynamical model in Eq.s 3.55 and 3.56:

$$\dot{b}_c = d_c + \varepsilon_{b_c} \tag{3.55}$$

$$\dot{d}_c = \varepsilon_{d_c} \tag{3.56}$$

where the stochastic components ε_{b_c} and ε_{d_c} are normally distributed with null mean and assumed standard deviations of $100\,\mathrm{m}$ and $1\,\mathrm{m\,s^{-1}}$, also here consistent with [51, 52].

The servicers' ephemerides are affected by the related platforms navigation errors, which are added with a simple additive white Gaussian noise model, as in Eq. 3.54, where $\varepsilon_r^{1\times 3}$ and $\varepsilon_v^{1\times 3}$ represent the three-dimensional position and velocity error vectors, defined by standard deviations of σ_r and σ_v.

3.3.3 Additional sensors

Additional sensors that are going to be exploited in the context of this work are here presented. In particular accelerometers and altimeters are taken into consideration.

Accelerometer Concerning the accelerometers contained in the Inertial Measurement Unit (IMU) it is fundamental to recall that such sensors are insensitive to volume-forces, such as all the gravitational effects included in the environment of our simulation. They are however sensitive to SRP, which in turn may be one of the most complex effects to correctly reproduce on board, reason for which an accelerometer can be extremely useful in this scenario. Another very important contribution that can be estimated via the accelerometer is the control acceleration that the thrusters provide.

It is also relevant to recall that the accelerations recorded by the IMU are expressed in the spacecraft body frame B. Since in this framework the attitude dynamics and kinematics are not taken into consideration, the spacecraft attitude is always considered to be perfectly known, reason for which the accelerations of the IMU are directly expressed in the inertial frame.

It is possible to provide high-fidelity models to simulate the noisy measurements of the accelerometer. In general it is possible to include biases, drifts, nonlinearities, misalignment and scale errors (see [71] as a good reference). For the purpose of this work, it was decided to simplify the model, collecting all such effects into a single term. As a consequence, the simulated sensor reading is defined by the non-volume accelerations contribution affected by an additive white Gaussian noise, as per Eq. 3.57.

$$\tilde{\mathbf{a}}_{IMU,B} = \mathbf{a}_{SRP,B} + \mathbf{a}_{thr,B} + \varepsilon_{\mathbf{IMU}} \tag{3.57}$$

A consolidated practice to exploit such sensor in the orbital filters is the so-called *Dynamic Compensation Mode* [70]. The basic idea is not to use the accelerometer readings among the measurement vector, but to use it directly within the propagation step of the filter. This concept, exploited also for angular rates with gyroscopes, is backed by the high accuracies that such sensors show. Moreover, some computations savings is thus achievable, avoiding the evaluation of the non-volume forces that IMUs sense which, in general have quite complex mathematical formulations, e. g. a high-fidelity SRP or propulsive acceleration.

Altimeter Another relevant sensor that may be considered in the lunar environment is an altimeter, especially if the spacecraft under analysis is performing a controlled landing. Also for this case, there is the possibility to employ fancy models of the sensor, considering the exploited technology and the considered topography of the Moon. Regarding this latter indeed, there is a wide range of possibilities, from assuming a perfect sphere or using detailed Digital Elevation Models (DEM). In the current work, using the simpler spherical Moon model, the real altitude is obtained as in Eq. 3.58 employing Moon average radius $R_{\text{☽}}$.

$$\zeta = \|\mathbf{r}\| - R_{\text{☽}} \tag{3.58}$$

The error effects introduced by the sensor is provided by a zero-mean additive white Gaussian noise, which, to reflect the behaviour of laser altimeter technology, considers a standard deviation of 1% of the current real height [72]. The resulting measurement function is thus defined as in Eq. 3.59.

$$\tilde{\zeta} = \zeta + \varepsilon_{\zeta}(\zeta) \tag{3.59}$$

with $\varepsilon_{\zeta}(\zeta) = \mathcal{N}(0,1)\zeta/100$ defined as the noisy component.

3.3.4 Measurement uncertainty propagation

As described in section 3.2, the filtering procedure requires an estimation of the covariance associated to the measurements through the matrix $\mathbf{R}$. In order to provide such estimate it is in general sufficient to include the expected covariance of the sensors. However, in case the measurement noise cannot be considered simply as additive white Gaussian noise, it is necessary to analyse the propagation of the uncertainty from the noisy terms to the final measurement functions.

To assess the extent of such propagation, the Root of the Sum of the Squares (RSS) principle can be exploited, which states that the uncertainty of a certain variable y which is function of a series of stochastic variables x_i can be expressed as in Eq. 3.60.

$$\sigma_y = \sqrt{\sum_{i=1}^{n} \left(\frac{\partial y}{\partial x_i}\bigg|_{\bar{x}_i} \sigma_{x_i} \right)^2} \tag{3.60}$$

This formulation is obtained as an approximation in the neighbourhood of the operative conditions $\bar{x}_i$, around which the expression is linearised. As a consequence, by evaluating the partial derivatives with respect to any stochastic variable in the operative conditions $\bar{x}_i$, the uncertainty on the parameter y can be retrieved. In the following, this principle is applied to two different expressions that are going to be used for the navigation analyses.

3.3.4.1 Optical angles to Line-Of-Sight

In some scenarios it may be favourable to consider a different mathematical expression to include the optical measurements in the filter, where instead of the azimuth and elevation angles, the LoS unit vector $\mathbf{l}$ is used, as in Eq. 3.61.

$$\mathbf{l} = \Big[\cos(Az)\cos(El), \quad \sin(Az)\cos(El), \quad \sin(El)\Big]^{\top} \tag{3.61}$$

Since the actual measured stochastic quantities considered here are the bearing angles Az and El, the RSS is employed to define the uncertainty on each

component of the LoS unit vector.

$$\sigma_{l_x,\mathbf{y}} = \left(\left.\frac{\partial l_x}{\partial Az}\right|^2_{(\bar{Az},\bar{El})} \sigma^2_{Az} + \left.\frac{\partial l_x}{\partial El}\right|^2_{(\bar{Az},\bar{El})} \sigma^2_{El} \right)^{1/2} = \left(\sin(\bar{Az})^2 \cos(\bar{El})^2 + \cos(\bar{Az})^2 \sin(\bar{El})^2\right)^{1/2} \sigma_{Az} \tag{3.62}$$

$$\sigma_{l_y,\mathbf{y}} = \left(\left.\frac{\partial l_y}{\partial Az}\right|^2_{(\bar{Az},\bar{El})} \sigma^2_{Az} + \left.\frac{\partial l_y}{\partial El}\right|^2_{(\bar{Az},\bar{El})} \sigma^2_{El} \right)^{1/2} = \left(\cos(\bar{Az})^2 \cos(\bar{El})^2 + \sin(\bar{Az})^2 \sin(\bar{El})^2\right)^{1/2} \sigma_{Az} \tag{3.63}$$

$$\sigma_{l_z,\mathbf{y}} = \left(\left.\frac{\partial l_z}{\partial Az}\right|^2_{(\bar{Az},\bar{El})} \sigma^2_{Az} + \left.\frac{\partial l_z}{\partial El}\right|^2_{(\bar{Az},\bar{El})} \sigma^2_{El} \right)^{1/2} = \left(0 + \cos(\bar{El})^2\right)^{1/2} \sigma_{Az} \tag{3.64}$$

In the second passage of each Eq.s 3.62, 3.63 and 3.64, the uncertainty on the two bearing angles has been assumed to be the same, i. e. $\sigma_{Az} = \sigma_{El}$.

In order to avoid giving preferences for a specific direction in the reference frame, the trisectrix of the first octant has been taken as reference condition, thus providing the the angle of $\pi/4$ for both Az and El. As a consequence, we can evaluate the previous expressions as in the following elaboration.

$$\sigma_{l_x,\mathbf{y}} = (1/4 + 1/4)^{1/2} \sigma_{Az} = \sigma_{Az}/\sqrt{2} \tag{3.65}$$

$$\sigma_{l_y,\mathbf{y}} = (1/4 + 1/4)^{1/2} \sigma_{Az} = \sigma_{Az}/\sqrt{2} \tag{3.66}$$

$$\sigma_{l_z,\mathbf{y}} = (1/2)^{1/2} \sigma_{Az} = \sigma_{Az}/\sqrt{2} \tag{3.67}$$

The final expressions in Eq.s 3.65, 3.66 and 3.66 show that the uncertainty is equally distributed to the three components, as expected given that the defined equilibrium condition is the trisectrix. From these relationships it is possible to define an uncertainty level for each component of the LoS unit vector and thus to express the measurement covariance matrix $\mathbf{R}$ as a 3×3 matrix, as needed by the modified measurement function.

3.3.4.2 GNSS servicers ephemerides to range and range-rate

Given that the pseudorange and pseudorange-rate expressions are generated exploiting the servicers' ephemerides components, the global measurement uncertainty will be affected also by such noise. For this purpose the RSS principle is applied, for which the errors in pseudorange and pseudorange-rate derived from the ephemeris errors are given as per Eq.s 3.68 and 3.69 respectively.

$$\sigma_{\rho_i,\mathbf{x}_{s,i}} = \left(\left[\left(\frac{\partial \rho_i}{\partial x_i} \right)^2 + \left(\frac{\partial \rho_i}{\partial y_i} \right)^2 + \left(\frac{\partial \rho_i}{\partial z_i} \right)^2 \right] \sigma_r^2 + \left[\left(\frac{\partial \rho_i}{\partial v_{xi}} \right)^2 + \left(\frac{\partial \rho_i}{\partial v_{yi}} \right)^2 + \left(\frac{\partial \rho_i}{\partial v_{zi}} \right)^2 \right] \sigma_v^2 \right)^{1/2} \tag{3.68}$$

$$\sigma_{\dot{\rho}_i,\mathbf{x}_{s,i}} = \left(\left[\left(\frac{\partial \dot{\rho}_i}{\partial x_i} \right)^2 + \left(\frac{\partial \dot{\rho}_i}{\partial y_i} \right)^2 + \left(\frac{\partial \dot{\rho}_i}{\partial z_i} \right)^2 \right] \sigma_r^2 \left[\left(\frac{\partial \dot{\rho}_i}{\partial v_{xi}} \right)^2 + \left(\frac{\partial \dot{\rho}_i}{\partial v_{yi}} \right)^2 + \left(\frac{\partial \dot{\rho}_i}{\partial v_{zi}} \right)^2 \right] \sigma_v^2 \right)^{1/2} \tag{3.69}$$

Developing all the partial derivatives of range and range-rate, expressed as in Eq.s 3.52 and 3.53, the mathematical expressions remain simple for the pseudorange, while they grow quite cumbersome for the pseudorange-rate. After the simple and necessary algebraic manipulations, the resulting expressions are the following Eq.s 3.70 and 3.71.

$$\sigma_{\rho_i,\mathbf{x}_{s,i}} = \sigma_r \tag{3.70}$$

$$\sigma_{\dot{\rho}_i,\mathbf{x}_{s,i}} = \left(\left[(v_x - v_{xi})^2 + (v_y - v_{yi})^2 + (v_z - v_{zi})^2 - \dot{\rho}_i^2 \right] \sigma_r^2 / \rho_i^2 + \sigma_v^2 \right)^{1/2} = \sqrt{\alpha \sigma_r^2 + \sigma_v^2)} \tag{3.71}$$

It turns out that the position error is propagated exactly in the pseudorange when the uncertainty on the servicer ephemerides position is uniform among the three directions. Instead, for the pseudorange-rate, the effect of both ephemerides position and velocity uncertainties is present. Moreover the latter, due to the coefficient $\alpha = \alpha(\mathbf{v}, \mathbf{v}_{s,i})$ showing dependence on the current values of the velocity components for both user and servicers, cannot be used directly in this formulation. To avoid having an adaptive formulation, the expression of the coefficient α is evaluated a-priori as the mean value experienced on the simulated trajectories of four different LLO users from 10 km to 250 km. The values of the ephemeris error standard deviation are σ_r =15 m and σ_v =0.15 m s^{-1}, compatible with orbit determination performance studied for lunar constellation elements (see [19]).

CHAPTER 4

Autonomous Navigation for Cislunar Proximity Operations: the Rendezvous and Formation Flying scenarios

The first two scenarios objective of this thesis are inserted in the framework of the relative dynamics in the cislunar space. In particular in both scenarios the target of the study is the proximity operations involving the Lunar Orbital Platform - Gateway, thus involving the associated NRHO. The first case study involves the completion of a rendezvous with the Gateway, while the second one considers instead a formation flying mission, where the chaser needs to perform reconfiguration manoeuvres. The details of the operative environment in which the LOP-G will work are described in Section 4.1.

The rendezvous study presented in Section 4.2 focuses on assessing the applicability of the already known approaches to perform proximity navigation on Earth orbits, to the cislunar environment. In particular, the BO technique presented in Chapter 2 is here selected as potentially available, from a sensor suite perspective, on all spacecraft classes, from nano to large satellites. Although this technique requires simple, cheap, and lightweight navigation

sensors, its application in the space environment has been sparsely studied because of inherent limitations in estimating the range.

Nevertheless, little to no literature exists regarding the applicability of bearing-only navigation to perform proximity operations in non-Keplerian orbits. Therefore the goal of this analysis is to develop a novel approach to favour the target observability while respecting traditional rendezvous requirements in the cislunar domain.

Following this goal, Subsection 4.2.1 provides a detailed description of the mathematical formulation behind the proposed GNC architecture, while two different set of rendezvous simulations are presented in Subsection 4.2.2. Subsection 4.2.3 exploits instead the very same architecture for heterogeneous orbits scenarios.

The goal of the second scenario proposed in Section 4.3 of this chapter is to provide a cost effective GNC strategy to perform reconfiguration manoeuvres, or *rephasing*, of a chaser spacecraft around the LOP-G. First, a scheme is built to target and move between natural relative trajectories around the Gateway orbit, exploiting the peculiar features of quasi-periodic invariant tori in Subsection 4.3.1. Then in Subsection 4.3.2, the design of the guidance and control scheme is tackled, using a Model Predictive Control based on an adaptive weights formulation and employing maximum thrust and collision avoidance constraints. The resulting transfers assuming perfect state knowledge are presented and discussed in Subsection 4.3.3. The problem of navigation is introduced afterwards, starting by defining the state reconstruction requirements. The BO strategy is first applied to assess its validity and eventually enhanced also with radiometric measurements to meet the found navigation requirements.

4.1 The LOP-G Operative Scenario

The Lunar Orbital Platform - Gateway is located on a Near Rectilinear Halo Orbit, with a resonant period with the Moon (9:2), a periselene and an aposelene of 3200 km and 70 000 km approximately, and an orbital period of 6.5 d. The orbit is reconstructed leveraging the initialisation, correction, and continuation scheme of orbital families, starting from the bifurcation point between Lyapunov and Halo orbits [73]. Figure 4.1 depicts the operative NRHO in the CR3BP and in a high fidelity model, including Earth and Moon ephemerides, Sun fourth-body gravity, and Solar radiation pressure. It can be observed how the high-fidelity motion mildly deviates from the CR3BP solution ($\sim$ 2300 km at the apolune in a time range of 30 days), thus substantiating the validity of the latter model for the preliminary analyses, to be then cross-validated against the high fidelity model.

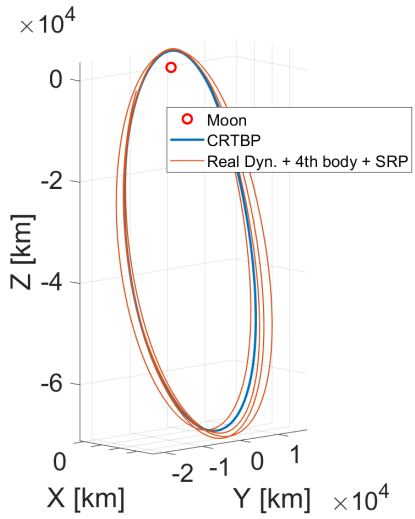

Figure 4.1: NRHO in the CR3BP, and in high-fidelity dynamics

4.2 GNC for Rendezvous in cislunar space

This first scenario sees the design and testing of a GNC system to successfully perform a rendezvous manoeuvre with the LOP-G, navigating with LoS angles with respect to the target spacecraft only, exploiting the BO guidance and control scheme to enhance the range observability. In addition to a rendezvous scenario the same scheme is tested in bounded-distance heterogeneous orbits scenarios.

4.2.1 Bearing-Only GNC

As seen in section 2.2.1.1, when dealing with a bearing-only architecture, the navigation process is directly influenced by the shape of the trajectory, therefore the main strategy proposed here is to include inside the guidance a contribution that allows to improve the navigation performance. A Shrinking Horizon MPC is selected to compute the manoeuvres required to bring the spacecraft to a desired location. In this formulation, the trajectory is discretised into a series of points, uniformly distributed in time. The course of action for this kind of architecture is displayed in Fig. 4.2. Applying operational and safety constraints related to the completion of the manoeuvre before entering dynamically unfavourable regions, the time of flight is fixed to the desired rendezvous time T_{rdv} and the trajectory is discretised into n steps $t_M = [t_{M_1}, t_{M_2}, ..., t_{M_n}]$ at which manoeuvres are envisioned. At the same time, a number of m re-optimisations of the control actions are scheduled for $t_O = [t_{O_1}, t_{O_2}, ..., t_{O_m}]$, such that t_{O_i} does not necessarily equal t_{M_i}. Once the procedure is initialised, for each update time t_j the need for a re-optimisation

is checked and if that is the case, the guidance uses the estimated relative state as the initial point to searches a solution for the remaining window, eventually updating the manoeuvre scheme $\mathbf{U}_{opt}$. Afterwards, it also controls if a manoeuvre is planned; whenever that is the case, the chaser executes the control action according to $\mathbf{U}_{opt}$. Finally, the cycle is stopped when the shrinking horizon window ends, i. e. at $t_k = T_{rdv}$.

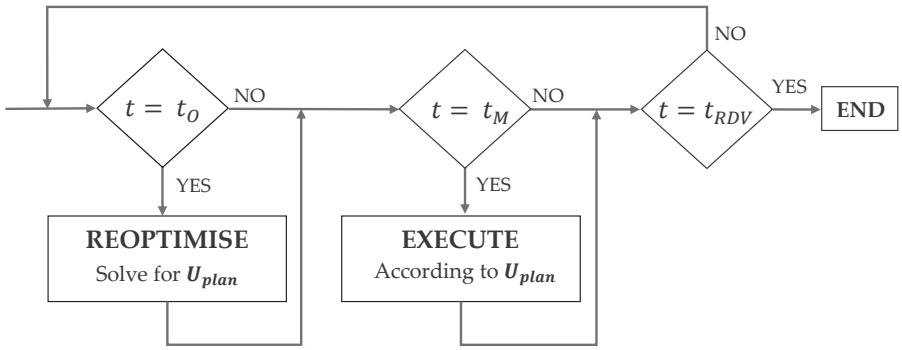

Figure 4.2: Guidance Flow-chart.

This kind of scheme represents a slight readaptation of the basic shrinking horizon MPC, since in this case the re-optimisation of the manoeuvre sequence within the finite horizon is not forced to occur at the same time instants of the manoeuvres.

In the next subsections the formulations of the dynamical model and optimisation problem are reported.

4.2.1.1 Guidance and Control Dynamic Model

Given the specific goal of bringing to zero the relative distance to complete the rendezvous, the MPC is here in charge of providing both a guidance, i. e. defining the trajectory to follow, and the control. In this framework, considering the environmental condition in which the LOP-G, the target spacecraft, is operative, the relative CR3BP dynamics in its linearised formulation of Eq. 2.9 comes at hand.

A closed form solution to these equations system does not exist since the dynamics Jacobian $\mathbf{A}(t)$ is dependent on the absolute dynamics of the target, which requires a numerical integration. Nevertheless, given the initial state $\mathbf{x}_k$ at a time t_k and the control action $\mathbf{u}_k$ the solution of any nonlinear similar equation of motion can be separated into a free and forced contribution as in a

discrete time formulation:

$$\mathbf{x}_{k+1} = e^{A_k(t_{k+1}-t_k)}\mathbf{x}_k + \int_{t_k}^{t_{k+1}} e^{A_k(t_{k+1}-\tau)} B_k \mathbf{u}_k(t)\, d\tau \tag{4.1a}$$

$$A_k = \frac{\partial \mathbf{f}(\mathbf{x}_k)}{\partial \mathbf{x}_k} \tag{4.1b}$$

$$B_k = \frac{\partial \mathbf{g}(\mathbf{u}_k)}{\partial \mathbf{u}_k} \tag{4.1c}$$

where $\mathbf{f}(\mathbf{x}_k)$ and $\mathbf{g}(\mathbf{u}_k)$ are the collection of nonlinear terms, function of the state and of the input respectively.

Approximating the exponential terms with a 2nd order Taylor series, the State-Transition Matrix A_k^{k+1} is expressed as in Eq. 4.2b. The solution of the forced response is instead more complicated and only in few cases the convolution integral of the time-varying manoeuvre $\mathbf{u}_k(t)$ can be written as the product between a matrix and a vector. For impulsive controls at the beginning of the time interval, however the solution of the integral B_k^{k+1} can be computed simply with the input matrix B_k and the State-Transition Matrix (STM) A_k^{k+1} as in Eq. 4.2c. The resulting expression of the discrete linearised dynamics becomes simply as in Eq. 4.2a.

$$\mathbf{x}_{k+1} = A_k^{k+1}\mathbf{x}_k + B_k^{k+1}\mathbf{u}_k \tag{4.2a}$$

$$A_k^{k+1} = I + A_k(t_{k+1} - t_k) + (A_k^2 + \dot{A}_k)(t_{k+1} - t_k)^2/2 \tag{4.2b}$$

$$B_k^{k+1} = A_k^{k+1} B_k \tag{4.2c}$$

Then, a generic (k+j)th state can be expressed as function of the initial state $\mathbf{x}_k$ and the sequence of control actions from initial node to the (k+j-1)th node

$$\begin{aligned}
\mathbf{x}_{k+j} &= A_{k+j-1}^{k+j}\mathbf{x}_{k+j-1} + B_{k+j-1}^{k+j}\mathbf{u}_{k+j-1} \\
&= A_{k+j-1}^{k+j}\left(A_{k+j-2}^{k+j-1}\mathbf{x}_{k+j-2} + B_{k+j-2}^{k+j-1}\mathbf{u}_{k+j-2}\right) + B_{k+j-1}^{k+j}\mathbf{u}_{k+j-1} \\
&\quad \ldots \\
&= \prod_{i=j-1}^{0} A_{k+i}^{k+i+1}\mathbf{x}_k + \\
&\quad + \left[\prod_{i=j-1}^{1} A_{k+i}^{k+i+1}B_k^{k+1},\ \prod_{i=j-1}^{2} A_{k+i}^{k+i+1}B_{k+1}^{k+2},\ \ldots,\ B_{k+j-1}^{k+j}\right]\begin{bmatrix}\mathbf{u}_k \\ \vdots \\ \mathbf{u}_{k+j-1}\end{bmatrix}
\end{aligned} \tag{4.3}$$

Note that the products involved are in reversed order, i. e. considering e. g. $j = 5$, the product $\prod_{i=j-1}^{0}$ starts with the index $i = 4$ and ends with $i = 0$. The matrix products are intended as left-side multiplications.
This formulation provides a simple manner to express any states within the

finite horizon of the MPC as function of the initial state $\mathbf{x}_k$ of the window, and the set of control actions $\mathbb{U}$. In particular, we can compact the state at any particular step $k+j$ as in Eq. 4.4

$$\mathbf{x}_{k+j} = \mathbb{A}_k^{k+j}\mathbf{x}_k + \mathbb{B}_k^{k+j}\mathbb{U}_k^{k+j} \tag{4.4}$$

$$\mathbb{A}_k^{k+j} = \prod_{i=j-1}^{0} A_{k+i}^{k+i+1} \tag{4.5}$$

$$\mathbb{B}_k^{k+j} = \left[\prod_{i=j-1}^{1} A_{k+i}^{k+i+1}B_k^{k+1}, \prod_{i=j-1}^{2} A_{k+i}^{k+i+1}B_{k+1}^{k+2}, \quad \ldots, \quad B_{k+j-1}^{k+j}\right] \tag{4.6}$$

$$\mathbb{U}_k^{k+j} = \begin{bmatrix} \mathbf{u}_k \\ \vdots \\ \mathbf{u}_{k+j-1} \end{bmatrix} \tag{4.7}$$

Applied to the final state of the finite horizon window at $t = t_n$, Eq. 4.8

$$\mathbf{x}_n = \mathbb{A}_k^n\mathbf{x}_k + \mathbb{B}_k^n\mathbb{U} \tag{4.8}$$

where the complete set of computed control actions from step k to step n, has been renamed as $\mathbb{U}$, a $3(n-1)\times 1$ vector.

This compact notation will be useful to simplify the optimisation problem described in the following subsection.

4.2.1.2 Optimisation Problem

The optimisation problem solved at each re-optimisation epoch is written as:

$$\begin{aligned} \min_{\mathbf{y}} \quad & \mathcal{J}_F(\mathbf{y}) && \text{(4.9a)} \\ \text{subject to} \quad & \mathbf{A}_{eq}\mathbf{y} = \mathbf{b}_{eq} \\ & \mathbf{A}_{iq}\mathbf{y} \leq \mathbf{b}_{iq} \\ & \mathbf{l}_b \leq \mathbf{y} \leq \mathbf{u}_b \\ & c(\mathbf{y}) \leq 0 \end{aligned}$$

where $\mathbf{y}$ is the vector of optimisation variables, among which the controls and other associated quantities can be present. Equality and inequality constraints are imposed linearly with the matrices $\mathbf{A}_{eq}$ and $\mathbf{A}_{iq}$ or nonlinearly with $c(\mathbf{y})$, while the upper and lower bounds for the optimisation variables are defined respectively by $\mathbf{u}_b$ and $\mathbf{l}_b$.

Fuel Objective Generally the fuel expenditure is quantified by the Δv, which however can be expressed only in a nonlinear fashion with respect to the vector $\mathbf{y}$, due to the squared root in its definition. To avoid dealing with a nonlinear cost function in this study the cost function will be expressed both as a quadratic $\mathcal{J}_{F,q}$ or linear $\mathcal{J}_F$ function.

Considering the quadratic formulation, we can write the cost function as in [74], i. e. :

$$\mathcal{J}_{F_q} = \frac{1}{2}\mathbb{U}^T \mathcal{Q}\mathbb{U} \tag{4.10}$$

where the diagonal matrix $\mathcal{Q}$ is exploited to favour the control actions at certain time-steps within the window. In this cost function, the variable $\mathbf{y}$ is represented by the stacked manoeuvres vector $\mathbb{U}$. The quadratic formulation in general provides smooth controls, resulting in a more robust dynamics with respect to disturbances and off-nominalities. Nevertheless, its output may result less optimal in terms of Δv with respect to a linear formulation of the control action as described in [75].

The linear representation of the fuel expenditure is instead provided by using the 1-norm of the control action, which is the sum of of all the components of $\mathbb{U}$ taken in absolute value:

$$\mathcal{J}_{F_s} = \sum_{k=1}^{3(n-1)} |\mathbb{U}_{(k)}| \tag{4.11}$$

This formulation provides smaller Δv with respect to the quadratic objective. Moreover the control action results also in sparser executions, which can be an interesting feature when continuous thrust is not a viable option. The disadvantage of this behaviour is that the strategy is less robust to thrust-misses.

To efficiently solve the optimisation problem with a Sequential Quadratic Programming (SQP) solver, it is advisable to remodulate the objective in Eq. (4.11) since it is a piece-wise linear function. Additional optimisation variables $\mathbb{S} = [\mathbf{s}_1^\top \ \mathbf{s}_2^\top \ ... \ \mathbf{s}_{n-1}^\top]^\top$, called slack variables as in [21], are thus introduced. Additional inequality constraints are added, such that the elements in $\mathbb{S}$ are forced to have the same absolute value of their related elements in $\mathbb{U}$.

With $\mathbf{Y} = [\mathbb{U}^\top \mathbb{S}^\top]^\top$ the augmented optimisation variables, Eq. (4.11) is recast as:

$$\mathcal{J}_{F_s} = \mathbf{F}^\top \mathbf{Y} \tag{4.12}$$

where the first $3(n-1)$ elements of $\mathbf{F}$ are null and the remaining ones are unity. The constraints on the slack variables are instead:

$$\mathbb{U}_j - \mathbb{S}_j \leq 0 \tag{4.13}$$

$$-\mathbb{U}_j - \mathbb{S}_j \leq 0 \tag{4.14}$$

which can be expressed in matricial form to include all the control actions as:

$$\mathbf{A}_s\mathbf{Y} \leq \mathbf{b}_s \tag{4.15}$$

$$\mathbf{A}_s = \begin{bmatrix} \mathbf{I}_{m\times m} & -\mathbf{I}_{m\times m} \\ -\mathbf{I}_{m\times m} & -\mathbf{I}_{m\times m} \end{bmatrix} \tag{4.16}$$

$$\mathbf{b}_s = \mathbf{0}_{2m} \tag{4.17}$$

with $m = 3(n-1)$.

Recall that the introduction of slack variables can be avoided by using directly a nonlinear solver, however the solver is much faster when the cost function is continuous and smooth.

Boundary Conditions The completion of the rendezvous is enforced through boundary conditions at the end of the horizon window, which is expressed as function of the control vector $\mathbb{U}$ and the initial conditions, as in Eq. 4.8, leading to:

$$\mathbf{A}_{BC}\mathbf{Y} = \mathbf{b}_{BC} \tag{4.18}$$

$$\mathbf{A}_{BC} = \begin{cases} \begin{bmatrix} \mathbb{B}_k^n & \mathbf{0}_{6\times m} \end{bmatrix} & \text{for} \quad \mathcal{J}_{F_s} \\ \mathbb{B}_k^n & \text{for} \quad \mathcal{J}_{F_q} \end{cases} \tag{4.19}$$

$$\mathbf{b}_{BC} = \hat{\mathbf{x}}_{EC} - \mathbb{A}_k^n\mathbf{x}_k \tag{4.20}$$

where the desired final point is $\hat{\mathbf{x}}_{EC}$.

Upper and lower bounds are instead used to impose the maximum thrust constraint, decoupling the three axes:

$$\begin{aligned} \mathbf{l}_b &= -u_m \begin{bmatrix} \mathbf{1}_{1\times m} & \mathbf{1}_{1\times m} \end{bmatrix}^\top \\ \mathbf{u}_b &= \quad u_m \begin{bmatrix} \mathbf{1}_{1\times m} & \mathbf{1}_{1\times m} \end{bmatrix}^\top \end{aligned} \tag{4.21}$$

Due to the discrete formulation of the original problem in Eq. 4.2a, u_m is expressed as a velocity and equals the maximum Δv available for each manoeuvre.

Observability cost function The approach of Grzymisch [21] is based on an MPC guidance adding also an observability cost function, denoted as $\mathcal{J}_O$, exploited to enforce the positive linear independence between the natural and the perturbed relative position vectors, as in Eq. 4.22. Here, the sum of the scalar products between the perturbed LoS vectors and the natural ones is minimised for each time-step within the horizon window.

$$\mathcal{J}_O = \sum_{j=2}^{n-1} \bar{\mathbf{r}}_j^\top \mathbf{r}_j = \sum_{k=1}^{n-2} (\Lambda_k^{k+1}\mathbf{x}_k)^\top (\Lambda_k^{k+1}\mathbf{x}_k + \Gamma_k^{k+1}\mathbf{u}_k) \tag{4.22}$$

In the previous expression, the matrices Λ_k^{k+1} and Γ_k^{k+1} are defined as only the first three rows of A_k^{k+1} and B_k^{k+1} respectively, thus with the same functionality but providing only the position vector instead of the full state. By developing the cumbersome algebra, with a process similar to the one that led to the Eq. 4.4, the resulting objective function can be expressed as a quadratic formulation of the $\mathbb{U}$ vector only, as in Eq. 4.23

$$\mathcal{J}_O = \frac{1}{2}\mathbb{U}^\top \mathbb{H}\mathbb{U} + \mathbb{L}^\top \mathbb{U} + \mathbb{C} \tag{4.23}$$

$$\mathbb{H} = \begin{bmatrix} \mathbb{H}_{11} & \mathbb{H}_{21} & \dots & \mathbb{H}_{1(n-1)} \\ \mathbb{H}_{21} & \mathbb{H}_{22} & \dots & \mathbb{H}_{2(n-1)} \\ \vdots & \vdots & \ddots & \vdots \\ \mathbb{H}_{(n-1)1} & \mathbb{H}_{(n-1)2} & \dots & \mathbb{H}_{(n-1)(n-1)} \end{bmatrix} \tag{4.24}$$

$$\mathbb{L} = \begin{bmatrix} \mathbb{L}_1^\top & \mathbb{L}_2^\top & \dots & \mathbb{L}_{(n-1)}^\top \end{bmatrix}^\top \tag{4.25}$$

with the different terms defined as in the following, where the Kronecker delta δ_{ij} is used.

$$\mathbb{H}_{ij} = \Gamma_i^{i+1\,\top} \Lambda_i^{i+1} \mathbb{A}_{j+1}^i \mathbb{B}_j^{j+1} (1 - \delta_{ij}) + \\ + 2 \left[\sum_{k=j+1}^{n-2} \mathbb{B}_i^{i+1\,\top} \mathbb{A}_{i+1}^{k\,\top} \Lambda_k^{k+1\,\top} \Lambda_k^{k+1} \mathbb{A}_{j+1}^k \mathbb{B}_j^{j+1} \right] \quad \text{for} i \geq j \tag{4.26}$$

$$\mathbb{L}_j = \mathbf{x}_1^\top \mathbb{A}_1^{j\,\top} \Lambda_j^{j+1\,\top} \Gamma_j^{j+1} + 2\mathbf{x}_1^\top \left[\sum_{k=j+1}^{n-2} \mathbb{A}_1^{k\,\top} \Lambda_k^{k+1\,\top} \Lambda_k^{k+1} \mathbb{A}_{j+1}^k \mathbb{B}_j^{j+1} \right] \tag{4.27}$$

$$\mathbb{C} = \mathbf{x}_1^\top \left[\sum_{k=j+1}^{n-2} \mathbb{A}_1^{k\,\top} \Lambda_k^{k+1\,\top} \Lambda_k^{k+1} \mathbb{A}_{j+1}^k \right] \mathbf{x}_1 \tag{4.28}$$

This cost function is quadratic in the optimisation variables and is combined with the fuel objective through a weighted-sum approach. The resulting problem can be solved with Quadratic Programming (QP) algorithms. An important note is that $\mathcal{J}_O$ can be minimised by either changing the angle between the two vectors (i.e., θ) or reducing their magnitude (i.e., moving closer to the target). This effect will be looked at particularly in the next sections.

Non-linear Observability Constraint Another possibility to include the observability angle inside the optimisation problem is to augment Eq. 4.9 with a non-linear constraint, which acts to impose that θ is larger than a certain

threshold after M steps, which can be used as a tuning parameter. Such constraint can be expressed as:

$$c(\mathbb{U}) = \theta_{thr} - \cos^{-1}\left(\frac{\bar{\mathbf{x}}_M^\top \mathbf{x}_M(\mathbb{U})}{\|\bar{\mathbf{x}}_M\|\|\mathbf{x}_M(\mathbb{U})\|}\right) \leq 0 \tag{4.29}$$

where $\bar{\mathbf{x}}_M$ depends only on the initial conditions. Using the compact formulation we can express the two vectors as:

$$\begin{aligned} \bar{\mathbf{x}}_M &= \mathbb{A}_k^M \mathbf{x}_k \\ \mathbf{x}_M &= \bar{\mathbf{x}}_M + \mathbb{B}_k^M \mathbb{U}_k^M \end{aligned} \tag{4.30}$$

This formulation gives rise to a Nonlinear Programming (NLP) problem, that requires, unfortunately, iterative and more time-consuming procedure to be solved. However, its advantages in the associated guidance and navigation performance will be evident in the next sections.

4.2.2 Simulation Environment and results

To investigate the ability of the proposed architecture to perform an autonomous bearing-only rendezvous, the Shrinking Horizon - MPC guidance is tested in a closed-loop system along with a navigation filter. The target considered is the LOP-G, and its operative orbit the southern NRHO introduced in Section 4.1.

The apolune region of the NRHO is considered as the reasonable area to complete the rendezvous operations as also highlighted by previous studies [30, 76]. This region is dynamically very stable and due to the relatively low velocity involved, as opposed to the perilune neighbourhood, where very small perturbations are able to generate large trajectory deviations (see [77]).

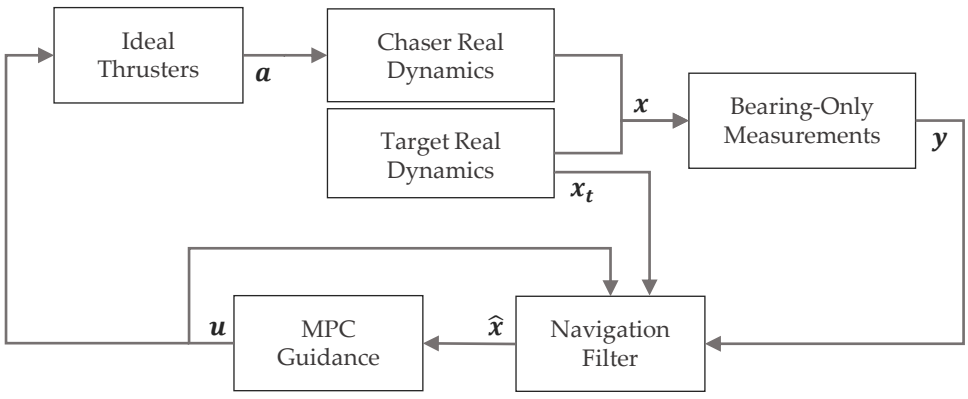

Figure 4.3: Simulation architecture scheme.

Figure 4.3 presents the architecture of the GNC scheme considered, implementing the logic in Fig. 4.2. The ground-truth considers a full-ephemerides high-fidelity propagation, including the perturbations of the Sun gravity and the SRP. The target spacecraft mass is assumed as 400 000 kg with an SRP-effective area of 12 000 m^2, similar to an ISS-class structure. The chaser instead is taken as automated transfer vehicle, with 20 000 kg of mass and 125 m^2 of total surface.

Given that the navigation filter requires the knowledge of the target absolute state, it is assumed that at each re-optimisation step this information is obtained through an RF link from the target to the chaser. This latter uses it as initial condition and propagates it onboard within the horizon window, obtaining thus a cooperative GNC strategy.

The navigation filter employed here is an Extended Kalman Filter, with the dynamics based on Eq. 4.2a, the STM provided by Eq. 4.2b and the update frequency set to 1 Hz. The re-optimisation time step is fixed to 1 h, while the dynamics discretisation to 600 s. The selection of such parameters is relevant for many aspects, both in terms of performance of the GNC scheme and of operational and technical compliance, requiring thus a proper trade-off to be sorted out. Indeed, it is possible to enhance the performance in both estimation and propellant aspects by increasing the filter frequency or by decreasing the re-optimisation and dynamics discretisation, respectively. Concerning the filter frequency however, the value of 1 Hz can be considered as a maximum value, limited by the capability of ingesting and processing optical images at higher frequency. Regarding the re-optimisation time, reducing it even more would counteract the benefits of employing the model predictive strategy, letting the system evolve not so much to generate a deviation between the on-board dynamics and the physical reality.

In order to obtain a more reliable propagation of the target position, it is expressed in the inertial frame. Regarding the navigation performance the threshold for good estimation is set to 0.5% of the range. Moreover a Monte-Carlo analysis with a total of 300 simulations is considered, varying the initialisation of the filter and the related noise effects.

Two Holding Points (HP) are used to identify the desired initial and final relative states. In a practical rendezvous approach, these points are used as checkpoints: they allow to account for operational constraints by enforcing few desired relative positions throughout the approach. Both BO guidances are tested in these two scenarios, namely the QP and the NLP case. The former represents the approach with the observability added as an additional cost function (combined with the fuel objective with a weighted sum), the latter with the nonlinear constraint.

4.2.2.1 Case A: Center Manifold

Case A considers as initial holding point a state on the NRHO center manifold, at a distance of 250 km from the target. The main feature of this point is that it presents a periodic simply stable motion around the target, consequently this can guarantee that in case of malfunctioning at the start of the approach, the chaser does not drift from the target. The second holding point is instead posed on the unstable manifold at the 1 km Keep-Out-Sphere, such that it guarantees a passively safe trajectory in case of non-nominalities as described in [76]. The time of flight is imposed to be 12 h.

Table 4.1: Center manifold navigation performance.

	Δv [m/s]	E_m [km]	R_{con} [km]	δr_{NAV} [m]	δr_{CTRL} [m]
QP	25.06	1.22	29.16	0.84	17.76
NLP	21.58	1.04	124.42	0.91	23.20

The results of the simulations are summarised in Table 4.1. In the latter E_m is the average value of the Root Mean Square Error (RMSE) of the estimated position and R_{con} is the relative distance at which the filter reaches the desired accuracy. δr_{NAV} and δr_{CTRL} are the final navigation and position mean errors (1σ), respectively.

Results are also visually represented in Fig. 4.4, where from the left figure, it is clear that the NLP formulation acting directly on the observability angle, can suddenly reduce the relative navigation error. The observability of the system greatly improves with the manoeuvring actions after 1 hour, which makes the estimate error drop of ∼3000 m, keeping a higher target-distance compared to the QP alternative. The evolution of the range shows some insight on how this latter strategy based also on the range information behaves. At the downside of higher initial fuel expenses, it favours a quick reduction of the relative distance, which however does not provide convenience from the operational point of view. Indeed the accuracy threshold in the navigation is crossed at a quite advanced stage of the rendezvous.

From Table 4.1 we see that the strategy exploiting $\mathcal{J}_o$ present a very small distance at which the accuracy threshold is crossed. This is due to a reduction of the range accompanied by a very small value of θ.

As such, there is the possibility that such trajectories may not comply with stringent requirements for a safe rendezvous with the LOP-G. The NLP

approach instead provides a threshold crossing from ∼125 km of distance to the target.

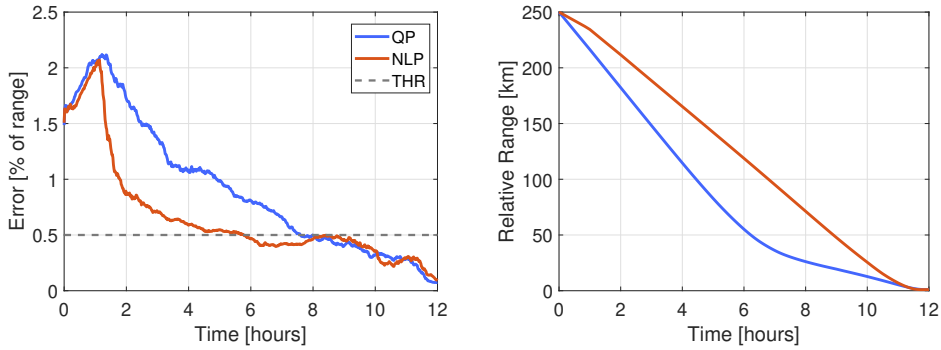

(a) Relative navigation error. **(b)** Relative distance.

Figure 4.4: Performance of the bearing-only guidance with the initial point on a center manifold

4.2.2.2 Case B: Quasi-Periodic Orbit

In this second test, the starting holding point is placed on a periodic mode of the NRHO, where the unperturbed dynamics provides an along-track formation due to the spacecraft being on the same orbit with an arbitrary phase displacement. The final holding point is the same of the previous case on the unstable manifold. The rendezvous time imposed is of 8 h.

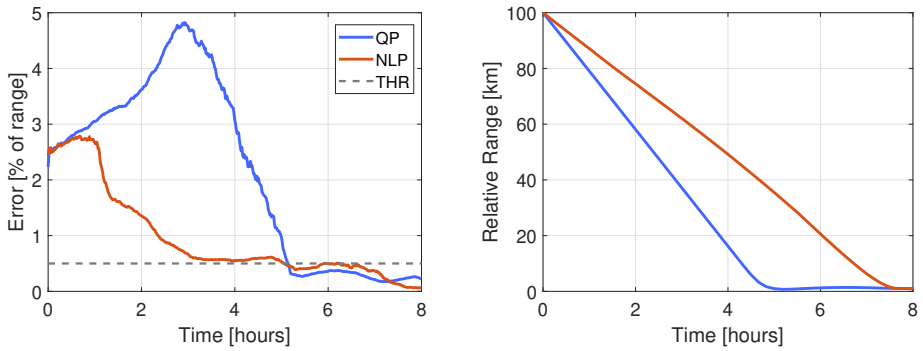

(a) Relative navigation error. **(b)** Relative distance.

Figure 4.5: Performance of the bearing-only guidance with the initial point on a quasi-periodic mode

The performance in this case is quite different with respect to the previous one, as Fig. 4.5 highlights. The QP strategy indeed provides initial manoeuvres which are not able to improve the estimation until half of the rendezvous time.

The navigation performance reaches adequate values only at very close distances to the target, near to the Keep-out-sphere. If we look at the navigation error at a 30 km distance from the target, we see almost 10 times the required threshold.

Table 4.2: Periodic mode navigation performance.

Method	Δv [m/s]	E_m [km]	R_{con} [km]	δr_{NAV} [m]	δr_{CTRL} [m]
QP	12.64	1.01	1.03	2.21	6.81
NLP	15.51	0.67	34.67	0.67	25.78

Figure 4.6 provides additional way to inspect this results. There we see the natural nominal trajectory (the violet line, without propulsion) with an initial motion perpendicular to the x-y plane, while the QP solution (blue line) straightly reaches the target parallel to the y-axis. With such a geometry, the difference in the bearing angle from an azimuth point of view is very reduced, as the left plot shows. Thus, the capability to reduce the uncertainty in the y-axis is very reduced, with an improvement in the estimation only after 3 h, when the natural trajectory starts bending to the positive x-axis.

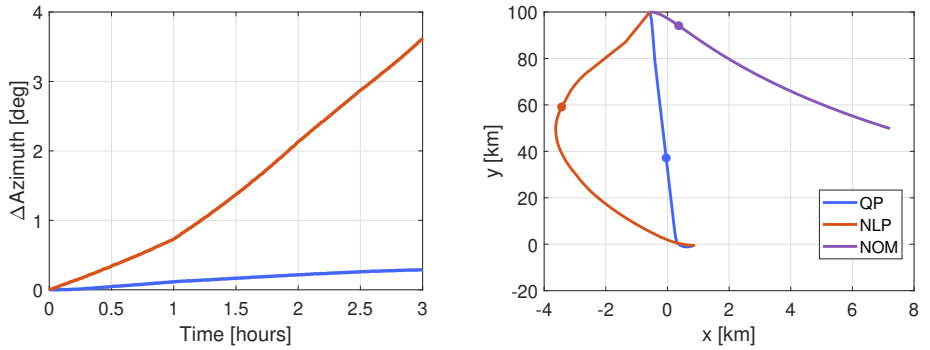

(a) Azimuth differences. **(b)** Trajectory projection in the x-y plane.

Figure 4.6: Approaching trajectories characteristics. NOM stands for the nominal trajectory without manoeuvring and the dots represent the relative position of the chaser after 3 h.

What we see instead in the results of the NLP guidance is that the manoeuvre after 1 h brings the chaser in an opposite direction with respect to the natural trajectory. This change in the geometry provides an improvement of the navigation performance, reducing the error by around 1000 m. Regarding the final position error, the NLP formulation provides worse dispersion, due to its

higher absolute state estimation error during its last re-optimisation window. The QP formulation instead, remaining for longer time in close proximity of the target, has already a good absolute state estimation at the time of the last re-optimisation step.

In general the results show that enhancing the observability with the additional term $\mathcal{J}_o$ in the cost function provides better results in terms of final control error, with minimal dispersion (in the order of few metres). If however the goal is to guarantee the maximum safety in terms of relative navigation error, the approach with the QP is not feasible. Instead the NLP strategy performs greatly under both points of view, providing much good relative estimation error at much larger distances (thus much sooner), while keeping good scores in the other metrics. Moreover it is possible also to improve even more the final position dispersion by introducing more frequent re-optimisation steps towards the final part of the rendezvous.

4.2.3 Heterogeneous orbits

A different set of scenario is tested instead in the following section. The basic idea is to analyse the effectiveness and related performance of a navigation system leveraging the BO guidance, in a different mission case, where instead of a rendezvous mission, a bounded motion between two cooperative spacecraft (here still named *chaser* and *target*) is forsaken. The test case is selected remaining in the cislunar region, thus still targeting the environment of interest for the next decades lunar exploration missions.

The selected scenarios involve two spacecraft flying on heterogeneous non-Keplerian orbits, with distances in the order of thousands of kilometres. Being the goal here to enhance the navigation without affecting the trajectory of the chaser after the execution, a final boundary condition is imposed, to ensure that the final state lies on the very same initial trajectory.

Two different orbital family couples are analysed here, with the target always placed in a DRO and the chaser first on a planar Lyapunov, then on a Halo orbit. The BO guidance in its NLP configuration is coupled with an UKF used to re-construct the relative state, with an update frequency of 0.1 Hz. Finally, to stress the architecture robustness and statistically evaluate the navigation performance, 100 Monte Carlo simulations are run for each scenario, changing the filter initialisation and the noise effects.

4.2.3.1 Lyapunov to DRO Navigation

For the first case, the chaser is settled on a L2 Lyapunov while the target is on a DRO, with an initial distance between the two spacecraft of 5300 km. The navigation filter is initialised with relative position and velocity uncertainties

of 10% and 2.5%, respectively, in order to provide reasonable initial navigation errors. The observability angle is imposed through the nonlinear constraint approach to three different limited values, namely 2.5, 5 and 7.5°, while the two fuel cost functions $\mathcal{J}_{F_s}$ and $\mathcal{J}_{F_q}$, linear (with slack variables) and quadratic respectively, are tested and compared. Moreover, being the target final state on the initial same orbit, the final value of θ is null. The time at which the observability is constrained is half of the simulation, for which the resulting symmetry ensures the lowest fuel expenditure. The total simulation time is 72 h, using a re-optimisation time step of 5 h and a discretisation time of 1800 s.

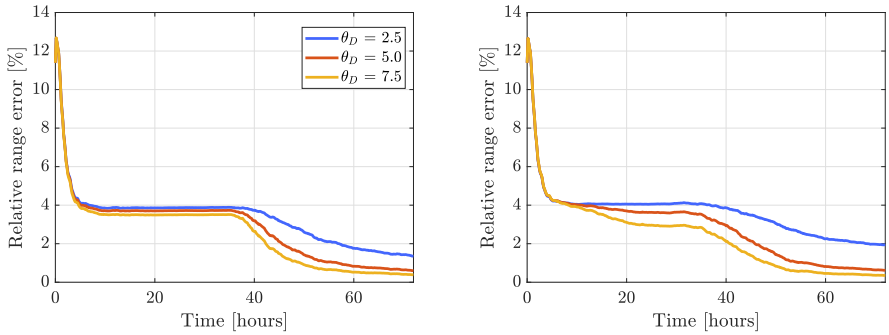

(a) Linear fuel objective. **(b)** Quadratic fuel objective.

Figure 4.7: Relative position error for the two cost functions considered.

The two cost function formulations provide similar state reconstruction performance, even though the quadratic one presents an increment of $10\,\mathrm{m\,s^{-1}}$ in Δv.

Looking at the relative position errors, we find a minimum around 0.4% of the range, corresponding to 60 km of estimation error (associated to an imposed angle of 7.5°). Considering the initial range of ∼5300 km and the filter initialisation with 10% of relative error, we see a total reduction of 10 times the initial value.

We can notice how the linear case presents a drop in the relative range error after the initial manoeuvre, while remaining almost constant for very long up to the time of θ enforcement. Anyway, due to the increasing distances (from 5300 km up to 16 500 km), we see an absolute navigation error that increases accordingly, as viewable in Fig. 4.8a and 4.8b.

Figure 4.9b shows that by solving for the quadratic fuel objective, the impulsive approximation of the forced response effectively approximates the behaviour of a low-thrust continuous control. This result is extremely useful since the convolution integral of a generic continuous thrust vector $\mathbf{u}(t)$, cannot be

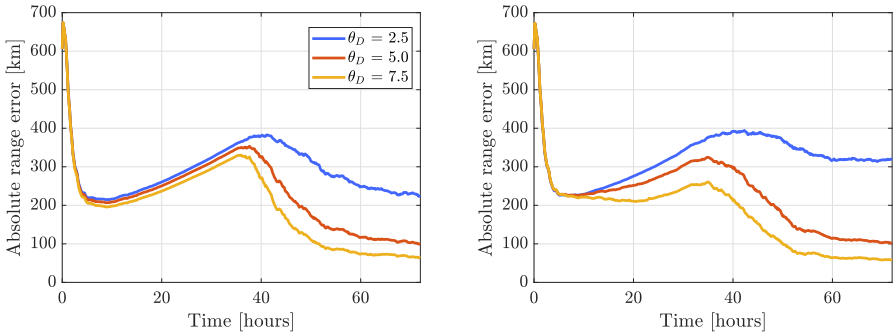

(a) Linear fuel objective. **(b)** Quadratic fuel objective.

Figure 4.8: Absolute position error for the two cost functions considered.

written in discrete form as the product between a matrix and a vector. Thus, the quadratic objective makes possible to model a pseudo low-thrust control within a discrete-time framework.

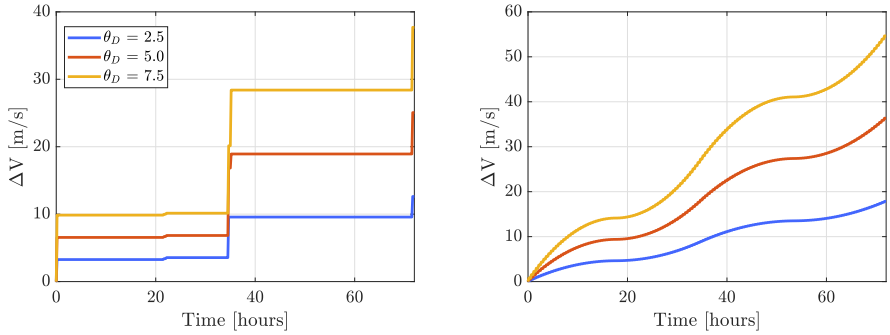

(a) Linear fuel objective. **(b)** Quadratic fuel objective.

Figure 4.9: Δv for the two cost functions considered.

The resulting trajectories for the quadratic fuel objective case in both absolute and relative conditions are reported in Fig. 4.10, distinguishing the natural and propelled arcs in each representation.

From these results we can deduce that, if the objective is to reduce the absolute navigation error below a certain value, there are multiple possibilities. First, for a target with a fixed relative distance, Eq. 2.12 can be used to select the value for θ. If that is not the case, it is favourable to have targets closer or that naturally reduces the range during the time of interest.

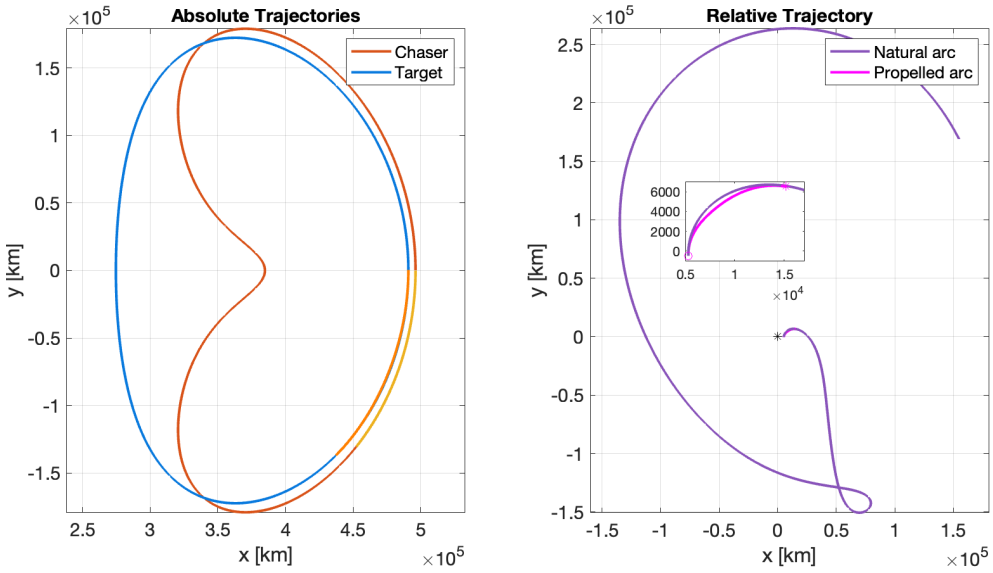

Figure 4.10: Absolute (left) and relative (right) trajectories resulting from the optimisation with the quadratic fuel objective for the Lyapunov to DRO scenario with $\theta_D = 5\,\text{deg}$.

4.2.3.2 Halo to DRO Navigation

In the previous scenario, a high relative distance was selected with the sole purpose of proving the validity of the GNC architecture. However, it is always desirable to work with smaller values because, given the angle θ, the Δv required to perturb the natural trajectory grows as function of the range between the spacecraft. In the following simulation the chaser has been placed on a L2 Halo orbit, whereas the location of the target has remained unchanged. Thus, the resulting relative motion will include both in-plane and out-of-plane components. Additionally, the initial positions have been selected to generate a relative motion whose range gradually reduces in time (contrary to the previous configuration). The optimal manoeuvre plan was computed assuming a high-thrust engine, thus the linear fuel cost function, and a desired minimum observability angle of 1°. The time span of this analysis is reduced to 8 h.

Figure 4.11a shows that despite a small observability angle was selected, the navigation filter is capable of improving the initial error down to 1% of the range.

The resulting absolute and relative trajectories are presented in Fig. 4.12, highlighting the natural and propelled evolutions.

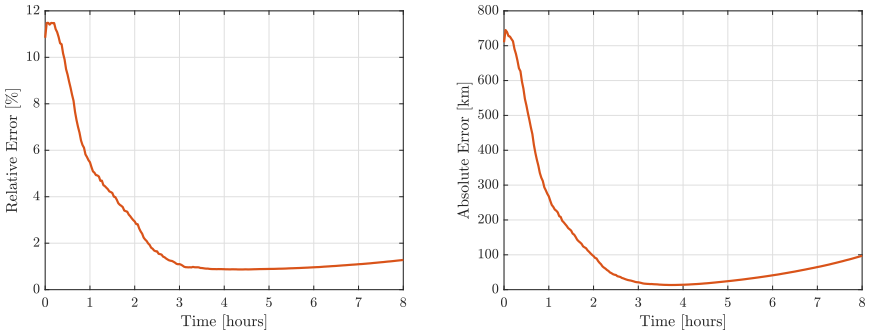

(a) Relative position error. **(b)** Absolute position error.

Figure 4.11: Relative and absolute position errors for the Halo to DRO scenario.

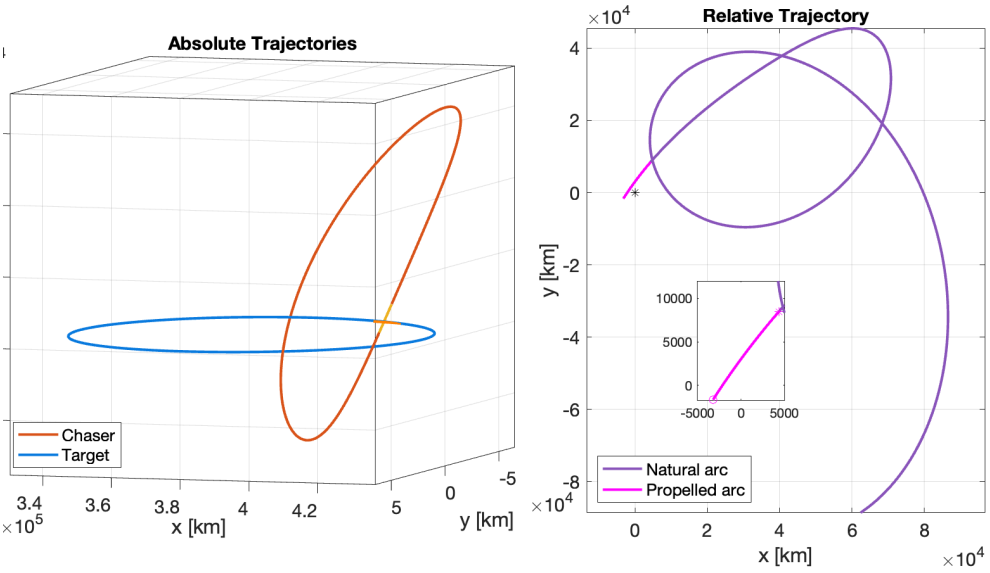

Figure 4.12: Absolute (left) and relative (right) trajectories resulting from the optimisation for the Halo to DRO scenario.

As visible in Fig. 4.13a the distance steadily decreases throughout the first half of the simulation; thus from an absolute point of view, the position error drops from more than 700 km to just 20 km. Then, as the satellites move away from each other, the absolute error deteriorates accordingly. Interestingly, in this scenario the filter convergence is almost exclusively due to the range reduction: enforcing higher observability angles yields only minor navigation improvements, which are not worth the extra-fuel consumption. Therefore, a careful selection of the natural relative motion can provide potential trajectories that enhance the filter observability with minimum fuel consumption. Indeed, thanks to both the smaller distance and lower observability angle, the total Δv required is only of $4.58\,\mathrm{m\,s^{-1}}$, less than half the smallest value of the previous case.

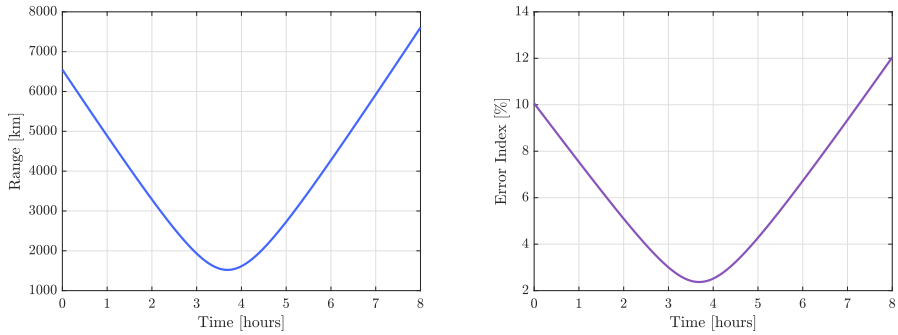

(a) Range evolution. **(b)** Linear model error index.

Figure 4.13: Evolution of the range and the approximation error index (i. e. ratio between chaser-target and target-Moon distance) in the Halo to DRO scenario.

Notice that towards the end of the simulation, Fig. 4.11a displays an increment of the relative error, contrary to Fig. 4.7a and 4.7b which are characterised only by constant or decreasing sections. This issue is associated with the quality of the linear approximation adopted to predict the relative dynamics. Indeed, the linearisation of the original nonlinear equations of motion was carried out assuming the range between the satellites to be much smaller than the target-Moon distance. The ratio between these two values, named here *error index*, can be used as a reference for the quality of the linear approximation and has been reported in Fig. 4.13b. By comparing these results with the relative position error, the final performance reduction can be correlated with the linear approximation deterioration. As the error index gets worse, the model accuracy decreases and the relative error grow rate increases (i.e., the faster increment at the end is caused by a worse relative model quality). As a reference, the previous simulation scenario had an error index of 2.5%. Unfortunately, this parameter drastically reduces the potential orbital combinations that can be

exploited with the proposed architecture. For example, when selecting orbits belonging to different non-Keplerian families, there are only few points where the error index is small enough to guarantee the convergence of the navigation filter. The results, also backed-up by a series of numerical simulations, prove that an error index smaller than 10% is enough to provide an improvement of the initial error, whereas a value below 5% is recommended to guarantee that the relative error remains within a bounded interval.

4.3 Formation Flying reconfiguration manoeuvres

As explained at the beginning of this chapter, the other relevant mission case where the autonomous GNC capabilities are interestingly forsaken is a formation flying scenario. In the environment we are dealing with, the multibody gravitational regime provides both an additional complexity and a resource to exploit some interesting dynamical characteristics.

In particular, the goal of this second scenario is to present a strategy to generate natural relative trajectories for formation flying mission to cooperate with the lunar Gateway, exploiting the peculiar features of quasi-periodic invariant tori, as discussed in section 4.3.1. Such natural evolution is also supported by a GNC strategy used to perform reconfiguration manoeuvres among different trajectories of the torus. To perform this rephasing, an MPC is employed, as deeply discussed in section 4.3.2. The results of this approach are presented in section 4.3.3, comparing a formulation with only platform thrusting limitations with another one which includes also collision avoidance capabilities. To prove the great performance of this approach with respect also to robustness against unmodelled dynamics, the results obtained within a high-fidelity dynamical model are collected and commented in section 4.3.3.3, introducing some discrepancies between the on-board and real-world models. Finally, section 4.3.4 presents the efforts put in place to introduce also the Navigation task to the whole loop, trying to apply the insights obtained by the analyses in the rendezvous scenario to include the BO guidance in the MPC.

4.3.1 Formation Design

This section introduces the models and methods for the design of the reconfigurable formation. The study considers a leader-follower formation type in the Earth-Moon binary system, taking the Lunar Gateway and the Orion capsule as spacecraft. To build the formation, the approximated model of the CR3BP (see Eq. 2.3) is adopted, such that periodic and quasi-periodic natural motion can be easily identified. Then, it is assumed that the main spacecraft (Gateway) is located on a periodic orbit, and that the chaser flies in formation around it, on a quasi-periodic natural motion described in the CR3BP as Quasi Periodic Torus (QPT) (Section 4.3.1.1).

The design of trajectories to host the formation is based on the CR3BP, as it provides an autonomous dynamics system, not explicitly dependent on time. This allows one to easily define continuous families of periodic and quasi periodic natural motion. When switching to more accurate models, such trajectories are no more natural, but the deviations will be small enough to require a limited station-keeping effort.

4.3.1.1 Quasi Periodic Tori

Quasi periodic invariant tori are closed surfaces that describe the bounded subspace covered by specific quasi periodic and non resonant trajectories, i.e., a quasi periodic trajectory in the CR3BP would exactly describe a QPT if propagated for an infinite time. Differently from their periodic counterpart, they are associated with two angles (θ) and relative frequencies (ω):

- Longitude (θ_0, ω_0): direction of the main motion which follows the reference trajectory
- Phase (θ_1, ω_1): secondary direction, describing the *winding* motion around the main trajectory

The ratio of the two frequencies is an irrational number, causing the trajectory to never close on itself. Also, a useful parameter to characterise the torus is the *rotation number*, which measures the change in the phase angle at every orbital turn (i.e., at 2π variation of the longitude). The development of QPT families follows the typical *Initialisation-Correction-Continuation* scheme adopted for generating periodic orbital families in the CR3BP [78, 79]. The family is initialised by creating a grid of states around the reference periodic trajectory, at a specified time, leveraging the center manifold of the latter. Such grid is then corrected by enforcing the following equations:

$$D^{-1}R(\rho)D\mathbf{X}_f - \mathbf{X}_i = \mathbf{0} \tag{4.31}$$

$$< \mathbf{X}_i - \tilde{\mathbf{X}}_i, \frac{\partial \tilde{\mathbf{X}}_i}{\partial \theta_0} > = 0 \tag{4.32}$$

$$< \mathbf{X}_i, \frac{\partial \tilde{\mathbf{X}}_i}{\partial \theta_1} > = 0 \tag{4.33}$$

$$\tau - \tau_p = 0 \tag{4.34}$$

which respectively ensure that the final states propagated for one orbital period belong to the same *stroboscopic map* (Eq. 4.31), which is the locus of states with same longitude and variable phase; that such map is fixed in space, avoiding drifts along the two dimensions of the torus (Eq.s 4.32 and 4.33); that the overall torus' period matches the one of the periodic orbit, or, equivalently, that the longitude frequency does not change (Eq. 4.34). Notice that the last constraint is included to limit the search of QPT families to the ones suitable

for formation flight, as having the same longitude frequency as the reference periodic orbit ensures the absence of secular drifts between the agents of the formation. In Eq. 4.31 D is the Direct Fourier Transform operator expressed as a matrix, while $R(\rho)$ is the diagonal rotation matrix for the Fourier coefficients. Finally, the continuation is typically performed through perturbations of the previous solution along tangent directions of the family. More details about the development of QPT families can be found in [80, 81, 82, 83].

The selected QPT to locate the follower spacecraft (the Orion capsule) is depicted in Figure 4.14 around the NRHO, and in a relative-state form with respect to the Gateway. The operative torus is characterised by an excursion of

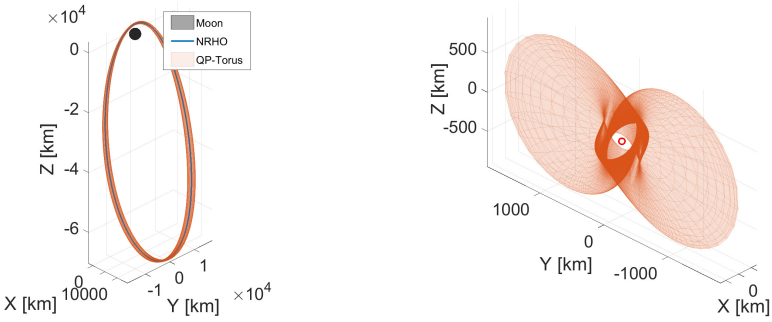

(a) Torus view from Moon-centered frame

(b) Torus view from Gateway-centered frame

Figure 4.14: Torus around the Gateway NRHO.

the relative distance between the formation's agents from 102 km to 1824 km. The orbital period is the same of the reference NRHO, coherently with the constraint of Eq. 4.34, and has a rotation number of 46.9° per orbit.

To reconfigure the formation, transfer arcs are foreseen for the follower spacecraft, that depart from the torus surface and arrives at the same surface on a different location. The final point is defined by the target phase angle, while the longitude angle evolves linearly in time as both spacecraft move along their respective orbits. Notice that, to avoid relative drifts during the transfer, it must be ensured that the transfer time matches the natural longitude drift of the leader spacecraft along the reference orbit, i.e.:

$$ToF = \frac{\theta_0}{\omega_0} \tag{4.35}$$

where ToF is the time of flight required to complete the transfer.

Given the known (and forecasted also in this scenario as it will be clearer) issues deriving from the periselene of the NRHO, the longitude associated to

the aposelene of the NRHO is set to a value of θ_0 =0°. In such a way, the periselene is present at θ_0 =180°.

In the following sections we will refer to mainly three different trajectories:

- Reference Trajectory: the trajectory of the LOP-G, which act as reference for the QPT.
- Target Trajectory: the final trajectory that we want to reach, i. e. the goal of our rephasing manoeuvre.
- Chaser (or Follower) Trajectory: the trajectory that the studied spacecraft is following.

It is important thus to recall that the term *Target* in the following does not point to the LOP-G, but to the final relative trajectory on the QPT that the chaser is *targetting* for the transfer.

4.3.2 On-Board Controller Design

Previous works [83] demonstrated the relatively low cost of impulsive reconfiguration manoeuvres leveraging phase targeting on the toroidal surface, thanks also to the symmetry properties of QPT. Figure 4.15 depicts optimal impulsive reconfiguration costs to ensure a 180° phase shift, given a *ToF* of 48 h (compatibly with manned operations for approaching the Lunar Gateway), on the operative torus just described. Limited costs are observed across the whole

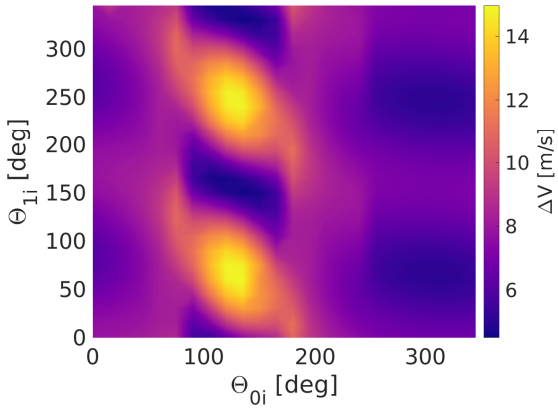

Figure 4.15: Cost map for a 180° phase shift as function of initial phase and longitude angles. Time of flight of 48 h.

torus, with peaks below 15 m s^{-1}. Nevertheless, such optimal transfers rely on ground-based off-line optimisation and planning, and require systematic refinements to accommodate the differences between the CR3BP model (on

which the maps are based) and the actual real-world dynamics of the formation. Frequent contacts between ground and the formation may result in more complex and expensive operations (especially if formations of several agents are employed), therefore it is desirable to have a (computationally) *light* and *effective* on-board control model, which allows a follower spacecraft to perform a full reconfiguration transfer with minimal data exchange with ground.

The present section describes a closed loop scheme for formation reconfiguration manoeuvres, with emphasis on the actual controller design, based on an MPC strategy, showing its strengths and weaknesses. Furthermore, a *classical* and an *adaptive* weights design is proposed, to highlight the benefits from the adaptive approach to the studied scenario.

4.3.2.1 Closed loop scheme

The implemented loop consists of a main block comprising the *Guidance* and the *Control* (G&C), an *Inputs* block which includes all the parameters needed by the G&C, and a *Plant* describing the dynamics of the spacecraft. Figure 4.16 depicts the three blocks, hereafter described in detail.

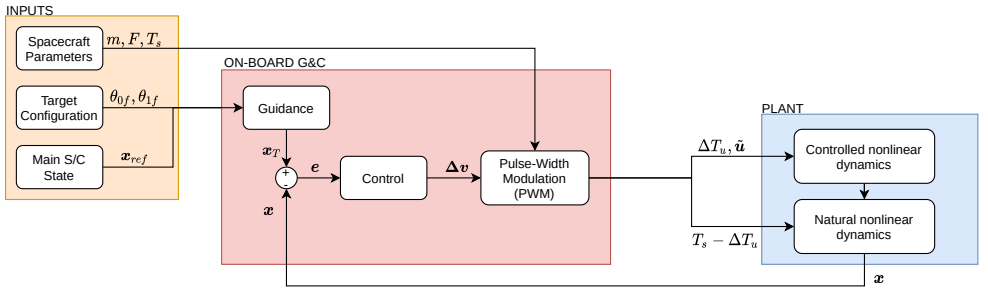

Figure 4.16: Closed loop scheme

Inputs The inputs block collects the full set of parameter on which the G&C loop is based. First, the platform technical characteristics are required to provide the true control action. Some assumptions are made within this study:

- Manoeuvres are small enough not to cause a relevant variation in the wet mass of the spacecraft
- Engines are able to provide a *fixed* thrust value
- A *discrete* control system is employed

Such assumptions allow one to initialise fixed values of mass m and thrust F for the whole transfer time. In particular, a mass of 25 855 kg, corresponding to the full wet mass of the spacecraft, is considered. Also, limited thrust

capabilities are planned for the analysed scenario: it is assumed that only auxiliary thrusters are available for the manoeuvres, and that only half of them (four) are active, delivering a total thrust of $4 \times 490\,\mathrm{N}$ [84]. The combination of high mass and low thrust provides an overall acceleration of $0.076\,\mathrm{m\,s^{-2}}$, and represents a worst-case scenario, to guarantee the effectiveness of the developed control scheme in any spacecraft condition. Finally, a sampling time of $T_s = 600\,\mathrm{s}$ is here set for the update of the discrete control system. This value is derived from tests at various frequencies, to minimise the effort of the control system, while ensuring the capability of reaching the target state. Table 4.3 summarises the platform parameters used for the transfer.

Table 4.3: Spacecraft parameters

Quantity	Value
Mass [kg]	25855
Thrust [N]	4×490
Sampling Time [s]	600
Acceleration [$\mathrm{m\,s^{-2}}$]	0.076

Then, it is required to provide the information needed to reconstruct the time-varying target state on the torus. To avoid the computational burden deriving from numerical propagation, the torus surface and its angular parameters are leveraged to define the motion of the target state over time; this corresponds to a specific quasi-periodic orbit associated with the target phase value (θ_{1f}), hence a single parameter is needed from the guidance. Notice that to identify a specific state along the target trajectory, the longitude angle would be also needed; however, the guidance works on the local stroboscopic map at each time step (as will be explained in the next paragraphs), thus imposing the same longitude as the one of the spacecraft itself.

Finally, the full state of the leader spacecraft ($\mathbf{x}_{ref}$) is needed as well. Indeed, the parametrisation of the torus is done in the context of the CR3BP, and its direct exploitation in a more realistic dynamics scenario would lead to a drift between leader and follower spacecraft of the formation. To work around the problem, the parametrisation is performed to the *relative* torus (where the states are expressed relative to the leader spacecraft), then the true state of the leader is added. This strategy anchors the torus' states around the leader regardless of the real dynamics, although it demands an a-priori knowledge of the leader state evolution, which shall be provided to the follower spacecraft.

On-Board G&C The G&C block is mainly composed of three sub-blocks:

- A *guidance* sub-block

- A *control* sub-block
- A *pulse-width modulation* sub-block

The *guidance* block takes the phase of the desired final trajectory as input, and provides the target trajectory to be tracked during the transfer. To always ensure the maintenance of the formation, regardless of the controller architecture, the target point shall always belong to the same stroboscopic map of the follower spacecraft. In this way, the transfer may take variable time, and yet prevent relative drifts between spacecraft. For this reason, the target point can be uniquely identified along the target trajectory (at phase θ_{1f}) by setting the longitude as

$$\theta_{0f} = \theta_{0i}(0) + \omega_0 t \tag{4.36}$$

with θ_{0i} being the longitude of follower and leader spacecraft at the beginning of the transfer. Given the two angles, the target state can be extracted through a proper parametrisation of the toroidal surface. In the present work, the torus is parametrised using 2D cubic splines, from a pre-defined grid of phase and longitude values. The resulting interpolating function, $\mathbf{s}(\theta_0, \theta_1)$, maps the $\mathbb{R}^2$ space of the torus' angular variables to the $\mathbb{R}^6$ state space in the CR3BP rotating frame, and relatively to the leader spacecraft. The angles defining the grid do not follow the natural evolution of trajectories on the torus. For this reason, the correct reconstruction of the target phase over time can be attained by including the winding frequency of the torus, i.e.:

$$\theta_{1f}(t) = \theta_{1f}(0) + \omega_1 t \tag{4.37}$$

with $\theta_{1f}(0)$ being the initial target phase value. Considering the real state of the leader spacecraft , the guidance block returns the final state to be targeted by the controller as:

$$\mathbf{x}_T(t) = \mathbf{x}_{ref}(t) + \mathbf{s}(\theta_{0i}(0) + \omega_0 t, \theta_{1f}(0) + \omega_1 t) \tag{4.38}$$

The *controller* block defines the law that computes the needed control action from the current error (the difference between the target state and the current state). Since the target state is not a constant quantity, the controller must solve a *reference tracking problem* [56, 85, 86]. In the present work, a *Model Predictive Control* scheme is employed (the details of the design are explained in Section 4.3.2.2). It is here important to stress that the output control action is an impulsive $\mathbf{\Delta v}$ with a variable magnitude, which cannot be provided by the spacecraft engines in the current form.

In this regard, the *pulse-width modulation* block is implemented to translate the variable input into a fixed value, which matches the engine characteristics (Table 4.3). At every sampled time the controller returns the required control

in the form of an impulsive $\mathbf{\Delta v}$. The pulse-width modulation translates the impulsive value into an equivalent *finite-time* manoeuvre by providing the correct thrust time according to the achievable acceleration of the spacecraft, namely:

$$\Delta T_u = \frac{\Delta v}{\tilde{u}} \tag{4.39}$$

where $\tilde{u}$ is the fixed acceleration of the platform. Consequently, at each interval between consecutive sampled times (from t_0 to $t_0 + T_s$), the spacecraft will perform a powered branch first (from $t_0 + \Delta T_u$), then a free drift through natural dynamics until the next time sample (from $t_0 + \Delta T_u$ to $t_0 + T_s$).

Plant The *plant* block describes the ground-truth evolution of the chaser spacecraft state in the binary system. The dynamics propagation is split in two sub-blocks to take into account the alternate powered branches and coasting branches at each sampling time. In the present work, two dynamics models are employed:

- CR3BP
- High-Fidelity (ephemerides with perturbations)

The CR3BP is used to simulate a perfect accuracy of the on-board model with respect to the real dynamics. This allows a direct evaluation and comparison of the controller performance with respect to the optimised impulsive transfers (Fig. 4.15), to address the feasibility of the proposed architecture. Then, high-fidelity dynamics (with true positions of the attractors, and with perturbation from Sun gravity and Solar radiation) is taken into account, to verify the robustness of the scheme against dynamics model errors.

4.3.2.2 MPC Formulation

Given the greater flexibility of the *Receding Horizon* approach for the MPC, this scheme has been selected for the controller design of this scenario, also due to the fact that no particular constraints are requested in a formation flying reconfiguration regarding the ToF, differently from the rendezvous one.

Objective and Constraints The nonlinear formulation of the reference tracking optimal control problem (with discrete quantities) reads:

$$\min_{\mathbf{\Delta x}_k, \mathbf{\Delta u}_k} \sum_{k=0}^{n_p-1} \left[\mathbf{\Delta x}_k^\top \mathcal{Q}_k \mathbf{\Delta x}_k + \mathbf{\Delta u}_k^\top \mathcal{R}_k \mathbf{\Delta u}_k \right] + \mathbf{\Delta x}_{n_p}^\top \mathcal{Q}_{n_p} \mathbf{\Delta x}_{n_p} \tag{4.40a}$$

$$s.t. \quad \mathbf{\Delta \dot{x}}_k = \mathbf{f}(\mathbf{\Delta x}_k) + \mathbf{g}(\mathbf{\Delta u}_k), \quad \forall k \tag{4.40b}$$

$$\mathbf{h}_k(\mathbf{\Delta x}_k, \mathbf{\Delta u}_k) = 0, \quad \forall k \tag{4.40c}$$

$$\mathbf{c}_k(\mathbf{\Delta x}_k, \mathbf{\Delta u}_k) < 0, \quad \forall k \tag{4.40d}$$

Equation 4.40a is the cost function to be optimised, in the *Bolza Problem* form [87]. Here, $\boldsymbol{\Delta}\mathbf{x}$ and $\boldsymbol{\Delta}\mathbf{u}$ are the relative state and relative control between the spacecraft $(\mathbf{x}, \mathbf{u})$ and the target point $(\mathbf{x}_T, \mathbf{u}_T)$ respectively, while $\mathcal{Q}$ and $\mathcal{R}$ are the corresponding weight matrices.

Equation 4.40b describes the on-board implemented dynamics, where $\mathbf{f}(\boldsymbol{\Delta}\mathbf{x}_k)$ and $\mathbf{g}(\boldsymbol{\Delta}\mathbf{u}_k)$ are the collection of nonlinear terms, function of the state and of the input respectively. Equations 4.40c and 4.40d are the set of equality and inequality constraints respectively.

Note that, according to the problem analysed in this paper, the target point is defined for each time step as Eq. 4.38, and the corresponding control action is null ($\mathbf{u}_T = 0$), being the target a natural trajectory in the dynamics model of the controller (CR3BP). Also, the control actions within the MPC are modelled as impulsive manoeuvres, therefore they can be expressed as

$$\boldsymbol{\Delta}\mathbf{u}_k = \boldsymbol{\Delta}\mathbf{v}_k \delta(t_k) \tag{4.41}$$

where $\delta(t_k)$ is the *Kronecker's delta*.

Problem 4.40 could be directly solved within a MPC scheme by using a Nonlinear Programming methodology; however, this typically leads to high computational burdens and makes the overall process less prone to on-board implementation. To make the problem more tractable, modifications are introduced to recast the problem in a Quadratic Programming form. The same approach followed in the previous scenario to define the discretised dynamics is exploited also here, recalling that given the receding horizon formalism, in this scenario the window is much shorter and with a fixed number of n_p predicted points. Given the shorter duration of the window, a first order approximation of the STM can be used.

First, the nonlinear dynamics of Eq. 4.40b is recast as a sequence of local linearisations, to avoid numerical integration of the state and of the STM. At each time step, the linearised dynamics reads:

$$\boldsymbol{\Delta}\mathbf{x}_{k+1} = e^{A_k(t_{k+1}-t_k)}\boldsymbol{\Delta}\mathbf{x}_k + \int_{t_k}^{t_{k+1}} e^{A_k(t_{k+1}-\tau)} B_k \boldsymbol{\Delta}\mathbf{u}_k \, d\tau \tag{4.42a}$$

$$A_k = \frac{\partial \mathbf{f}(\boldsymbol{\Delta}\mathbf{x}_k)}{\partial \boldsymbol{\Delta}\mathbf{x}_k} \tag{4.42b}$$

$$B_k = \frac{\partial \mathbf{g}(\boldsymbol{\Delta}\mathbf{u}_k)}{\partial \boldsymbol{\Delta}\mathbf{u}_k} \tag{4.42c}$$

Approximating the exponential terms as $I+A_k(t_{k+1}-t_k)$, and recalling Eq. 4.41, the expression 4.42a becomes

$$\boldsymbol{\Delta}\mathbf{x}_{k+1} = A_k^{k+1}\boldsymbol{\Delta}\mathbf{x}_k + B_k^{k+1}\boldsymbol{\Delta}\mathbf{v}_k \tag{4.43a}$$

$$A_k^{k+1} = I + A_k(t_{k+1} - t_k) \tag{4.43b}$$

$$B_k^{k+1} = A_k^{k+1}B_k \tag{4.43c}$$

Again, the generic (k+j)th state is expressed as function of the initial state $\boldsymbol{\Delta}\mathbf{x}_k$ and the set of control actions from initial node to the (k+j-1)th node

$$\begin{aligned}
\boldsymbol{\Delta}\mathbf{x}_{k+j} &= A_{k+j-1}^{k+j}\boldsymbol{\Delta}\mathbf{x}_{k+j-1} + B_{k+j-1}^{k+j}\boldsymbol{\Delta}\mathbf{v}_{k+j-1} \\
&= A_{k+j-1}^{k+j}\left(A_{k+j-2}^{k+j-1}\boldsymbol{\Delta}\mathbf{x}_{k+j-2} + B_{k+j-2}^{k+j-1}\boldsymbol{\Delta}\mathbf{v}_{k+j-2}\right) + B_{k+j-1}^{k+j}\boldsymbol{\Delta}\mathbf{v}_{k+j-1} \\
&\ \ \ldots \\
&= \prod_{i=j-1}^{0} A_{k+i}^{k+i+1}\boldsymbol{\Delta}\mathbf{x}_k + \\
&+ \left[\prod_{i=j-1}^{1} A_{k+i}^{k+i+1}B_k^{k+1},\ \prod_{i=j-1}^{2} A_{k+i}^{k+i+1}B_{k+1}^{k+2},\ \ \ldots,\ \ B_{k+j-1}^{k+j}\right]\begin{bmatrix}\boldsymbol{\Delta}\mathbf{v}_k \\ \vdots \\ \boldsymbol{\Delta}\mathbf{v}_{k+j-1}\end{bmatrix}
\end{aligned} \tag{4.44}$$

If the expression 4.44 is computed for all states of the prediction window (from $k+1$ to $k+n_p$) the full stack of the states $\mathbb{X}$ reads

$$\mathbb{X} = \mathbb{A}_k\boldsymbol{\Delta}\mathbf{x}_k + \mathbb{B}_k\mathbb{U} \tag{4.45}$$

with

$$\mathbb{X} = \left[\boldsymbol{\Delta}\mathbf{x}_{k+1}, \boldsymbol{\Delta}\mathbf{x}_{k+2}, \ldots, \boldsymbol{\Delta}\mathbf{x}_{k+n_p}\right]^\top \tag{4.46}$$

$$\mathbb{U} = \left[\boldsymbol{\Delta}\mathbf{v}_k, \boldsymbol{\Delta}\mathbf{v}_{k+1}, \ldots, \boldsymbol{\Delta}\mathbf{v}_{k+n_p-1}\right]^\top \tag{4.47}$$

$$\mathbb{A}_k = \begin{bmatrix} A_k^{k+1} \\ A_{k+1}^{k+2}A_k^{k+1} \\ \prod_{i=2}^{0} A_{k+i}^{k+i+1} \\ \cdots \\ \prod_{i=n_p-1}^{0} A_{k+i}^{k+i+1} \end{bmatrix} \tag{4.48}$$

$$\mathbb{B}_k = \begin{bmatrix} B_k^{k+1} & 0 & \ldots & 0 \\ A_{k+1}^{k+2}B_k^{k+1} & B_{k+1}^{k+2} & \ldots & 0 \\ \vdots & \vdots & & \vdots \\ \left(\prod_{n_p-1}^{1} A_{k+i}^{k+i+1}\right)B_k^{k+1} & \left(\prod_{n_p-1}^{2} A_{k+i}^{k+i+1}\right)B_{k+1}^{k+2} & \ldots & B_{k+n_p-1}^{k+n_p} \end{bmatrix} \tag{4.49}$$

Similarly, the cost function 4.40a can be expressed through the stack of states and inputs as

$$\min_{\mathbb{X},\mathbb{U}} = \frac{1}{2}\Big(\mathbb{X}^\top \hat{\mathcal{Q}}\mathbb{X} + \mathbb{U}^\top \hat{\mathcal{R}}\mathbb{U}\Big) \tag{4.50}$$

$$\hat{\mathcal{Q}} = \begin{bmatrix} \mathcal{Q} & 0_{6\times6} & \dots & 0_{6\times6} \\ 0_{6\times6} & \mathcal{Q} & \dots & 0_{6\times6} \\ \vdots & & \ddots & \\ 0_{6\times6} & 0_{6\times6} & \dots & \mathcal{Q} \end{bmatrix} \tag{4.51}$$

$$\hat{\mathcal{R}} = \begin{bmatrix} \mathcal{R} & 0_{3\times3} & \dots & 0_{3\times3} \\ 0_{3\times3} & \mathcal{R} & \dots & 0_{3\times3} \\ \vdots & & \ddots & \\ 0_{3\times3} & 0_{3\times3} & \dots & \mathcal{R} \end{bmatrix} \tag{4.52}$$

where all the weights have been set equal for all nodes ($\mathcal{Q}_k = \mathcal{Q}_{n_p} = \mathcal{Q}$, $\mathcal{R}_k = \mathcal{R}$).

After substituting the stack of states from 4.45 in the cost 4.50, a quadratic form as function of the control stack $\mathbb{U}$ is obtained, and reads[1]

$$\min_{\mathbb{U}} \frac{1}{2}\mathbb{U}^\top \mathbb{H}_k \mathbb{U} + \mathbf{l}_k^\top \mathbb{U} \tag{4.53}$$

with

$$\mathbb{H}_k = \mathbb{B}_k^\top \hat{\mathcal{Q}}\mathbb{B}_k + \hat{\mathcal{R}} \tag{4.54}$$

$$\mathbf{l}_k^\top = \Delta\mathbf{x}_k^\top \mathbb{A}_k^\top \hat{\mathcal{Q}}\mathbb{B}_k. \tag{4.55}$$

Regarding the constraints (Eq.s 4.40c and 4.40d), a linearisation is required to fully define the QP Problem. In the present study, no equality constraint is included, while two inequality constraints are considered:

- Maximum thrust
- Leader-Follower collision avoidance

The *maximum thrust* constraints ensures that every $\mathbf{\Delta v}_k$ does not exceed the value that can be provided by the fixed thrust within a full sample time T_s, namely:

$$\|\mathbf{\Delta v}_{k+i}\|_2 < \tilde{u}T_s \ , \quad i \in 0:j \tag{4.56}$$

The constraint is nonlinear as it involves the *2-norm* of a vector. Hence, it needs first to be linearised, according to the formulation of the QP Problem.

[1]The additional, constant term $\frac{1}{2}\Delta\mathbf{x}_k^\top \mathbb{A}_k^\top \hat{\mathcal{Q}}\mathbb{A}_k\Delta\mathbf{x}_k$ would be present in the final cost expression; however, it does not affect the minimisation process, hence it can be omitted.

In particular, a simplification is introduced by imposing that the ∞-*norm* of every $\boldsymbol{\Delta}\mathbf{v}_k$ in the prediction window, i. e. every component of the control stack, shall be lower than the right-hand side of Eq. 4.56 divided by the square root of three, namely:

$$\|\mathbb{U}\|_\infty < \frac{\tilde{u}T_s}{\sqrt{3}} \tag{4.57}$$

Notice that this formulation makes the constraint anisotropic. In fact, any control action aligned with one of the Cartesian directions is required to be less than the actual maximum control that the spacecraft can provide; nevertheless, when the control vector is aligned with the trisectrix of any octant (defined by the three Cartesian axes), it is ensured that its *2-norm* stays below the max value:

$$\|\boldsymbol{\Delta}\mathbf{v}_{k+i}\| = \sqrt{\Delta v_x^2 + \Delta v_y^2 + \Delta v_z^2} < \sqrt{\left(\frac{\tilde{u}T_s}{\sqrt{3}}\right)^2 + \left(\frac{\tilde{u}T_s}{\sqrt{3}}\right)^2 + \left(\frac{\tilde{u}T_s}{\sqrt{3}}\right)^2} = \tilde{u}T_s \tag{4.58}$$

The *collision avoidance* constraints imposes a minimum distance between the leader and the follower of the formation for the whole transfer arc. In general, the distance constraint is expressed in nonlinear form as follows:

$$\|C\boldsymbol{\Delta}\mathbf{x}_{k+i}\|_2^2 = \boldsymbol{\Delta}\mathbf{x}_{k+i}^\top C^\top C \boldsymbol{\Delta}\mathbf{x}_{k+i} > R_{KOZ}^2 \,, \quad i \in 0:j \tag{4.59}$$

where $C := [I_{3\times 3} \quad 0_{3\times 3}]^\top$, while R_{KOZ} is the radius of the Keep-Out Zone (KOZ) sphere. To embed the constraint in the QP formulation, a linearisation is again needed. In this regard, the paper exploits the methodology proposed by Morgan et. al. [88]. The KOZ sphere is approximated into a plane tangent to it, and normal to the $\Delta\mathbf{x}_{k+i}$ vector. In such a way, the constraint can be expressed in a convex form as per Eq. 4.60, leveraging the known initial value of the prediction window, $\boldsymbol{\Delta}\mathbf{x}_k$.

$$-\boldsymbol{\Delta}\mathbf{x}_k^\top C^\top C \boldsymbol{\Delta}\mathbf{x}_{k+i} < -R_{KOZ} \|C\boldsymbol{\Delta}\mathbf{x}_k\|_2 \tag{4.60}$$

Note that, to express the constraint as an upper boundary inequality, the sign of both sides of the equation has been inverted.

Equation 4.60 is applied to each step of the time window, hence the constraint can be formulated as function of the control stack, leading to the following expressions:

$$A_{CAM}\mathbb{U} < \mathbf{b}_{CAM} \tag{4.61}$$

with

$$A_{CAM} = -I_{n_p \times n_p} \otimes \boldsymbol{\Delta}\mathbf{x}_k^\top C^\top C \mathbb{B}_k \tag{4.62}$$

$$\mathbf{b}_{CAM} = -R_{KOZ} \|C\boldsymbol{\Delta}\mathbf{x}_k\|_2 \mathbf{1}_{n_p \times 1} + I_{n_p \times n_p} \otimes \boldsymbol{\Delta}\mathbf{x}_k^\top C^\top C \mathbb{A}_k \boldsymbol{\Delta}\mathbf{x}_k \tag{4.63}$$

where the symbol $\otimes$ denotes the *Kronecker product*.

Finally, the complete problem, with quadratic cost function and linear constraints, reads:

$$\begin{aligned} \min_{\mathbb{U}} \quad & \frac{1}{2}\mathbb{U}^\top \mathbb{H}_k \mathbb{U} + \mathbf{l}_k^\top \mathbb{U} \\ \text{s.t.} \quad & \|\mathbb{U}\|_\infty < \frac{\tilde{u} T_s}{\sqrt{3}} \\ & A_{CAM}\mathbb{U} < \mathbf{b}_{CAM} \end{aligned} \tag{4.64}$$

The algorithm that solves Problem 4.64 returns the full stack of optimal control $\mathbb{U}_{opt}$; however, only the first control is applied before a new optimisation is performed.

Weight Tuning The solution of Problem 4.64 is strongly dependent on the selection of weights $\mathcal{Q}$ and $\mathcal{R}$.

The common approach is to search for *Fixed Weights* which ensure the completion of the transfers with the desired performance. In this study, the main objective is the minimisation of costs and the completion of the transfers within a specified maximum ToF of 48 h. The transfers are considered completed when the position error between follower spacecraft and target point falls below 2 km. The weights are obtained through an optimisation process as well. To set up the optimisation, some simplifications are introduced. Considering that state ($\mathcal{Q}$) and control ($\mathcal{R}$) weights act on a cost function to be minimised, we can set $\mathcal{R}$ equal to identity matrix and tune $\mathcal{Q}$ relatively to it without any loss of generality. Furthermore, no coupling between the state terms is considered, therefore $\mathcal{Q}$ is a diagonal matrix. As an additional simplification, all the diagonal terms associated with the position terms of the state are assumed equal, and the same assumption is applied to velocity-related weights as well. As a result, the weight arrays read:

$$\begin{aligned} \mathcal{Q} &= \begin{bmatrix} q_r I_3 & 0_3 \\ 0_3 & q_v I_3 \end{bmatrix} \\ \mathcal{R} &= I_3 \end{aligned} \tag{4.65}$$

where q_r and q_v are the two scalars to be tuned and optimised. Then, the optimisation problem reads

$$\min_{q_r, q_v} \Delta v \quad s.t. \quad \Delta T \leq ToF \tag{4.66}$$

where Δv is here the overall scalar cost of the transfer, and ΔT is the time required to reach the target point within a specified tolerance.

Despite the simplicity of the approach, this strategy suffers from a lack of robustness against deviations in the trajectory, for example due to errors in the

dynamics model. Furthermore, the fixed values may not capture variations in the controller behavior during each transfer, as a consequence of large relative position displacements and changes in speed. For these reasons, this thesis also implements a strategy to modify the weights on-board while performing the transfer, leveraging an adaptation law developed in [89] for a *State Dependent Riccati Equation* controller in the same scenario. This *Adaptive Weights* strategy is designed to require a single initial tuning of some terms, and it provides efficient transfers of the spacecraft anywhere along the quasi-periodic torus. In particular, the position terms q_r of the weight matrix $\mathcal{Q}$ are scaled through a coefficient which is directly related to the spacecraft-target relative state, and to the available time to complete the transfer within the ToF:

$$q_r = \gamma(\Delta r, \Delta \dot{r}, t_k) q_{MAX} \tag{4.67}$$

with q_{MAX} being a user-defined upper limit for the weight, and γ being the adaptation coefficient, explicitly defined as:

$$\gamma = \alpha^{\beta} \tag{4.68}$$

$$\alpha = \left(\frac{\Delta r_T}{\Delta r} \right) \tag{4.69}$$

$$\beta = 1 + \frac{\Delta \dot{r}}{\Delta r}(ToF - t_k) \tag{4.70}$$

Here, Δr and $\Delta \dot{r}$ respectively represent the relative distance and relative radial velocity from spacecraft to target point, Δr_T is the distance threshold which determines the end of the transfer, and t_k is the discrete time instant passed from the beginning of the transfer.

As a result, this scaling law makes the control action smaller and milder at large distance from target and at recently begun transfers, to avoid large initial control actions, while it brings the weight closer to its max value when approaching the target and/or when the time left is short. In addition, the local evaluation of relative radial velocity adapts the coefficient to avoid excessively slow or excessively high approaching speeds. In addition, a reduction step saturation $\Delta\beta$ from consecutive sample points is set to avoid large control cost increments caused by local low approach speed of the target (see again [89] for the complete rationale):

$$\beta = \max \left(\left[1 + \frac{\Delta \dot{r}}{\Delta r}(ToF - t_k) \quad , \quad \beta_0 - \Delta\beta \right] \right) \tag{4.71}$$

where β_0 denotes the β exponent from the previous step. The velocity-related weights (q_v) are instead tuned once and remain constant across the transfer. Figure 4.17 depicts the update scheme of the weights according to the adaptation law. Overall, the initial parameters to be set are: q_{MAX}, q_v, β_0 and $\Delta\beta$.

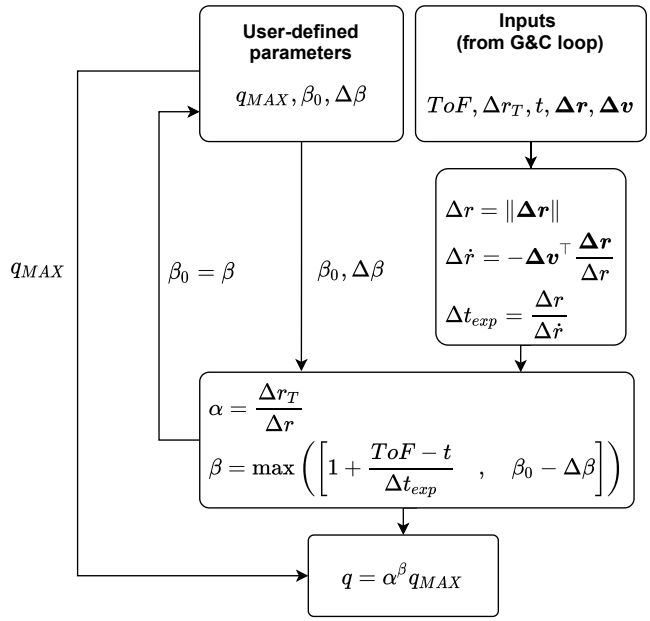

Figure 4.17: Adaptation law scheme.

The present study develops the transfers and maps the costs for both fixed and adaptive weights strategies, highlighting the advantages of the latter technique.

4.3.3 Simulations and Results

This section reports on the performance of the formation reconfiguration transfers with the closed-loop scheme described in Section 4.3.2.

The first part shows a performance comparison between a MPC with *Fixed Weights* and with *Adaptive Weights*. Here, only the maximum thrust constraint is considered in the MPC optimisation process, to decouple the effect of CAM from the intrinsic differences of the weights management. Furthermore, the CR3BP dynamics model is leveraged as both on-board and ground-truth dynamics, to avoid cost variation from model errors.

Then, collision avoidance is included in the controller, to highlight the cost variation and assess the validity of the weights tuning in the presence of large trajectory detours.

As a final part of the study, high-fidelity dynamics are introduced to propagate the spacecraft state, and the robustness of the controller is tested in the presence of model errors.

4.3.3.1 Fixed Weights vs Adaptive Weights

Before proceeding with the analysis, it is important to mention a particular behaviour that characterises the on-board scheme with respect to the offline optimisation of the transfer of Figure 4.15, regardless of how the weights of the cost function are designed. Because of the local-optimising nature of the MPC, the scheme is not able to locate the best points where to manoeuvre, and it will provide a control action at every sampled point for the whole transfer. This leads to unacceptably high costs when the spacecraft is flying across the periselene of the NRHO, as the high speed and low distance from the Moon make most of the manoeuvres very expensive. To work around the problem a limiter in the ToF is here implemented, which always ensures the completion of the transfer before crossing the periselene, for all transfers that foresee a periselene passage within the default ToF of 48 h.

Weights Setup The first step of the analysis of the MPC scheme involves the setup of the *fixed* and of the *adaptive* weights.

The *fixed weights* approach required a dedicated tuning for every transfer, according to optimisation problem 4.66. The output is a map of position- and velocity-related weights as a function of the initial angular coordinates of the transfer along the torus, as depicted (in logarithmic scale) in Figure 4.18. Ranges of approximately $10^0 - 10^3$ are observed across the torus, with peaks

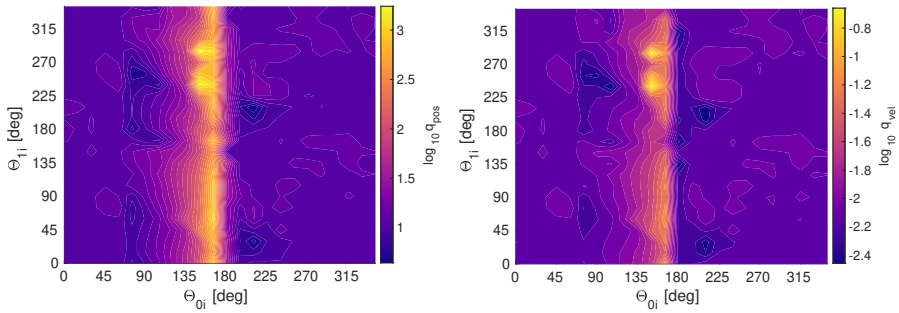

(a) Position weights **(b)** Velocity weights

Figure 4.18: Map of the position and velocity weights for the *fixed weights* MPC (logarithmic scale)

nearby the periselene, and significantly lower values on the rest of the surface. The velocity weights follow the same trend of the position weights, with values scaled down to the $10^{-2.4} - 10^{-0.7}$ range. Their lower values ensure a prompter transfer to achieve the target point within the time limit, but provide a minor control over the relative speed, preventing overshooting issues. In general, negligible to no influence of the initial phase was observed on the weights, and

minor scattered variations can be attributed to the optimisation process and to the tolerances associated with it. It is, however, important to stress how such minor variations do not have macroscopic influence on the costs for the transfer, as it will be shown later in this section.

The *adaptive weights* setup consists of a single tuning process, which is done for the whole transfer map at once. First, the maximum position weight (q_{MAX}) and the velocity weight (q_v) are tuned to ensure transfer times below the limit, and minimise the Δv over the entire torus as much as possible. This is done repeatedly for different values of β_0, to find the initial exponent value which improves performance the most. The previous search is done with a total freedom of the coefficient β to adapt to any value (i.e., without setting the exponent limiter $\Delta\beta$). This inevitably leads to local isolated peaks due to the β overshoot problem described in Section 4.3.2.2. In the final step of the design, the limiter is introduced and modified until the isolated cost peaks disappear. Following the described procedure for the case under study, the parameters reported in Table 4.4 are obtained: Notice that the maximum position weight

Table 4.4: Parameters for the *adaptive weights* MPC.

q_{MAX} [−]	q_v [−]	β_0 [−]	$\Delta\beta$ $[units/h]$
10^6	10^{-2}	2	2

is far higher than the *fixed weights* case. This is explained by the variability of the actual weight along the transfers, which starts from very low values at the beginning when large distance from target are experienced, and needs to be very high at the end in order to complete the transfer before the time limit when the spacecraft is very close to the target point.

Performance Comparison The costs to reconfigure the formation using a *fixed* or *adaptive* weights approach are depicted in Fig. 4.19.

From a direct comparison of the costs from Fig. 4.19a with the optimised impulsive manoeuvres of Fig. 4.15, the *fixed weights* approach shows an overall increment in costs, which however is fairly contained in the most suitable regions for performing the transfers, i. e. nearby the apolune and after passing the periselene. In particular, lower costs of $\sim 13\,\mathrm{m\,s^{-1}}$ are observed in the apolune surroundings, centred at phase values θ_{1i} of 90° and 270°. Here, despite the relative uniformity in the weights maps, a sensitivity is observed with respect to the phase, as the cost of manoeuvres begun at the apolune raise above $20\,\mathrm{m\,s^{-1}}$ when crossing $\theta_{1i} = 0°$ and $\theta_{1i} = 180°$. This is directly related to the larger initial distance from target point at such phases, which leads to a higher control action when the weights are constant values (as it is

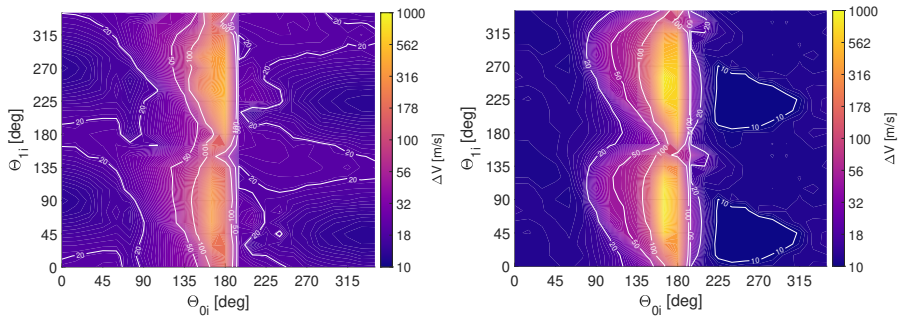

(a) *Fixed weights* approach **(b)** *Adaptive weights* approach

Figure 4.19: Cost maps for the MPC-based formation reconfiguration in the CR3BP. Results in logarithmic scale to highlight differences in the low-cost region.

for the *fixed weights* strategy). Cost rapidly ramps up to above $50\,\mathrm{m\,s^{-1}}$ when approaching the periselene, with peaks at $\sim 450\,\mathrm{m\,s^{-1}}$. Such values suggest how a constantly executed on-board control is not a viable option when close to the Moon, and should be restricted to the rest of the orbit; nevertheless, it is worth stressing that the high cost region occupies a small portion of time (few hours) with respect to the orbital period of 6.5 d, and therefore does not globally hinder the applicability of this control scheme.

The adoption of the *adaptive weights* mostly solves the initial distance-related issues, by providing a milder control action at the beginning of the transfer. This is directly observable in Fig. 4.19b: not only are the cost globally lowered (far from periselene), but also a lower dependence on the phase is here measured. More in detail, the vast majority of transfers costs less than $20\,\mathrm{m\,s^{-1}}$, with very low-costs regions ($< 10\,\mathrm{m\,s^{-1}}$) after the periselene passage, nearly approaching the optimal impulsive manoeuvre cost. On the other hand, costs at the periselene appears to be far higher than the ones displayed by the *fixed weights* MPC, with peaks at $> 800\,\mathrm{m\,s^{-1}}$. This is caused by the direct dependence of the adaptation coefficient to the relative velocity from target, which achieves high values in this orbital region.

Overall, the *adaptive* scheme demonstrated to be more effective than the *fixed weights* approach. Firstly, it allows, from a first design perspective, a faster tuning process which identifies a single group of parameters for all the possible reconfigurations along the quasi periodic torus. Secondly, its capability to reduce the control effort at larger distances from target, while ensuring the success of the transfer in the given time, makes the MPC scheme less sensitive to the follower spacecraft location around the leader, and globally more convenient in terms of cost (with the only exception of the periselene

region, where manoeuvres should be avoided). A result of a specific transfer trajectory for the adaptive weight case, among others, is reported in Fig. 4.22, together with the initial and final trajectory in the relative reference frame.

By comparing the MPC-based transfers with other transfers, such as in [89], it is observed a mild increment of transfer costs, with smaller regions with costs below $10\,\mathrm{m\,s^{-1}}$ and $20\,\mathrm{m\,s^{-1}}$ for the fixed and adaptive weight cases respectively. These narrower areas for the MPC are justified by the finite nature of the optimisation window employed, against the infinite-window formulation of the State Dependent Riccati Equation employed in that analysis. The presence of a final time of the prediction window, shorter than the real final time allowed for the transfer, makes the MPC-computed control generally prompter than the SDRE one. On the other hand, this Δv drawback is compensated by the possibility to deal with constraints that the MPC has, with respect to the SDRE, where the maximum thrust value was not limited.

4.3.3.2 Collision avoidance

Another constraint that can be exploited in the MPC scheme is that of the collision avoidance, very important for spacecraft formation flying. Given the success of the adaptation of weights shown in Section 4.3.3.1, it is of interest to assess the capability of the adaptation law to withstand the CAM and the large deviation that the follower spacecraft may be subjected to when a KOZ is placed around the leader spacecraft. For the problem under study, a KOZ of 100 km has been selected, to enforce CAM to the majority of the transfers, compatibly with the natural distances of the torus from the leader (i. e. avoiding excessive and unjustified deviations). Figure 4.20 depicts the changes in the minimum distance between leader and follower for transfer with and without CAM. One can notice the large involvement of most of the

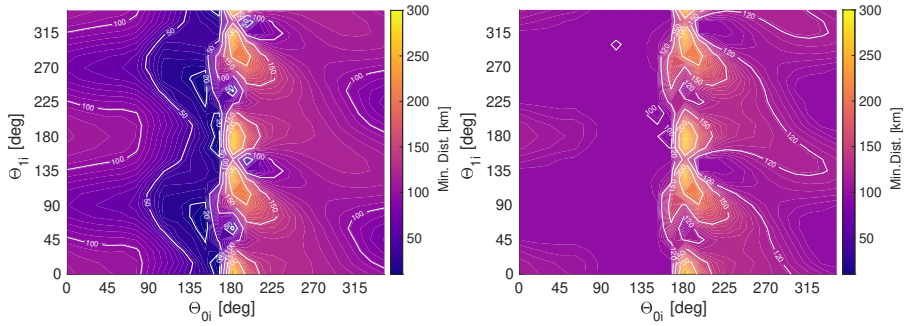

(a) No KOZ **(b)** KOZ at 100 km

Figure 4.20: Minimum distance map between leader and follower spacecraft.

post-apolune regions ($\theta_{0i} \in [0^\circ\ 180^\circ]$), and some zones after the periselene.

Furthermore, the absence of values below 100 km from Fig. 4.20b demonstrates the effectiveness of such constraint within the MPC scheme.

Despite the success in the CAM execution, it is of interest to address whether it makes the completion of the transfers more difficult, and how the costs are affected by it. Regarding the former aspect, the *adaptive weights* MPC demonstrated its capability to complete the transfers in the vast majority of locations along the torus. The only exception is given by the periselene, where the difficulty of the transfer, due to large velocity differences between spacecraft and target point, is exacerbated by the path changes imposed by the CAM. Concerning the cost variation, Fig. 4.21 depicts the increment caused by the introduction of the KOZ. Cost increments are observed in those regions

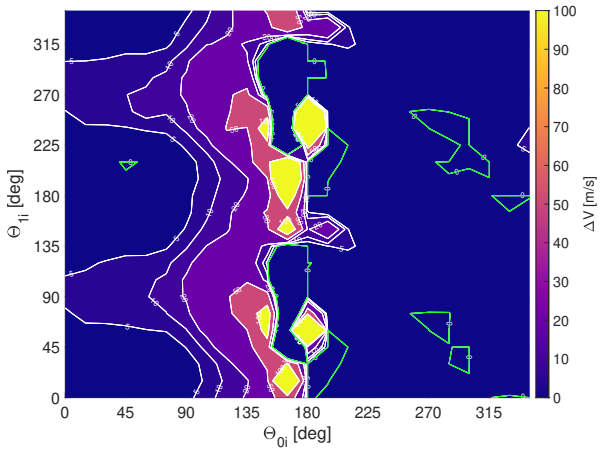

Figure 4.21: Transfers cost increment due to CAM at 100 km.

affected by the presence of CAMs, going from $5\,\mathrm{m\,s^{-1}}$ nearby the apolune, ramping up to $20 - 50\,\mathrm{m\,s^{-1}}$ as the spacecraft approach the periselene region. While the former value indicates a realistic feasibility of such transfers, the latter corresponds to an increment of $75\% - 100\%$ with respect to the no-KOZ costs, thus further enforcing the necessity to avoid transfers when the chaser is so close to the Moon. The two blue regions at the periselene ($\theta_{0i} = 180°$), at the phases of 90° and 180° indicate the aforementioned zones of failed transfers, and shall not be confused with possible low cost solutions across the periselene. These two regions together with the other ones with negative Δv variations are highlighted by green contours.

In general, the analysis of the formation transfers with distance constraint highlighted the good capabilities of the *adaptive weights* controller to withstand distance constraints between spacecraft. A specific sample in the map of possible transfers on the torus is depicted in Fig. 4.22, where the different transfer strategies are presented, considering the optimal tri-impulsive guidance of [83], the MPC without and with CAM along the initial and final relative trajectories.

The surface of the QPT in the relative-synodic reference frame is also depicted. It can be observed how, despite large changes in the trajectory directions, the

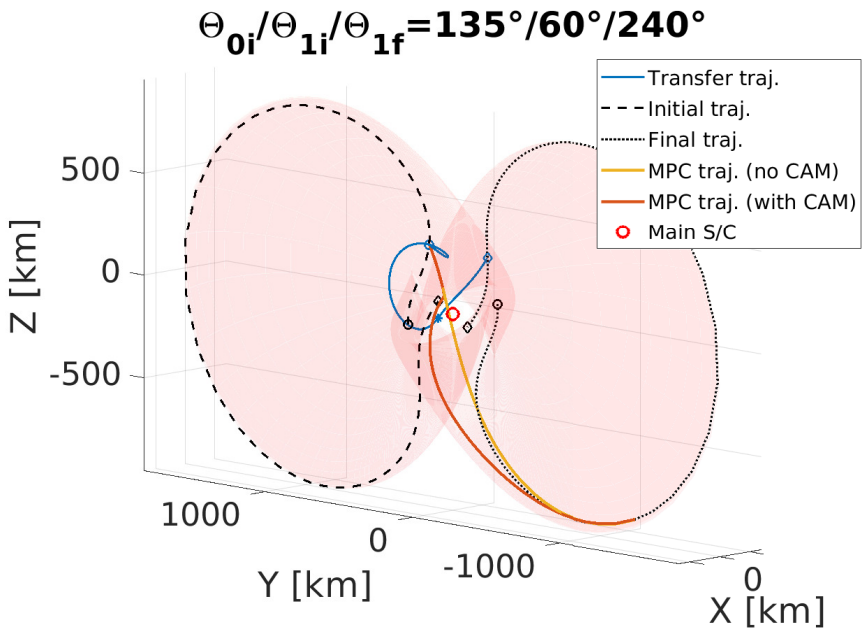

Figure 4.22: Different rephasing transfers for the tri-impulsive guidance and for the MPC with and without the CAM. Circles represent initial points, while diamonds the end of the depicted trajectories.

arrival point almost coincides with that of the MPC without CAM. In fact, the longer time taken to fly around the KOZ makes the adaptation law provide larger weights in the second half of the transfer trajectory, thus allowing the completion of the reconfiguration in nearly the same time.

4.3.3.3 High-Fidelity Dynamics

The previous sections proved that the proposed MPC scheme, with the adaptation of weights, is able to fulfil the requirements of the transfers, at feasible costs, and with the additional advantage of dealing with collision avoidance. Nevertheless, it is fundamental to address the feasibility of such a scheme in the presence of discrepancies between the on-board dynamics model and the ground-truth dynamics. In particular, the controller schemes keeps its dynamical formulation with the CR3BP, while the spacecraft dynamics is propagated in a higher fidelity model. This model comprehends the gravity from Earth, Moon and Sun, with their ephemerides-based motion, and the SRP.

Then, the MPC setup proposed in previous sections is tested and its performance is evaluated in terms of fulfilment of the position constraint at the end of the transfer, considering a final displacement from target below 2 km. By exploiting the same tuned parameters from the CR3BP case, the maps of Figure 4.23 are obtained. It can be noticed how such control scheme behaves

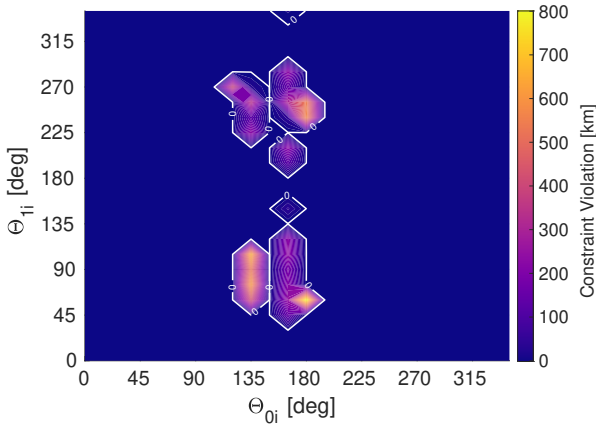

Figure 4.23: Position constraint violation with CR3BP-optimised MPC tested in the high-fidelity ephemerides-based dynamics.

quite robustly against changes in the dynamical model, with limited failure zones, all nearby the periselene region. Of particular interest is the fact that negligible cost variation was observed, with respect to the CR3BP-based cost map, and that the controller is still able to perform the CAM due to the KOZ from the leader spacecraft

4.3.4 Closing the loop with navigation

In this section, the navigation task is added to the presented guidance and control strategy, starting from the requirement definition and providing solutions exploiting different measurements.

4.3.4.1 Navigation requirement definition

To assess the robustness of the basic fixed weights guidance and control scheme against state estimation uncertainties, in Fig. 4.24 a possible complete closed-loop GNC scheme to be used is shown. The inclusion of a navigation filter in the loop, which is fed by the various measurements $\mathbf{y}_k$ provided by on-board sensors, outputs the initial conditions $\hat{\mathbf{x}}_k$ of the spacecraft in the prediction window to the MPC scheme. Note that these initial conditions are not the real ones, as the navigation will introduce deviations from the real trajectory.

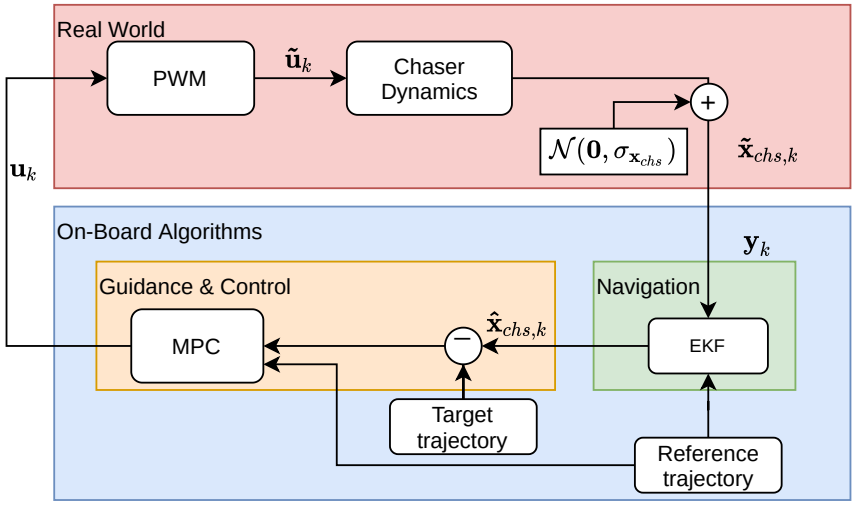

Figure 4.24: GNC scheme with a dummy EKF to emulate the complete system in closed loop.

To emulate such behaviour, the simulations of the transfer presented in the previous section for a single $(\theta_{0i}, \theta_{1i})$ couple are performed a second time, considering noisy states as initial conditions. These conditions have been obtained by generating Gaussian random noise components for each of the six elements of the state, with a null mean and different standard deviation values (grouped into a value for the position σ_r and a value for the velocity σ_v). By letting these value vary by orders of magnitude, final position error Δr_f and total transfer cost Δv_{tot} have been mapped. Table 4.5 reports the results for a specific transfer ($\theta_{0i} = 45°$, $\theta_{1i} = 135°$), including the case of a perfect state knowledge as reference for comparison.

Table 4.5: Resulting trajectory position error and total transfer cost for different levels of state estimation errors applied through a dummy EKF .

ID	σ_r [km]	σ_v [m/s]	Δr_f [km]	Δv_{tot} [m/s]
REF	0	0	2	20.4
A	10	100	190	2256
B	100	10	18	235
C	10	10	21.7	231
D	10	1	8.7	34.5
E	1	1	8.7	34.4
F	10	0.1	3.1	22.3
G	1	0.1	2.8	20.8
H	0.1	0.1	2.8	20.8

Considering an increased threshold error for the final position in the closed GNC loop of 3 km, the results highlight how the nominal outputs are reached only with $\sigma_r \leq 10\,\text{km}$ and $\sigma_v \leq 0.1\,\text{m}\,\text{s}^{-1}$. This result was expected regarding the position estimation error, due to the very strict requirement in terms of final trajectory error, but these analyses provided a boundary value also for the velocity, leading to quite demanding requirements for a navigation system. From the table, other useful insights on the proposed G&C scheme are deducted. By looking at the rows E and F, it can be noticed that a higher accuracy in the velocity components (case F) is more beneficial than reducing the position error (case E) with respect to the D configuration. Indeed, having a better position reconstruction pushes the controller to activate thrusters for longer periods, but without achieving good results due to the bad velocity knowledge. The improvement in velocity estimation is the driving factor for this GNC scheme, while position is in many conditions not fundamental. From such analysis we can set as a target of a navigation scheme the couple of 10 km and $0.1\,\text{m}\,\text{s}^{-1}$ for σ_r and σ_v respectively.

4.3.4.2 Navigation analyses

Once defined such performance requirements, the goal is to assess the feasibility of recovering such errors simulating a real filter working with reduced observables.

A possibility worth being investigated is that of exploiting Line-of-Sight angles only, coupled with the Bearing Only guidance scheme, to enhance the observability of the system. The same scheme of the navigation requirement analysis is here modified employing an EKF fed by the angular measurement only. The resulting scheme is reported in Fig. 4.25.

From the scheme we can highlight two different modifications with respect to the scheme in Fig. 4.24. First, the measurement flowing to the EKF is composed by the two angles $\tilde{Az}$ and $\tilde{El}$ (with the possibility of adding also radiometric data, as we'll see in the next steps). Secondly, the MPC block has an additional sub-block that provides the BO guidance to the scheme. This is obtained by accompanying the constraint of thrust magnitude with one of the minimum observability angle θ, expressed as in Eq. 4.72.

$$c(\mathbb{U}) = \hat{\theta}_{thr} - \arccos \frac{\mathbf{x}_{M,nat}^{\top} \mathbf{x}_M(\mathbb{U})}{\|\mathbf{x}_{M,nat}\| \, \|\mathbf{x}_M(\mathbb{U})\|} \leq 0 \tag{4.72}$$

Such enforcement of the observability angle $\theta_{thr} = 10°$ is required to be obtained after 10 hours from the start of the transfer, in order to avoid huge control actions requests at the start of the transfer. Note that, including such nonlinear

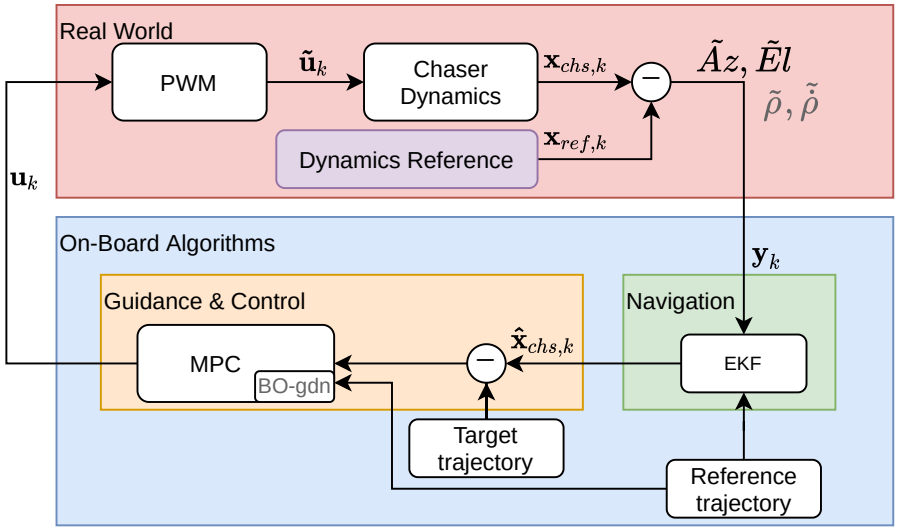

Figure 4.25: GNC scheme with closed loop.

constraint, the computationally favourable quadratic programming problem of the basic MPC scheme is transformed into a nonlinear programming one.

The results of the performed analysis are reported in the following, where an angular measurement error of $\sigma_{Az} = \sigma_{El} = 0.1°$ has been considered. Given the nonlinear formulation of the angular measurements, the LoS unit-vector's three components are directly passed as observables to the filter, leading to a simpler measurement Jacobian matrix, reducing the nonlinearities and helping the filter convergence. The measurement uncertainties of the angles are thus propagated through the RSS principle, as derived in subsection 3.3.4.1.

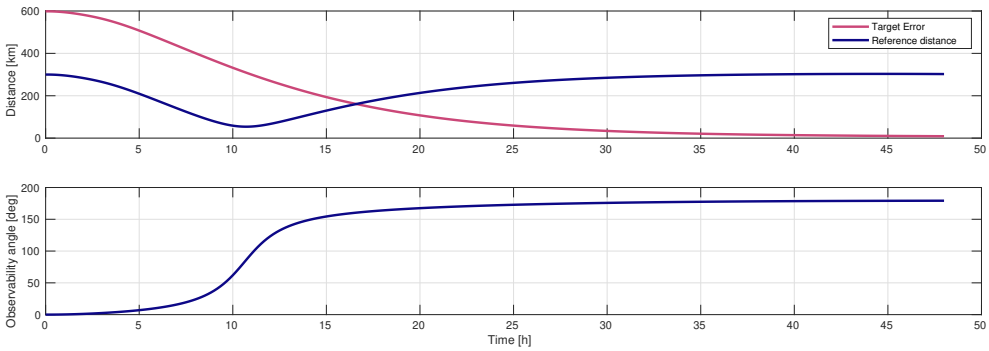

Figure 4.26: Distances to the target and reference trajectory (top) and observability angle evolution (bottom) for the basic transfer with BO guidance and angular measurement.

Figure 4.26 reports in the top plot the evolution of the distances to both the target trajectory and the reference one, i. e. the distance to the LOP-G, which is associated to the LoS vector. The geometry of the transfer is displayed in Fig. 4.27 in the synodic reference frame, with the chasing spacecraft performing a sort of fly-around with respect to the reference orbit.

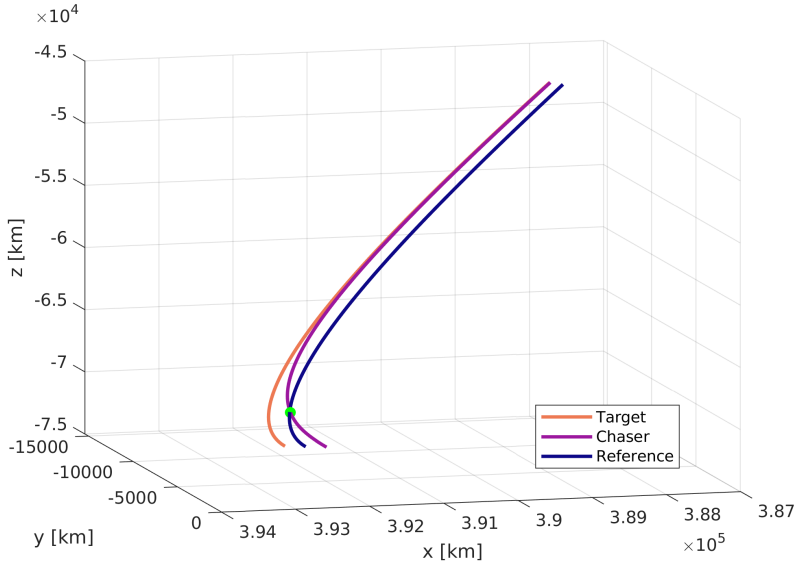

Figure 4.27: Comparison of the three trajectories involved in the synodic reference frame: the target relative trajectory, the trajectory flown by the chaser and the reference trajectory of the LOP-G. Note that for visualisation purposes the three Cartesian axes are not in scale.

It is easy thus to understand the trend of the distance to the reference of the LOP-G which shows a decreasing behaviour in the first 10 hours and then reaches a minimum value before starting increasing again. The closest approach point, marked by the green circle in Fig. 4.27, provides also the best observability angle obtainable, i. e. $\theta = 90°$ as seen in the bottom plot of Fig. 4.26, for which the range uncertainty tends to the minimum value. This effect is indeed reflected in the navigation errors provided by Fig. 4.28, where we see the best position estimation error are obtained exactly during the closest approach, where the distance is minimum and the sine of θ is maximum (recall Eq. 2.12).

By looking at the numbers, the simulations provide a final position and velocity navigation errors of around 8 km and 0.1 m s^{-1} respectively. The navigation requirements previously set seem to be satisfied but only at the end of the simulation. Indeed high errors are reached (velocity in particular) in first half of the simulation. The target position error at the end of the simulation is 8.5 km, above the threshold of 3 km.

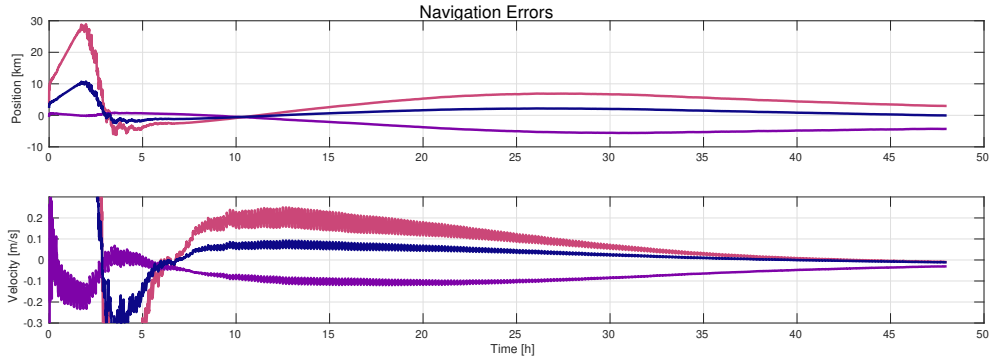

Figure 4.28: Navigation errors for position (top) and velocity (bottom) for the basic transfer with BO guidance and angular measurement.

An important fact to analyse is that the observability angle is driven to its best value of 90° and then to the maximum of 180° due to the transfer geometry, and not due to an actual effectiveness of the BO guidance. This is also proven by obtaining qualitatively the same results without the observability angle constraint in the MPC optimisation part, as highlighted by Fig. 4.29.

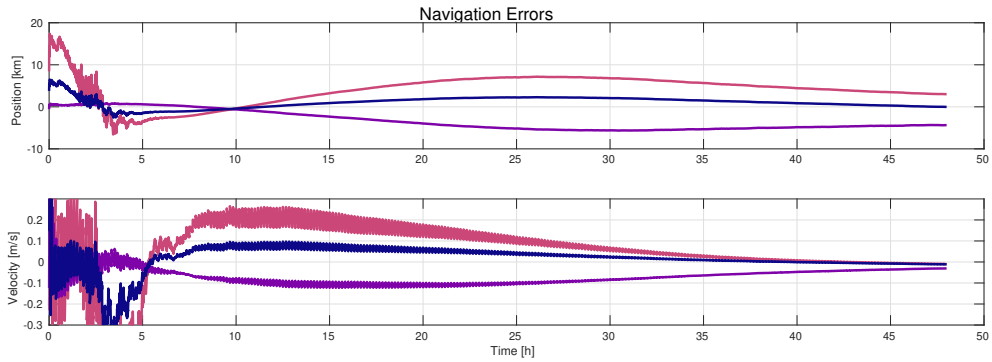

Figure 4.29: Navigation errors for position (top) and velocity (bottom) for the basic transfer with angular measurement but without BO guidance.

It is possible to say that the scenario under test, as all the formation reconfiguration points reported in the previous maps, do not take advantage of the Bearing Only guidance, since they inherently drive the observability angle to a high value in the closest approach point.

Having assessed that, the goal is now to find a way to increase the navigation performance in order to reach the goal of completing the transfer with the final target error within the threshold and keeping the fuel expenditure in the vicinity of the nominal scenario.

To achieve this, radiometric measurements are added to the set of observables, first including only the range to the LOP-G and then also the range-rate. The results are collected in Figures 4.30 and 4.31.

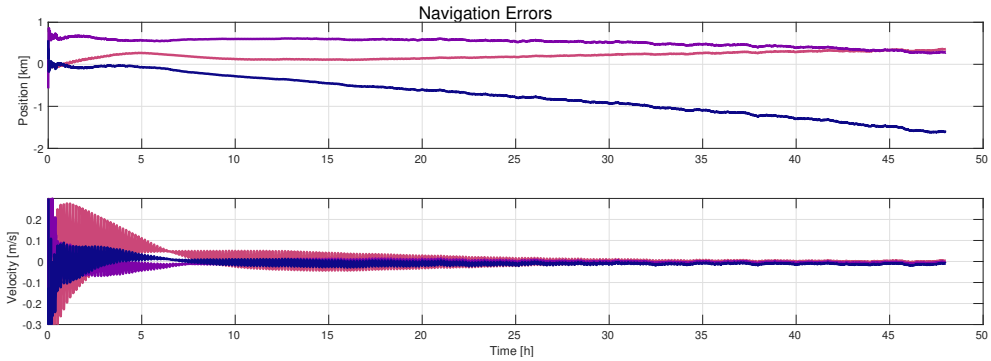

Figure 4.30: Navigation errors for position (top) and velocity (bottom) for the basic transfer with angular and range measurements.

For the first case of Fig. 4.30 we notice that a convergence of the transfer is reached with a final error 3 km and a total Δv slightly higher than the nominal $20.4\,\mathrm{m\,s^{-1}}$. The position estimation shows an incipient divergence that is not affecting the transfer strategy. Indeed the position error stays much lower than the 10 km required for the whole transfer.

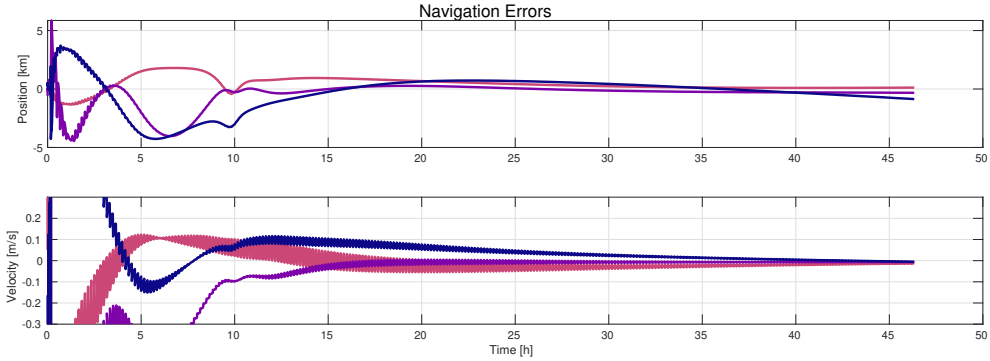

Figure 4.31: Navigation errors for position (top) and velocity (bottom) for the basic transfer with angular, range and range-rate measurements.

Adding also Doppler data, the situation improves even more, as in Fig. 4.31. With this scenario it is possible to have a stable navigation with transfer errors and costs comparable to the nominal scenario with perfect state knowledge.

4.4 Closing Remarks

This chapter provided the study of two separate scenarios dealing with design of proximity operations in the cislunar space with the LOP-G. In both analyses the complete autonomous cooperative GNC design has been based on the Model Predictive Control guidance and control scheme and on a condition with reduced state observability.

The first scenario presented in Section 4.2 has studied the applicability of BO guidance to improve the relative state estimation of a spacecraft in a rendezvous mission. In particular, it was inferred that in the cislunar space the minimisation of an objective which includes information on the range always favours a reduction of the relative distance rather than an increment on the observability angle. On the other hand, by directly targeting the angle, the guidance scheme here proposed effectively reduced the navigation error whilst remaining at relatively high distances from the target.

The effectiveness of the proposed shrinking horizon MPC architecture has been explored also in two additional non-rendezvous case studies: a planar case considering the DRO to L2 Lyapunov and an out-of-plane one , with a DRO to Halo relative motion. In both cases, the GNC scheme has proven capable of computing observable relative trajectories through the concept of observability angle, reducing the relative error to a small fraction of the initial value. Different strategies for the definition of the fuel cost function have been proposed mimicking low-thrust and impulsive manoeuvring. The outcomes of this study broaden the range of operations for which angle-only measurements can successfully be exploited, from close-range rendezvous to long-range scenario, opening the door to a variety of missions that entail solving for the relative dynamics in multi-gravitational environments.

The second work presented in Section 4.3 aimed at the design of a control scheme for formation flying reconfiguration manoeuvres. In particular, the implemented receding horizon MPC enables a direct management of collision avoidance and thrust constraints, and provides a scheme capable of withstanding model uncertainties. To further improve autonomy, a self-adaptation of the cost function weights already successfully adopted in previous studies, has been included confirming its effectiveness also with an MPC scheme, given the faster setup and the generally lower costs with respect to fixed-value weights. Moreover, emphasis was also put on the robustness of the scheme, in presence of discrepancies between the on-board and the true dynamics. The MPC proved to be robust, succeeding at completing transfers in the new, high-fidelity dynamics, with its parameters still tuned in the simpler CR3BP model.

The addition of the navigation task to this block was performed by considering first the exploitation of the BO guidance also in this second scenario. The

resulting navigation performance was not sufficient to complete the rephasing transfers correctly and with a high enough accuracy. Moreover, this analysis found that in this scenario the BO guidance was not needed to improve the observability of the system, since the transfer already was driving the observability angle θ to its optimal value of 90°. In order to provide a closed scheme with a navigation compliant with the transfer requirements also radiometric data have been added as observables. Just with the addition of the relative range, the completion of the transfer was proven, while adding also the range-rate, improved performance was achieved.

Overall, the proposed MPC design demonstrated to be a suitable scheme to be embedded in future spacecraft flying in formation with the Lunar Gateway, provided sufficient computational capabilities of the spacecraft, and, more important, provided the combined measurements of optical and radiometric data.

CHAPTER 5

Navigation through GNSS-like lunar constellation

The third and last scenario that this thesis analyses involves the design of a constellation of lunar GNSS satellites and the definition of the associated user navigation algorithms. The dynamical environment of the main objective of this study is quite different. Among the different orbital users that may be considered for this assessment, those on LLOs have been selected, i.e. circular orbits in the 50–150 km altitude range. In the context of the Moon exploration roadmap, such orbits are foreseen to be used for many different reasons and by many missions. In addition, connected to the importance of the South Pole and the associated landing missions, polar LLOs are targeted in this work. The constellation however shall also be able to provide communication and navigation services to surface users, with a peculiar attention to the South Pole, the current most interesting surface region for scientific and technological purposes.

In this research work a complete framework for performing a multi-objective optimisation is presented, whose outputs are used to help the constellation

design process, and then to test and evaluate the navigation performance that different orbital users can achieve. The strategy of using a multi-objective optimisation is a key element, in order to maintain the flexibility and versatility that early stage mission studies require. Indeed, during phase 0/A of mission design, the requirements are usually under definition and consolidation, so it is usually not so simple to provide clear and precise performance metrics to be used in a single objective optimisation.

After this brief introduction, the chapter will go through the presentation of the optimisation setup in Section 5.1, providing the definition of the orbital search space for the constellation, the constraints and the various objectives. All such elements are put together to form the optimisation problem whose outputs are presented with the aid of Pareto plots. Among these solutions, some are extracted for their specific features and characterised.

Then, Section 5.2 presents the complete navigation filter strategy and the related simulation results. In particular, the characteristics of the EKF employed are provided, detailing the state formulation, the propagation dynamics and the different sensors and observables used. The performance of the filter is then evaluated per each one of the constellations extracted from the optimisation step, comparing the results and assessing the effectiveness of the different cost functions. A test of enhancing the estimation with optical observables is presented too.

In order to include a more dynamically challenging scenario, a propelled landing trajectory is analysed with such navigation strategy as well, in Section 5.3. The basic goal is to evaluate the behaviour of this architecture in a complete GNC closed loop. The results in a nominal scenario are presented, not before providing the description of the added guidance and control algorithms. After that a Monte-Carlo analysis with dispersion in the initial state is performed and the overall results collected.

Finally, Section 5.4, coming back to the simpler natural LLO user, performs a comparison of different filter formulations, employing Extended Kalman Filters and Unscented Kalman Filters with different propagation methods. They are first compared from a performance perspective, by looking at the state estimation errors. Then they are compared from a computational standpoint, recording and analysing the execution times. In particular this last step is performed with PIL tests performed on representative hardware, on which the prototyped navigation algorithm are deployed. In such way, it is possible also to validate the feasibility of the proposed algorithms to be successfully employed on-board.

5.1 Constellation Design

In order to perform an optimisation of the constellation with the goal of maximising the performance of the provided service, simulating the servicer-user interaction is a key element. In the following sub-sections we present the key performance indices used to construct the cost function of the multi-objective optimisation.

5.1.1 Genotype

To ensure that the performance of the constellation of satellites satisfies the different requirements and provide thus a quality and reliable service, a multi-objective optimisation procedure is set-up in line with what done in [54]. Its genotype is built in such a way that a constellation with n Keplerian Orbits is constructed. In particular, the design variables space has been defined by the following considerations.

- n: number of constellation elements, *fixed a-priori*;
- Semi-major axis (`sma`), eccentricity (`ecc`), inclination (`inc`) and argument of pericenter (`aop`) are considered to be the same for the whole constellation element.
- Considering the final service to provide to the surface user, where communication and navigation capabilities are required, we can understand that the associated operations can benefit so much by a periodicity of these services windows that is aligned with the Earth day, by exploiting a constellation period of multiples or sub-multiples of this time frame. Considering thus two extrema we can say that, having a 12 h period the resulting semi-major axis is quite low, reducing the visibility capability of the servicers, while with 48 h the semi-major axis is instead too high, where third body perturbations start adding some relevant perturbation. The orbit semi-major axis is then *fixed a-priori* to 9750.7 km, in order to ensure a period of 24 hours.
- The argument of pericenter is fixed to 90° such that the aposelene lies above the South Pole, thus spending most of the orbital period in its neighbourhood, being it the region of main interest for future missions.
- The orbits are constrained to be of the Elliptical Lunar Frozen Orbit class (see the details in [90]), in order to ensure a more stable behaviour and thus to reduce station keeping expenditure. As such the inclination is no more a degree of freedom, but it is fully defined as function of the other Keplerian elements, as $\texttt{inc} = f(\texttt{sma}, \texttt{ecc}, \texttt{aop})$.

- The right ascension of the ascending node (`ran`) and the true anomaly (`tan`) are optimised for every i^{th} constellation element.

Hence, the design variables vector $\mathbf{x}$ is defined as:

$$\mathbf{x} = (\texttt{ecc}, \texttt{ran}_i, \texttt{tan}_i)^\top \quad i = 1, \ldots, n \tag{5.1}$$

with a total number of $2n + 1$ variables.

5.1.2 Objectives and cost function

In order to showcase the flexibility and versatility of the proposed constellation design strategy, three different optimisation paths have been followed, i.e. three different cost functions are used. In particular, it is assumed that the interest is associated to the Lunar South Pole (`SP`, latitude $< -75°$) as well as the Low-Lunar Orbit (`LLO`, as polar circular orbiter in the range of altitudes between 50 and 150 km). Regarding the `SP`, the objectives identified to be minimised for the present study are:

- `SP_COMM_CONT`: percentage of South Pole users for which a 8 hours continuous window per day is not present for at least 99% of the time.
- `SP_NAV_NCONT`: percentage of South Pole users for which a daily 5 hours non-continuous time window with `2DHDOPAV` is not present for at least 99% of the time.

Instead, regarding the `LLO` region, the following minimisation objectives are identified as of interest:

- `2DHDOP_NCONT`: percentage of LLO users for which a daily 2 hours non-continuous time window with `2DHDOP` < 10 is not present for at least 99% of the time.
- `LLO_mu`: maximum among the different LLO users of the average 2-fold blind windows duration, i.e. the duration of windows where less than 2 satellites are in view, expressed in minutes.
- `LLO_sigma`: maximum among the different LLO users of the standard deviation of the 2-fold blind windows duration, expressed in minutes.
- `LLO_musigma`: Product of the previous two objectives, expressed in squared minutes. This component is added to collapse the previous two elements into a single one.
- `LLO_cum`: maximum among the different LLO users of the cumulative sum of the 2-fold blind windows duration, expressed in minutes.

From the previous objectives three different cost functions are assembled, as in the following.

- `full`: cost function comprising both `SP` and `LLO` related objectives – `SP_COMM_CONT`, `SP_NAV_CONT`, `SP_NAV_NCONT`, `2DHDOP_NCONT`, `LLO_mu`, `LLO_sigma`.
- `llo_sgl`: cost function comprising only `LLO` related objectives – `2DHDOP_NCONT`, `LLO_musigma` and `LLO_cum`, on a set of LLO users on a single `ran` value equal to 0°.
- `llo_mlt`: same cost function as before but on a set of LLO users on `ran` values spanning the range 0–360°.

The exploration of the design variable space and the generation of the Pareto fronts for the optimisation runs are performed through the exploitation of a *Multi-Objective Hypervolume-Based Ant Colony Optimisation* (MHACO) algorithm [91]. The ESA *pagmo* [92] optimisation package has been exploited for that purpose. MHACO is preferred over standard heuristic methods, such as the *Non-Dominated Sorting Particle Swarm Optimiser* (NSPSO) [93] or the *Non-Dominated Sorting Genetic Algorithm* (NSGA-II) [94], since it is shown to be really competitive with those algorithms, exhibiting superior performance in large search space exploration.

After a preliminary analysis, a population of 100 elements and a maximum number of 150 generations are considered per each one of the three optimisation runs.

5.1.3 Pareto front analysis

As described in the previous sections the optimisation scheme presented is used to run three different objective functions, namely `full` accounting for both South Pole and LLO users performance, `llo_sgl` and `llo_mlt` considering instead only `LLO` related performance, both considering mean, standard deviation and cumulative sum of the 2-fold blind windows duration, the former for a single class of LLO users and the latter for a wider selection. Moreover, each optimisation has been run letting the fixed parameter of the constellation size n vary between 4, 5 and 6, leading to a number of three optimisation runs per each cost function. In the following we analyse the collection of the results in the form of Pareto plots, showing the population of the three constellation sizes in the cost function space per each objective function.

Figure 5.1 shows the results for the objective function `full`. The associated cost function vector is six-dimensional, however in this plot only the solutions that fully satisfy the South Pole related constraint per each user are presented, i.e. those showing 0% for `SP_COMM_CONT`, `SP_NAV_CONT` and `SP_NAV_NCONT`. First from the top left and bottom left plots we highlight that being the objective `2DHDOP_NCONT` a percentage, it undergoes effects of saturation, reason for which a full Pareto front is not visible in those graphs. It is instead visible as a

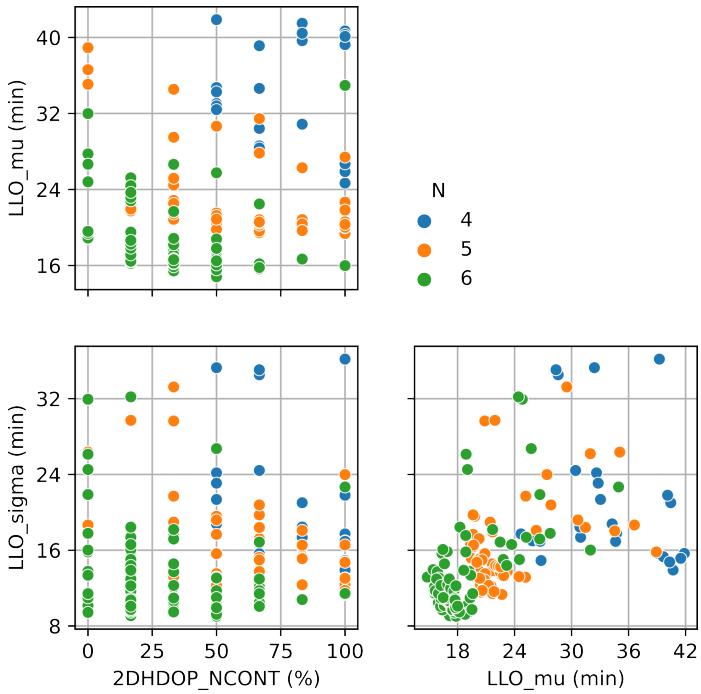

Figure 5.1: Population optimised with the objective function `full`.

clearer front in the `LLO_sigma` vs `LLO_mu` plot. To extract the best solution, the different objectives were favoured in the following manner. First the solutions with the best values for `2DHDOP_NCONT` are selected, and among those only two Pareto optimal solutions are considered, minimising one of the two remaining objectives at a time. For the run with $n = 4$ no solution with `2DHDOP_NCONT` completely satisfied (i. e. 0%) is present, reaching a minimum value of 50% of the users. The best solutions taken from $n = 5$ and $n = 6$, satisfy instead this requirement completely.

The Pareto plot in Fig. 5.2 for the objective function `llo_sgl` is easier to read, since in this case only two objectives are displayed, comparing `LLO_cum` and `LLO_musigma`.

Indeed, in this case for all three constellation sizes, there are solutions with the `2DHDOP_NCONT` saturated to 0, so the extraction of the best candidate is simply done by picking 2 Pareto points favouring one of the two remaining objectives.

Similar considerations apply also for the `llo_mlt`, whose solutions are presented in Fig. 5.3. In this case there are 0% `2DHDOP_NCONT` solutions only for $n = 6$, so the best solutions for $n = 4$ are picked among the 33.3% solutions, while those for $n = 5$ among the 16.7% solutions. Also here, two solutions optimal for the two remaining objectives are taken per each constellation.

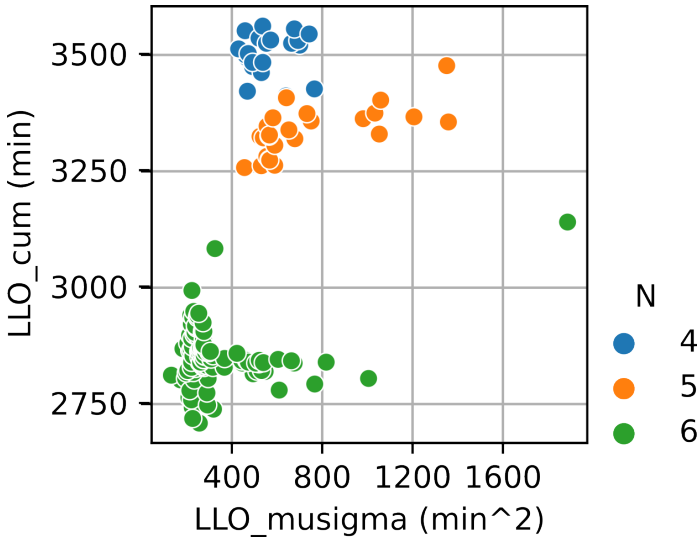

Figure 5.2: Population optimised with the objective function `llo_sgl`.

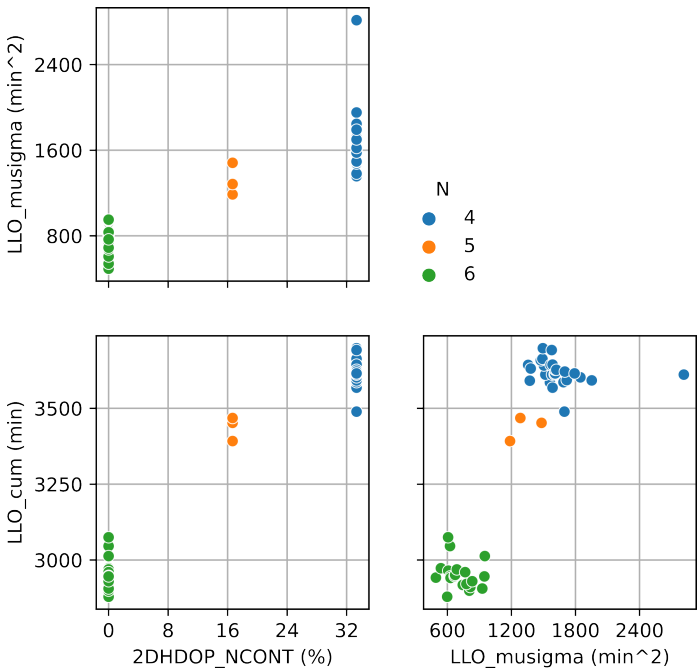

Figure 5.3: Population optimised with the objective function `llo_mlt`.

After having collected these results from the Pareto plots, we can analyse the solutions, which are summarised in Table 5.1, where also the eccentricity `ecc` and the inclination `inc` are displayed. Recall that having constrained the orbit to be frozen, the latter is always a function of the former, providing no additional degree of freedom.

Looking at the complete picture, it is possible to derive some relevant insights on the characteristics of the solutions. One of the first things that pops up is the evolution of the eccentricity value, that varies vastly from the first objective function `full`, where the upper boundary of 0.7 is almost reached, to the second one `llo_sgl` where the eccentricity reaches values lower than 0.5. This can be justified by the presence of the South Pole within the user regions for which performance shall be maximised. Having indeed higher eccentricities (recalling the imposed anomaly of pericenter of 90°) means spending more time around the aposelene, i.e. closer to the South Pole for the inclinations between 0° and 180°, enlarging the visibility duration. This value is generally decreasing for larger constellation sizes, due to the higher performance obtainable when increasing this parameter. In the third objective `llo_mlt`, instead, intermediate values of eccentricity are obtained, with the maximum value of 0.649 for the solution with $n = 6$.

Table 5.1: Summary of the extracted results, per each objective function and per each constellation size. Column `SP` comprehends all the objectives associated to South Pole users. For the `full` cost function solutions with the A label favour the `LLO_mu` objective, while those with the B label favour the `LLO_sigma` one. For `llo_sgl` and `llo_sgl` instead, A indicates favouring `LLO_musigma`, B `LLO_cum`.

Cost fcn	*ID*	`ecc` [-]	`inc` [°]	`SP` [%]	`2DHDOP_NCONT` [%]	`LLO_mu` [min]	`LLO_sigma` [min]	`LLO_musigma` [min^2]	`LLO_cum` [min]
`full`	4A	0.668	54.81	0%	50%	32	35	–	–
	4B	0.664	54.59	0%	50%	42	16	–	–
	5A	0.608	52.06	0%	0%	32	26	–	–
	5B	0.678	55.29	0%	0%	30	16	–	–
	6A	0.654	54.13	0%	0%	19	16	–	–
	6B	0.550	49.70	0%	0%	19	9	–	–
`llo_sgl`	4A	0.452	46.29	–	0%	–	–	430	3513
	4B	0.441	45.95	–	0%	–	–	640	3412
	5A	0.583	51.01	–	0%	–	–	456	3258
	6A	0.489	47.50	–	0%	–	–	132	2812
	6B	0.518	48.49	–	0%	–	–	256	2709
`llo_mlt`	4A	0.570	50.45	–	33.3%	–	–	1357	3643
	4B	0.548	49.60	–	33.3%	–	–	1696	3489
	5A	0.594	51.45	–	16.7%	–	–	1187	3392
	6A	0.556	49.93	–	0%	–	–	493	2942
	6B	0.649	53.90	–	0%	–	–	598	2879

After that, we can see that the objectives of the different solutions are always decreasing for increasing constellation size. This is expected as a general remark. It is also quite reasonable that worse values are obtained in the third objective `llo_mlt` with respect to what was obtained for the second one, which is optimised for a specific set of LLO users on a single orbital plane.

Figure 5.4 displays the geometries of the obtained constellation for three different cases. In particular, the first two plots show the selected solutions of the optimisation with `llo_sgl` for case 5A (left) and 6A (center). From the solution with $n = 5$ we see basically three orbiters clustered on similar planes, while the remaining two are placed in separate planes covering the remaining space. The 6A solution presents instead a clear clustered solution, with only two planes considered, with their node axis aligned to the x-axis of the *LME2000* inertial frame. This is indeed clear if we recall that the LLO users considered by the `llo_sgl` cost function are placed on orbital planes with the `ran` equal to 0, thus being the symmetry plane of the two clusters of servicers present in the central plot. This effect is partly present also in the 5A constellation (left plot), where the three clustered servicers have a compatible value of right ascension of their ascending nodes.

This clustering is instead completely destroyed in the right plot, where the 6A solution for the `llo_mlt` cost function is displayed. Here, we see instead a different behaviour, where the 6 orbiters are displaced on almost 6 symmetric planes. This effect is clearly determined by the targetting of different orbital plane users, with `ran` spanning the whole 360° space.

5.2 Navigation filter formulation

As mentioned above, an orbital user exploiting a GNSS constellation is characterised by an evolution that requires the exploitation of a dynamical tracking problem, which can be handled with a bayesian filter. In particular, among the different estimation algorithms, the most reliable and effective to work within a complete Guidance, Navigation and Control (GNC) scheme is the Kalman Filter, declined in all its different formulations. Given the limited size of the constellation under study, the user will eventually lose visibility with any of the servicers and consequently will need a way to continue with a propagation of its own state. To do this, a reasonable dynamical model is required on-board which, together with an accelerometer, can be beneficial in providing an inertial navigation solution for the blind windows.

5.2.1 Ground truth dynamics

In order to validate the navigation strategy, a complete high-fidelity propagation of the LLO users is required, for both simulating the dynamic evolution in the

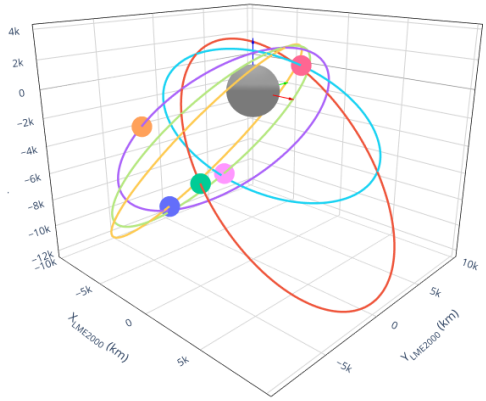

(a) `llo_sgl` 5A

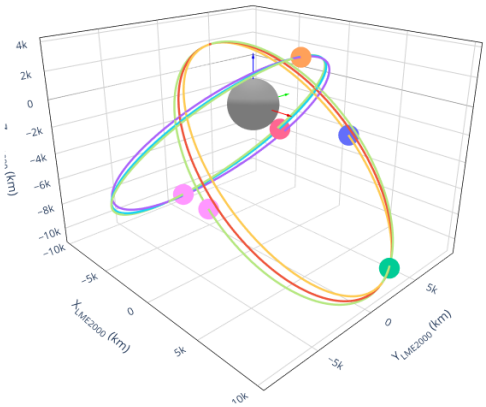

(b) `llo_sgl` 6A

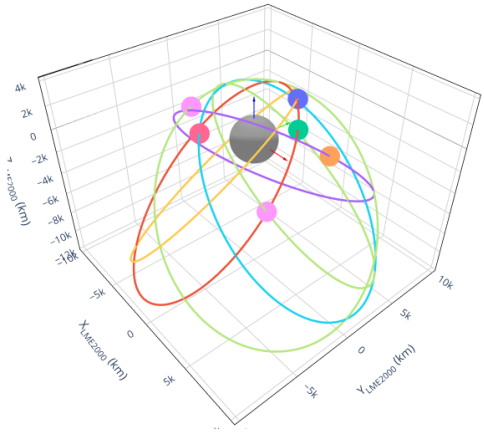

(c) `llo_mlt` 6A

Figure 5.4: Representation of three solutions extracted from the optimisation procedure for the cost functions `llo_sgl` and `llo_mlt` with the constellation sizes $n = 5$ and $n = 6$.

complexity of the cislunar environment and generating a trajectory to be used as ground truth reference.

The dynamics in which the ground truth trajectory is generated comprises two separated contributions:

- Gravitational effects
- Solar Radiation Pressure (SRP) perturbation

For the ground truth a detailed full ephemerides model is accounted for, including Moon, Earth and Sun contributions. Terms from the other Solar System bodies have been deemed negligible in the low lunar orbits environment. What was instead applied as relevant is the contribution from the Moon irregular gravitational field, expressed by spherical harmonics up to the 60^{th} order, with coefficients values derived from the LP165P model [95].

The SRP perturbation is accounted for as in Eq. 2.6. Generic values of $c_R = 0.7$ and $m/A = 150\,\text{kg}\,\text{m}^{-2}$ have been assumed for this scenario.

5.2.2 Filter structure and implementation

Given the different nature of the measurements used, a suitable way to perform sensor fusion is needed, exploiting both the accelerometer, pseudorange and pseudorange-rate information. We faced this challenge through a tightly coupled GNSS/INS formulation, as described by the scheme in Fig. 5.5.

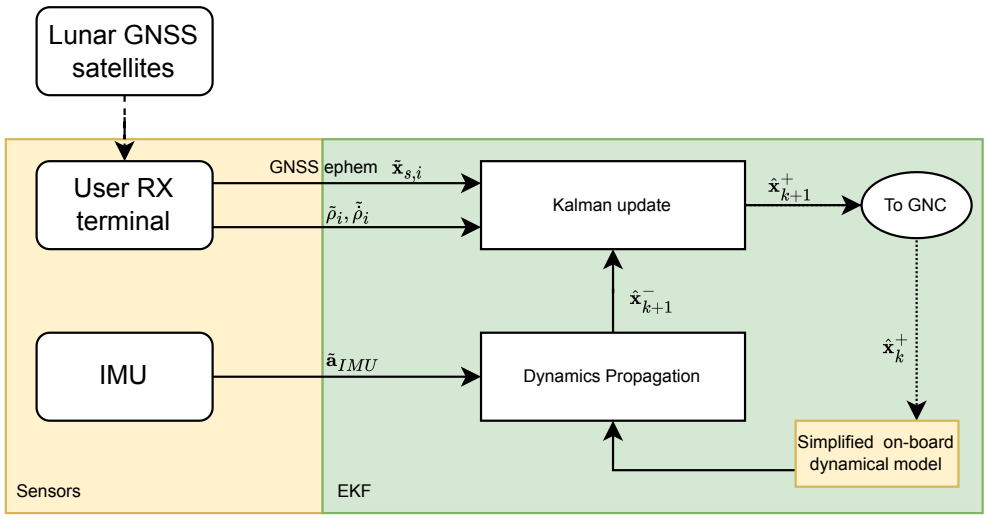

Figure 5.5: Description of the GNSS/INS Navigation formulation

The acceleration $\tilde{\mathbf{a}}_{IMU}$ measured by the IMU is exploited in dynamic compensation mode, added to the on-board dynamical model, to perform the state

prediction step in the filter, outputting the a-priori estimate $\hat{\mathbf{x}}_k^-$ at time step k. The accelerometer noisy term is taken as a zero-mean Gaussian term with a standard deviation of $3.5 \times 10^{-4}\,\mathrm{m\,s^{-2}}$, representative of standard high fidelity accelerometers.

The GNSS observables of the pseudorange $\tilde{\rho}_i$ and pseudorange-rate $\tilde{\dot{\rho}}_i$ together with the ephemeris of each constellation satellite are instead passed as measurements directly to the filter, which, by performing the update step, returns the a-posteriori corrected state $\hat{\mathbf{x}}_k^+$. The advantages of a *tightly coupled* GNSS/INS formulation over a *loosely coupled* one [96] where the GNSS receiver is considered as a black-box outputting the complete state directly reside in the possibility to exploit the GNSS signals also when less than 4 satellites are in visibility, which - for the proposed scenario - can be a very likely condition due to the limited number of constellation elements. Whenever no GNSS signal is available, the proposed architecture continues propagating on board the user position exploiting the information from the IMU only.

Given the choice to include also the clock bias b_c and drift d_c in the estimated parameters, the spacecraft state $\mathbf{x}_{S/C}$ is appended by these components, forming an overall filter state $\mathbf{x} = [\mathbf{x}_{S/C}^\top,\ b_c,\ d_c]^\top$.

The implemented filter is an Extended Kalman Filter, defined by the following simplified spacecraft dynamical model $\mathbf{f}_{S/C}(\mathbf{x}_{S/C}, \tilde{\mathbf{a}}_{IMU})$ and a clock dynamical model for the propagation and measurement function $\mathbf{h}(\mathbf{x}, \tilde{\mathbf{x}}_{s,i})$, defined as in Eq.s 5.2 and 5.3.

$$\mathbf{f}_{S/C}(\mathbf{x}_{S/C}, \tilde{\mathbf{a}}_{IMU}) = \mathbf{f}_{S/C}(\mathbf{x}_{S/C})_{\text{☽}} + \mathbf{f}_{S/C}(\mathbf{x}_{S/C})_{\text{♁}} + \tilde{\mathbf{a}}_{IMU} \tag{5.2}$$

$$\mathbf{h}(\mathbf{x}, \tilde{\mathbf{x}}_{s,i}) = \Big[\rho_1,\ \dot{\rho}_1,\ \rho_2,\ \dot{\rho}_2,\ \ldots,\ \rho_n,\ \dot{\rho}_n\Big]^\top \tag{5.3}$$

From Eq. 5.2 it is possible to see the dynamic model replacement strategy to exploit the accelerometer in the navigation filter, including thus the SRP acceleration measured contributions. Moreover, the only gravitational terms inserted here are those associated to the Moon and Earth point mass gravitational potential. The Moon irregular mass distribution and the Sun gravity are not modelled here, in order to reduce the computational burden on the on-board computer. We want also to recall that the measurement function (Eq. 5.3) uses the estimated clock bias and drift to correct the pseudorange and range-rate a-priori predictions, following Eq.s 3.52 and 3.53. Associated to these parameters, their propagation model is instead given by $\mathbf{f}_c$ defined by Eq. 5.4.

$$\mathbf{f}_c = \begin{cases} \dot{b}_c & = d_c \\ \dot{d}_c & = 0 \end{cases} \tag{5.4}$$

Stacking then Eq.s 5.2 and 5.4, we obtain the dynamical model to be used in the filter $\mathbf{f} = [\mathbf{f}_{S/C}^{\top},\ \mathbf{f}_c^{\top}]^{\top}$.

The filter is here initialised with initial conditions of the state $\hat{\mathbf{x}}_0$ and the state covariance matrix $\mathbf{P}_0$, which are both set at the beginning of the simulation. We used $\sigma_{r,0} = 1\,\text{km}$ and $\sigma_{v,0} = 1\,\text{m}\,\text{s}^{-1}$ as values for $\mathbf{P}_0$ and as standard deviation for $\hat{\mathbf{x}}_0$. The process and measurement noise covariance matrices are represented by $\mathbf{Q}$ and $\mathbf{R}$ respectively. The former can be considered as a tuning parameter, the latter is instead defined by the sensors accuracy.

The evaluation of the innovation vector defined by $\tilde{\mathbf{y}}_{k+1} - h(\hat{\mathbf{x}}_{k+1}^{-}, \tilde{\mathbf{x}}_{s,i,k+1})$ is affected by two independent errors, i.e. the pseudorange and range-rate errors (introduced by the physics of the signals transmission and the RF terminals) and the error introduced in the servicers' ephemerides (given by the servicers' own navigation budget). As such, in the definition of the covariance $\mathbf{R}$, both the radiometric and the propagated servicers ephemerides errors contributions are considered, derived with the RSS in subsection 3.3.4.2.

5.2.3 Filter performance verification

In this additional step, a subset of the extracted solutions is analysed more in depth, verifying the proposed on-board navigation scheme in terms of performance, comparing the level of accuracy obtained in the state estimation and the duration of the convergence losses due to the 2-fold blind windows. The simulation is set up for a single polar LLO user with an altitude of 50 km, a `ran` of 0° (the same as the one of the users considered for the `llo_sgl` optimisation) and a total simulation time of 48 hours.

Figure 5.6 reports the zoomed simulation outcomes for the specific case of $n = 4$ in the optimisation with the `full` cost function, ID 4A (favouring `LLO_mu` over `LLO_sigma`), in the first 10 hours of simulation.

In the plot 4 different quantities are displayed over the simulated timespan. The first row reports the dilution of precision parameters, in particular `2DHDOP` (red dots) and `GDOP` (blue dots), indicating thus also the 3- and 4-fold visibility respectively. This is directly correlated with the second row of the plot, where the total number of servicers actually connected to the user is plotted over time. The third and the last rows indicate instead the estimation error on position and velocity respectively, expressed on a logarithmic scale.

From these plots we can extract a clear trend, which is present in all the performed simulations for the whole 48 hours. There is a continuous alternation

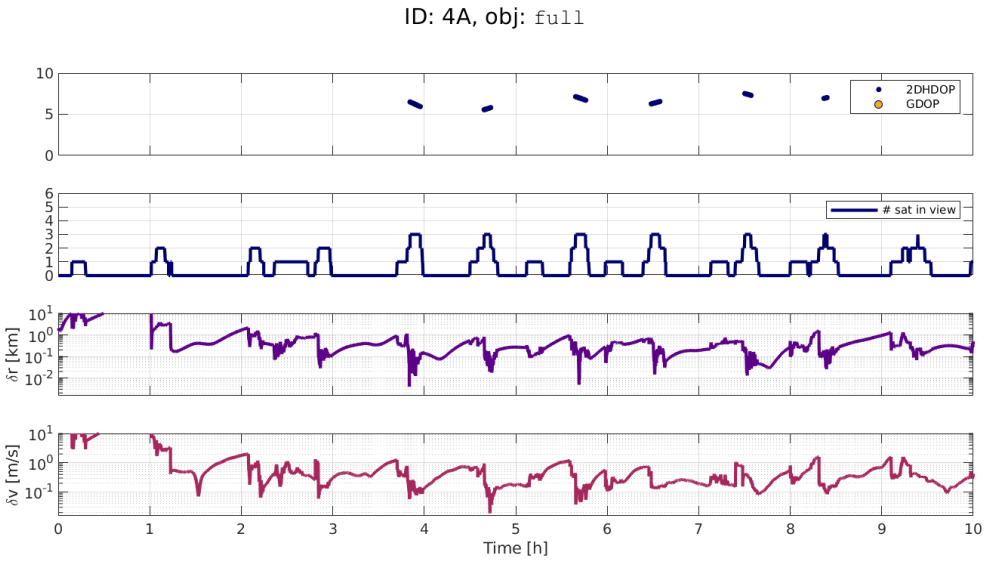

Figure 5.6: Zoomed view of the first 10 hours of navigation simulation outcomes for the $n = 4$ case of the `full` optimisation, ID 4A, minimising `LLO_mu`.

of navigation availability and blind windows. During the former, the navigation solution converges rapidly to extremely good results, with errors in the order of 10 m, practically consisting in the pseudorange measurement error. When the number of satellites in visibility is instead less than 3, the position error starts rising reaching quickly ~ 100 m and then drifting up to 1 km and even higher in the worst cases.

We can see that optimising for good `2DHDOP` values (< 10 in this case) results in extremely good performance for position estimation. It is however still limiting the presence of blind windows. In such regions, the performance of state estimation is not always satisfactory, but remains bounded below 10 km, after the starting convergence period.

In order to provide insights on the global navigation solutions, a recap of integral figures of merit is provided by Table 5.2, providing information on a subset of 8 solutions among the 16 extracted from the optimisations.

Among such indices we collected both δr`_cum`, δr`_cum1km` and δv`_cum` which are the cumulative time in hours where the navigation errors overcome 100 m, 1 km and 10 m s^{-1}. These last two values are considered as a possible threshold to define a navigation divergence, while the former defines good navigation performance. In addition to those we computed also $\mu_{\delta r}$, $\sigma_{\delta r}$ and `max(`δr`)`,

Table 5.2: Collection of navigation performance for a subset of the extracted optimal solutions, representing the different analysed cases and an LLO user with `ran`=0°.

Cost function	`full`		`llo_sgl`	`llo_mlt`
ID	4A	5A	5A	5A
δr`_cum` [h]	45.0	42.9	41.2	43.6
δr`_cum1km` [h]	6.2	5.3	3.6	10.5
δv`_cum` [h]	0.82	0.40	0.01	0.04
$\mu_{\delta r}$ [km]	0.856	0.635	0.425	0.955
$\sigma_{\delta r}$ [km]	2.776	1.455	0.438	1.437
`max(`δr`)` [km]	41.2	34.9	9.1	7.6
Cost function		`llo_sgl`		
ID	4A	4B	6A	6B
δr`_cum` [h]	45.3	43.1	39.3	40.4
δr`_cum1km` [h]	12.0	11.7	1.0	4.3
δv`_cum` [h]	0.05	0.29	0.067	0.076
$\mu_{\delta r}$ [km]	0.825	0.814	0.296	0.458
$\sigma_{\delta r}$ [km]	0.971	1.288	0.314	0.603
`max(`δr`)` [km]	9.6	18.2	10.8	13.2

which are mean, standard deviation and maximum value recorded by the position error.

In the following, different side-by-side comparisons are proposed, in order to assess the capability of the optimisation procedure to address some specific points.

5.2.3.1 Cost function `full` vs `llo_sgl`

First of all, we compare what is obtained including or not the objectives associated to the South Pole surface user, thus looking at the `full` and `llo_sgl` cost functions. In particular, the cases for constellation sizes of $n = 4$ and $n = 5$ are taken into consideration, relating the results of Pareto points A in both cases. It is relevant to recall that for the `full` case (as in Fig. 5.6), solution A favours the average value of the maximum 2-fold blind windows, while for the `llo_sgl` one (as in Fig. 5.7), it is the product of mean and standard deviation of the same quantity that is prioritised.

By looking at the scores in Table 5.2, we see that for the $n = 4$ case, there are no major improvements from keeping only the `LLO` related objectives. Indeed the values obtained for δr`_cum` and $\mu_{\delta r}$ do not differ so much, while for the 1 km threshold cumulative time, we have a practically doubled score. The only improving scores are found in the cumulative velocity threshold overcome and

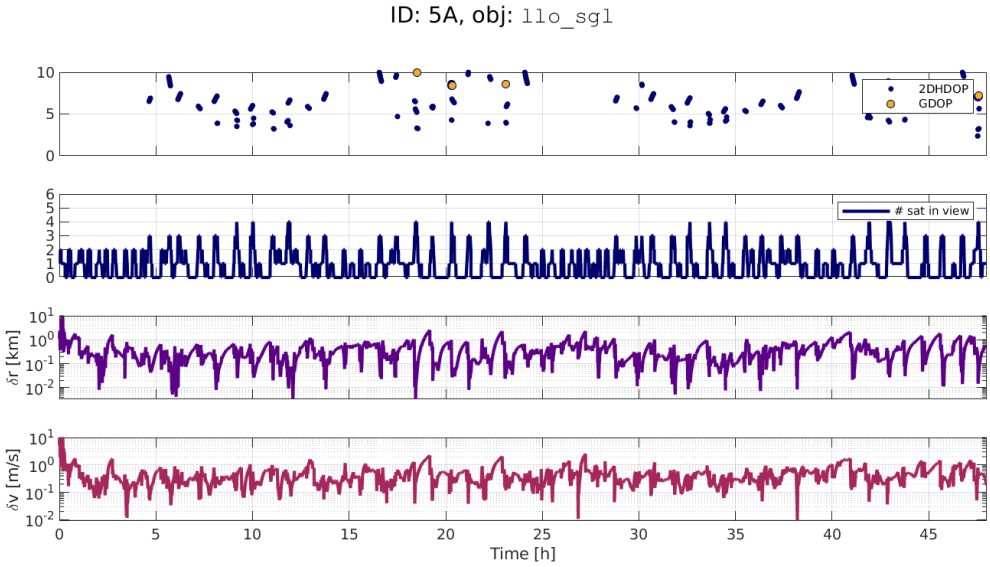

Figure 5.7: Navigation simulation outcomes for the $n = 5$ case of the `llo_sgl` optimisation, ID 5A, Pareto knee point minimising both `LLO_musigma` and `LLO_cum`.

in the standard deviation of the position error, other than the maximum error experienced.

If we analyse instead the results of the $n = 5$ case we see that a major improvement overall is present. In particular, δv`_cum` is extremely reduced as well as $\sigma_{\delta r}$ and `max(`δr`)`.

For both constellation sizes, the improvements are found principally in the position error standard deviation and maximum value. The former is the direct effect of choosing the Pareto solution comprising only the `LLO_mu` objective minimisation in the `full` cost function and not `LLO_sigma`, while in the second cost function the two objectives are already traded off, by minimising their product directly.

5.2.3.2 Objective `LLO_musigma` vs `LLO_cum`

The next comparison is performed by looking at results for solutions with ID A and those with ID B of the `llo_sgl` cost function. Recalling the Pareto points selection procedure for that specific optimisation results, we picked solutions minimising `LLO_musigma` (labelled with ID A) and others minimising `LLO_cum` (labelled with ID B). In this comparison we look at both $n = 4$ and $n = 6$, so IDs 4A, 4B, 6A (see Fig. 5.8) and 6B (see Fig. 5.9), corresponding to the bottom part of Table 5.2.

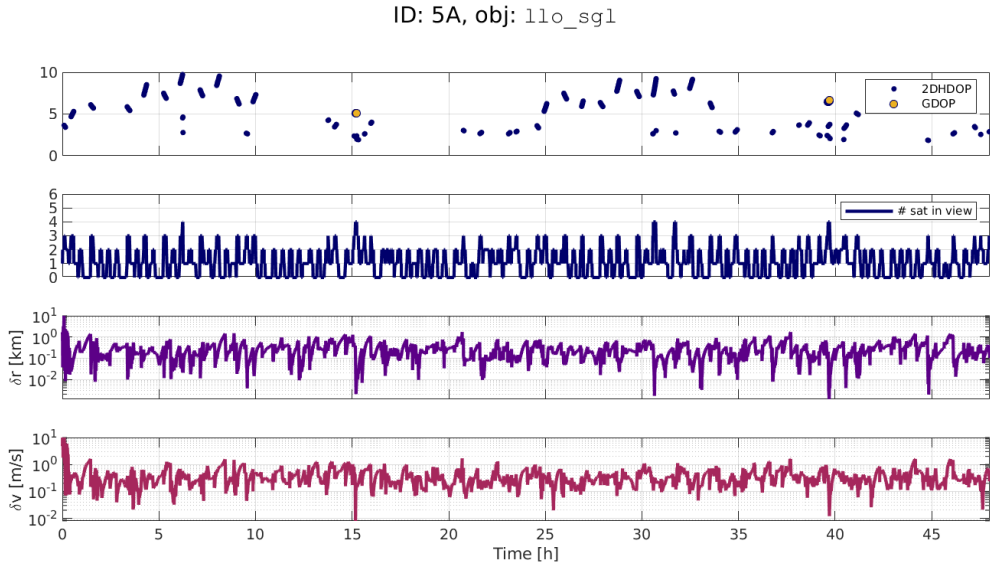

Figure 5.8: Navigation simulation outcomes for the $n = 6$ case of the `llo_sgl` optimisation, ID 6A, Pareto optimal point minimising `LLO_musigma`.

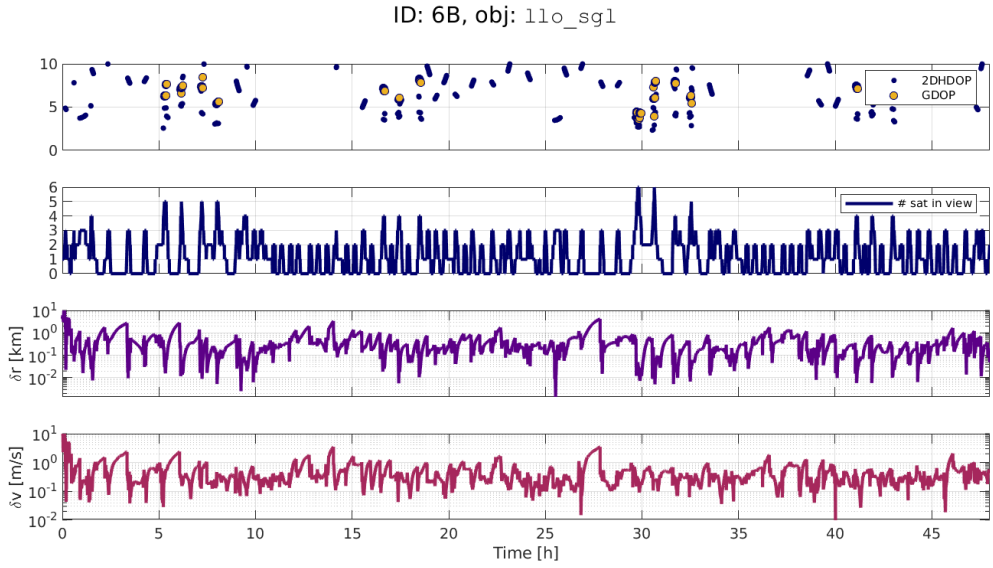

Figure 5.9: Navigation simulation outcomes for the $n = 6$ case of the `llo_sgl` optimisation, ID 6B, Pareto optimal point minimising `LLO_cum`.

In both the $n = 4$ and $n = 6$ cases we observe comparable or slightly lower performance choosing solutions B over A. For the $n = 4$ case, the solution with `LLO_cum` presents slightly higher performance in the cumulative position errors and the average value. This is instead not the case for $n = 6$, where these parameters are worse in solution B. Deteriorations of the performance are instead present in both sizes for the cumulative velocity error and for the position error standard deviation $\sigma_{\delta r}$ and maximum value `max(`δr`)`.

Moreover, comparing the first row of Fig.s 5.8 and 5.9 we can also see worse `GDOP` and `2DHDOP` values in the 6B case, although a general higher `2DHDOPAV` is present, due to the specific objective favoured in its selection.

In general, the analysed cases show that no significant improvement can be achieved in the overall performance, by favouring the minimisation of 2-fold blind windows, with respect to the minimisation of the average and standard deviation values.

5.2.3.3 Cost function `llo_sgl` vs `llo_mlt`

All the previous solutions were obtained targeting a single value of `ran`, so specialised for a single class of polar LLOs. The cost function `llo_mlt` has been set to provide performance to different orbital planes, with the goal of providing more reliable and robust solutions. The comparison we perform here is among the 5A solutions for the `llo_sgl` and `llo_mlt` cost functions, the former presented in Fig. 5.7, the latter in Fig. 5.10.

From the plots in Fig. 5.10 we can spot 2-3 hours-long daily windows with a maximum of a single servicer satellite in visibility of the user. Indeed, recall that we are considering an LLO user with `ran` at 0°, serviced by a constellation optimised for a wider variety of users with `ran` $\in [0, 120, 240°]$. As such it is reasonable that some blind windows can be found.

This decrement in performance is also found by looking at Table 5.2, where the last two columns of the upper row provide a side-by-side comparison. Excluding `max(`δr`)`, which is slightly better for the multi-plane optimised solution, we find a persistent performance degradation. E.g., the cumulative time spent with a position error higher than 1 km is practically tripled, as well as the standard deviation of the error, indicating a more discontinuous and heterogeneous behaviour. In any case, a good remark about the `llo_mlt` cost function is that there are still parts of the day when good navigation performance is present, reaching position errors below 100 m, giving the possibility to still perform most of the critical GNC tasks overall.

By looking instead at a different LLO user, placed on a plane with `ran`=90°, we obtain the results in Table 5.3.

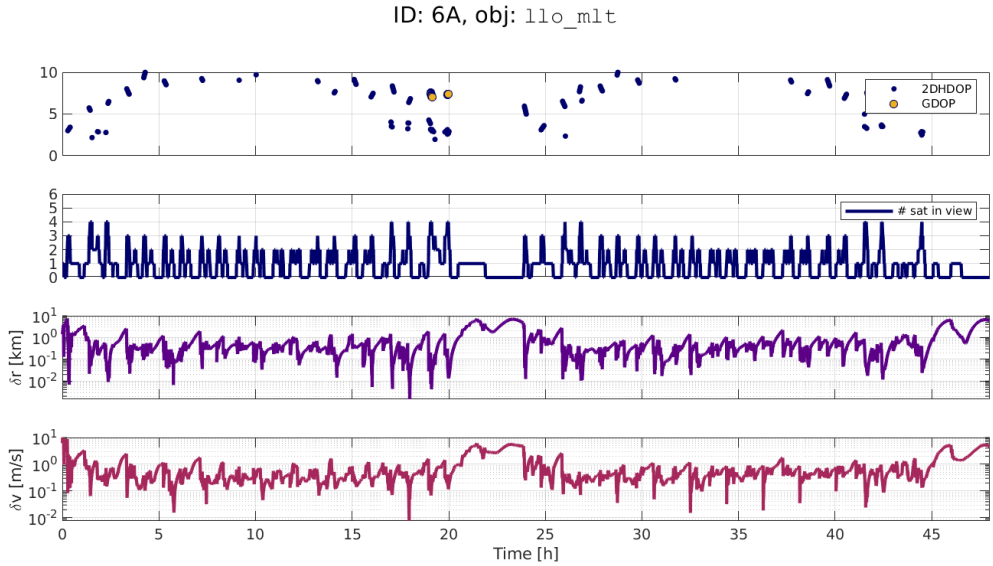

Figure 5.10: Navigation simulation outcomes for the $n = 5$ case of the `llo_mlt` optimisation, ID 5A, Pareto optimal point minimising `LLO_musigma`.

We can see here that for a user case for which the constellation was not optimised the two constellations perform similarly, with the multi-plane one, scoring worse in δr`_cum1km` and in $\sigma_{\delta r}$. Looking at the comparison of these data per cost function with respect to the results for the user at `ran`=0°, we see an important decrement of performance for the `llo_sgl` cost function, while in the `llo_mlt` case we see a much more robust behaviour, keeping the performance more similar, fulfilling the rationale behind such a constellation optimisation choice.

5.2.3.4 Constellation size $n = 4$ vs $n = 5$ vs $n = 6$

The last analysis proposed here is to verify the improvements obtained in the `llo_sgl` cost function increasing the constellation size from 4 to 5 and finally to 6.

Overall we see a continuous improvement of the performance with the peak values obtained in the 6A case. The only two parameters not following strictly the increment are the cumulative time with velocity error above $10\,\mathrm{m\,s^{-1}}$ and the maximum position error. In both situations the best score is obtained with the 5A case. If the maximum value encountered in the position error is something that levels out after the transient completion and thus not deemed as a fundamental parameter, the worse score in the velocity error parameter

Table 5.3: Comparison of navigation performance for the 5A solutions of both the `llo_sgl` and `llo_mlt` coupled with an LLO user with `ran`=90°.

Cost fcn ID	`llo_sgl` 5A	`llo_mlt` 5A
δr`_cum` [h]	45.6	44.6
δr`_cum1km` [h]	6.0	7.2
δv`_cum` [h]	0.16	0.16
$\mu_{\delta r}$ [km]	0.602	0.790
$\sigma_{\delta r}$ [km]	0.781	1.433
`max(`δr`)` [km]	11.7	11.8

can be explained likely by the higher eccentricity found in the 5A case, `e`=0.583, with respect to the 6A case, `e`=0.489. The higher value provides larger servicer velocity values excursions, thus a higher measured *range-rate* excursion, which increases the observability of the velocity itself.

5.2.4 Enhancement with Optical measurements

An additional analysis is proposed here, where the constellation `llo_sgl` 6A is taken as a basis to improve the associated navigation performance by including optical observables to the filter.

Since the goal of such analyses is to provide an insight on the enhancement of the state reconstruction capabilities, many peculiar assumptions are made that in real operative conditions may require some complex architecture, both in terms of optical sensors and/or in the related IP technique.

Indeed, dealing with the optical measurements of the LoS with respect to the elements of a constellation there are different aspects to take into consideration.

1. Cameras FoV are generally narrower than those of the antennae, but the exploitation of 180° may be very beneficial. There are some studies on the prototyping and application of such hyper hemispheric optical sensors [97, 98] that are quite promising even though the related Technology Readiness Level (TRL) is relatively low.

2. Specific on-board IP algorithms are needed to recognise a specific spacecraft in its field of view and discern it from other objects visible (e. g. stars, bodies or other servicers). Such algorithms may be very complex from an implementation point of view and their reliability shall also be assessed properly.

3. The coupling of sensor and image processing provides specific LoS angular errors that shall be particularly characterised.

In the following analyses, the previous points are addressed starting with the most favourable conditions and then removing the strong assumptions one by one reaching finally a more realistic scenario.

Regarding point 1 three different values of half-FoV are tested, namely 90°, 45° and 20°, with an angle measurement error of either 0.01° and a more reasonable value of 0.1°. Concerning the point 2, in this work no assessment of the IP complexity and the related application solution are presented. Six different scenarios of observable and recognisable satellites are considered instead: all 6 satellites of the constellation (labelled A), just one (2 different scenarios changing the one satellite, labelled B and C) or just two (three different couples tested, labelled D, E and F).

Figure 5.11 reports the result of the analysis for a 10 h timespan, in terms of relative navigation error reduction with respect to the RF-only strategy, i. e. $\Delta(\delta r_{NAV})/\delta r_{NAV}$). The labels in the legend indicate with a letter the the 6 different cases of number of servicers recognisable and with a number the value of the half Field of View (h-FoV) in degrees. Moreover in the first row, an additional "c" is added to indicate that the angular error is 0.01°, while the other scenarios consider 0.1°. The results reported in the figure suggest

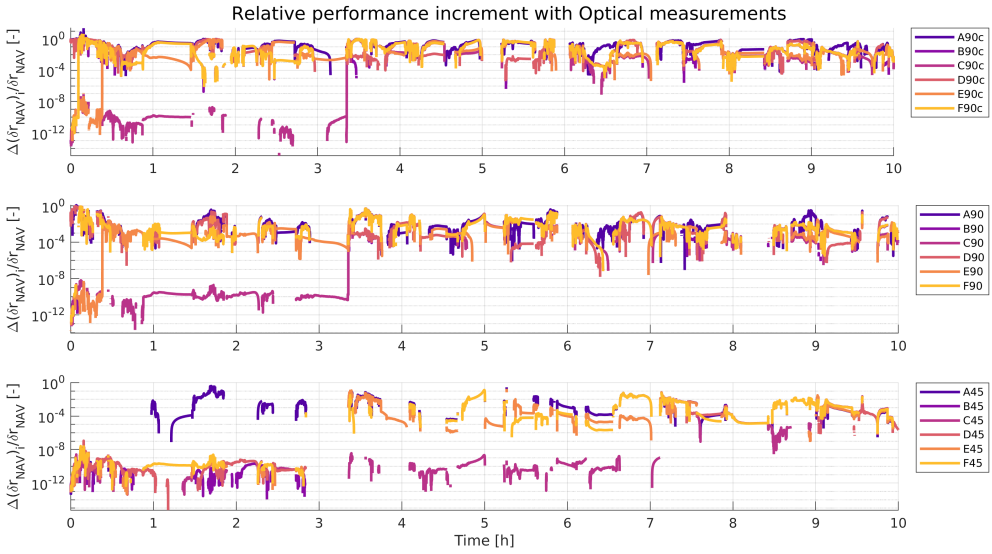

Figure 5.11: Relative navigation error reduction with respect to the RF-only strategy of different test cases exploiting the optical measurements.

that even in the most optimistic case A90c, which is the most complex to be realistically implemented, of 90° h-FoV and 0.01° of angular error with all the six satellites exploitable, the increment in performance is limited to ∼10% of the navigation error reduction. For the other analysed case, this reduction is

completely negligible or non-existent, as e.g. for the case where the h-FoV is 20°, where there are, in the analysed window no visibility periods at all.

From such results we can conclude that an enhancement of the navigation performance with optical measurements is excluded in this scenario as a viable option, given that the modest increment obtainable requires additional system complexities that are not worth the small navigation error reduction.

5.3 South Pole Landing case study

In the two previous sections, a method to design a GNSS constellation has been proposed and then a filtering architecture has been tested for LLO users in a completely natural trajectory. In the previous analyses, thus, only the navigation task was taken into consideration. The goal of this section is to present a complete GNC chain in order to test the obtained performance with the `llo_sgl` 6A constellation, for a more dynamically challenging scenario. The case of a South Pole lander is analysed here considering only the main braking phase of the landing. Starting from an elliptical orbit (100×15 km altitude) the lander starts its thrusted arc at the periselene of 15 km and ends at 1 km altitude, before relative navigation hand-over. The terminal landing phase is not included in this analysis, since it cannot be separated from the exploitation of a fully relative navigation strategy.

The considered GNC architecture is presented in Subsection 5.3.1, together with the results of the nominal landing scenario. After that, the sensitivity of the approach is tested through a Monte-Carlo analysis in Subsection 5.3.2.

5.3.1 GNC strategy

The strategy exploited in this landing scenario relies on the architecture shown in Fig. 5.12.

From the real world simulation, the dynamics of the lander and of the servicers is propagated in a high fidelity environment and the sensors readings are generated. These are fed to the navigation block whose output is the absolute state estimation. The guidance and control block employs this state together with the targetted trajectory to generate a control action $\mathbf{u}_k$. This control action is perturbed before entering the lander dynamics, by simulating both a pointing and magnitude zero mean additive Gaussian errors. The former presents a standard deviation of 1° on each of the two angles defining the thrusting direction, while with standard deviation equal to 0.1% of the maximum thrust.

The guidance and control strategy employed in this case is to provide an offline optimised landing trajectory that is interpolated on-board and then fed to a reference tracking controller, based on a PID regulator.

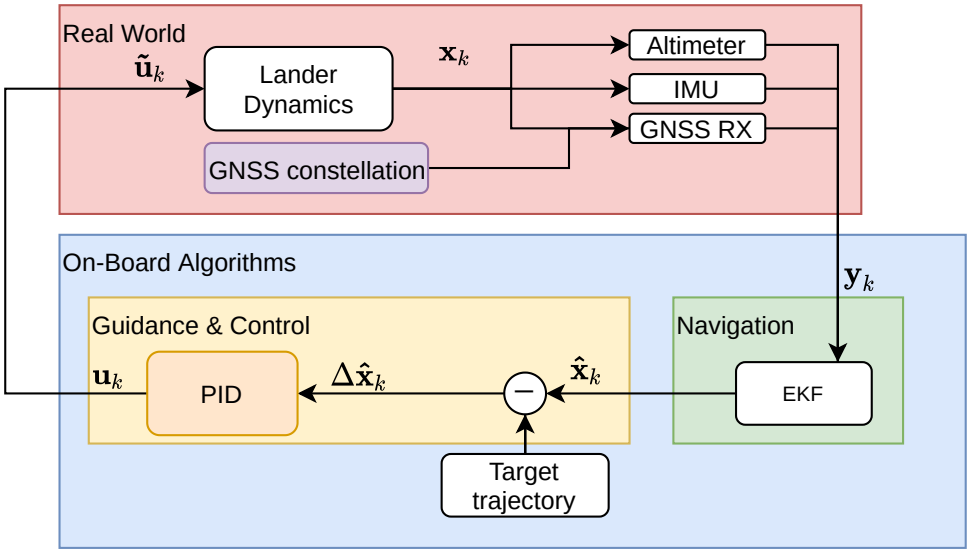

Figure 5.12: Architecture of the GNC scheme used for the landing analysis.

The trajectory used for the guidance is generated offline an indirect optimisation procedure similar to the one presented in [4, 99], where the final altitude of 1 km above the south pole is imposed. Such trajectory is imported just as a sequence of states, since the control action is recomputed using the PID controller described by Fig. 5.13. The input of this block, $\boldsymbol{\Delta\hat{\mathbf{x}}_k}$, is computed

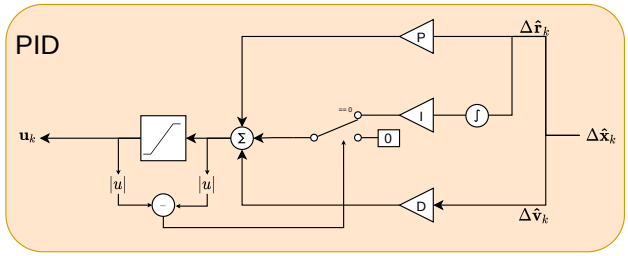

Figure 5.13: Details of the PID scheme used to follow the offline optimised guidance, employing an anti-windup logic.

as the error between the setpoint trajectory state at time t_k and the current estimation of the state $\hat{\mathbf{x}}_\mathbf{k}$. This state error, is decomposed into its position and velocity parts, $\boldsymbol{\Delta\hat{\mathbf{r}}_k}$ and $\boldsymbol{\Delta\hat{\mathbf{v}}_k}$. The former is used for the proportional and the integral parts of the control, while the latter for the derivative one. The sum of the three components passes then through a saturation block, in order to impose the maximum thrust constraints. To prevent uncontrollability due to the control saturation caused by the integral term, a simple *anti-windup*

logic [100] is introduced. The computed control action before passing the saturation step is compared in absolute value to the output of the limiter. A non-null difference means that the saturation is active, so to avoid controllability issues, the integral term is driven to zero. In such a way the regulator is able to avoid the windup condition, for which a saturated control action would continue increasing the integral of the error. The anti-windup logic remains active as long as the control acts to reduce the error and consequently re-enter the saturation limit.

The navigation instead is performed through an EKF which employs as in the previous cases of this chapter the GNSS/INS strategy, fusing these observables with an altimeter readings. In a landing scenario the employment of such instrument is fundamental for both state estimation enhancement and safety reason. The presence of the IMU, used also here in dynamic model replacement, provides the possibility to retrieve directly a measurement of control acceleration $\tilde{\mathbf{u}}_k$ to be fed in the EKF prediction step, avoiding using the acceleration predicted by the controller $\mathbf{u}_k$. Indeed, the measurement error introduced by the accelerometer is much lower than that introduced by the real actuator model.
Given the complex and more dynamically challenging scenario, the filter update frequency has been set to 10 Hz.

The simulation of the nominal scenario considers a start at the apocentre of the parking orbit and the lander begins its controlled phase after half of its orbital period, i. e. after roughly 3400 s. The trajectory followed in can be seen in Fig. 5.14, superposed to the landing guidance trajectory. A zoomed trajectory of the propelled arc is instead present in Fig. 5.15, with the view taken directly on the landing trajectory plane.

The results from a GNC point of view are instead displayed in Fig. 5.16, where both the estimation and control errors are plotted over the simulated time on a logarithmic scale. Note that the control error plot starts slightly before $t = 1$ h, i. e. when the propulsive leg begins. An initial condition with a reduced number of satellite in visibility is considered, in order to validate the system concept also in a worst case reduced observability scenario.

The results are also in this case dependent on the number of satellites in visibility. Indeed, for the first part of the trajectory the navigation error remains quite high, until a new servicer enters the visibility of the lander, just before $t = 0.4$ h. At that instant the navigation error drops to the order of $\sim$100 m, and reducing even more around $t = 0.8$ h. When the control action starts, the initial oscillatory behaviour of the thrust acceleration is reflected on both the navigation and control errors, which eventually stabilise to the final values of ~ 200 m and ~ 400 m respectively.

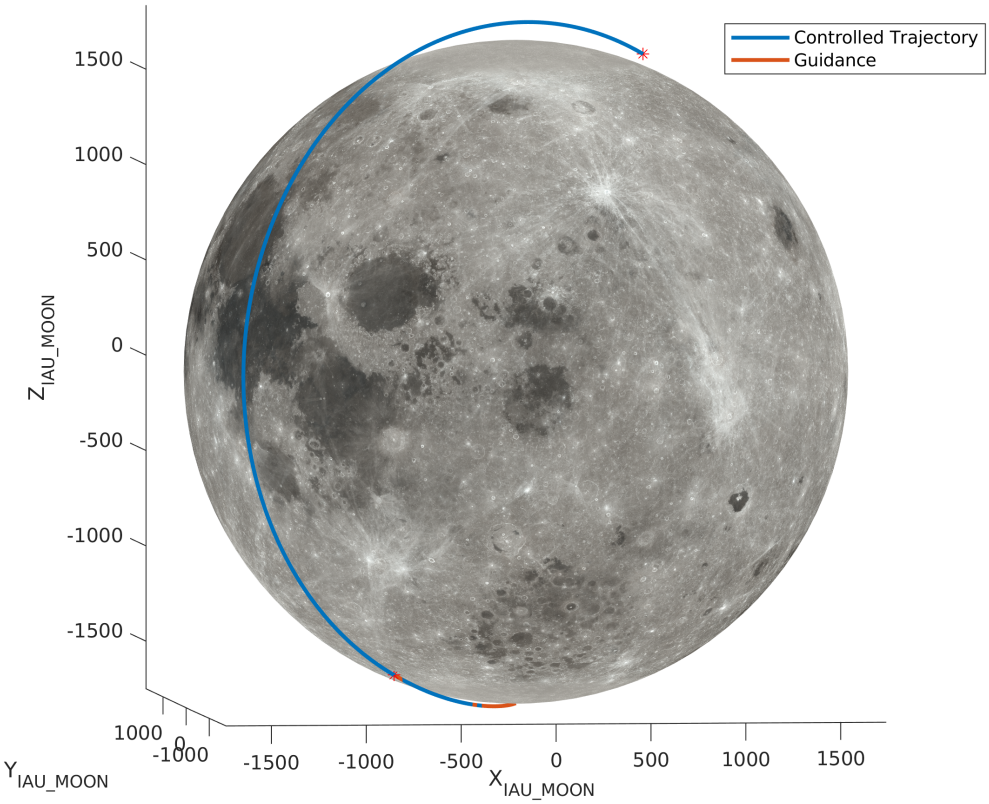

Figure 5.14: Representation of the trajectory in the `IAU_MOON` reference frame. The trajectory followed by the spacecraft is plotted in blue, overlapped on the guidance for the thrusted arc in red.

It is useful to remark that, the filter is in a stable and converged status just before the start of the control phase, which is reflected by the low values in the covariance matrix $\mathbf{P}$. This effect gives a high stiffness to the filter, that prevents its convergence to the new correct status at the beginning of the thrusting phase. In order to overcome this issue, the covariance matrix is re-initialised to 10% of its initial condition $\mathbf{P}_0$ at the beginning of the thrusted arc. In such a way, the filter is made more flexible and driven at convergence to the new state.

Overall we may say that the GNC performance is satisfactory for the scenario under study, giving the possibility to follow the prescribed guidance, with errors below 1 km. The navigation error of $\sim$ 200 m at the final instants after the filter post control re-convergence is characterised by a Root Mean Squared Error (RMSE) of around 120 m in the two horizontal components and of 15 m on the vertical one. The associated control errors show for the horizontal components a RMSE values of 330 m while a value of 90 m for the vertical

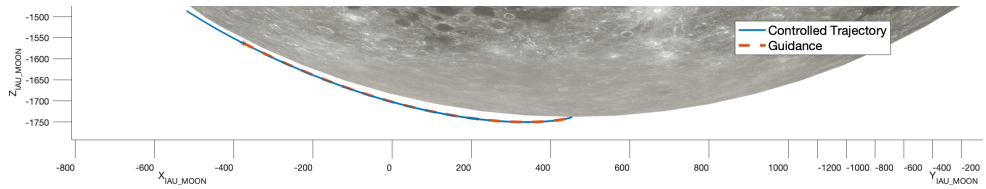

Figure 5.15: Zoomed on the thrusted arc, viewed on the plane of the trajectory.

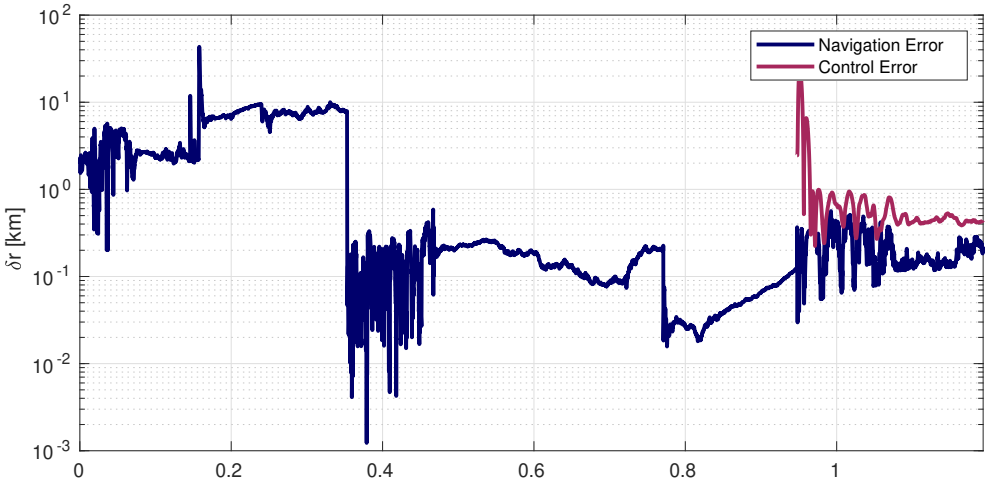

Figure 5.16: Navigation and control error of the landing trajectory, plotted in logarithmic scale.

component. This difference between horizontal and vertical errors show how fundamental is in any case the presence of an altimeter.

Moreover, testing the same landing scenario, but shifted in time in order to track a window with an overall higher number of servicers in visibility, the navigation errors drops below 100 m also during the thrusted phase, with final control error slightly below 200 m.

5.3.2 Monte Carlo Analysis

In order to consolidate the landing scenario, the sensitivity of its performance is analysed with a Monte-Carlo analysis, collecting the outcomes of a set of 500 sampling trajectories.

The parameters that are let vary to generate the samples dispersion are the start time of the landing phase, and a state error in the associated initial condition. The basic idea behind this choice is that by changing the start time of the landing, the visibility condition of the GNSS constellation is shuffled as

well, providing a distribution of different observability level per each sample. The error in the initial condition is instead added to provide perturbation of the nominal scenario, testing thus the robustness of the GNC chain.

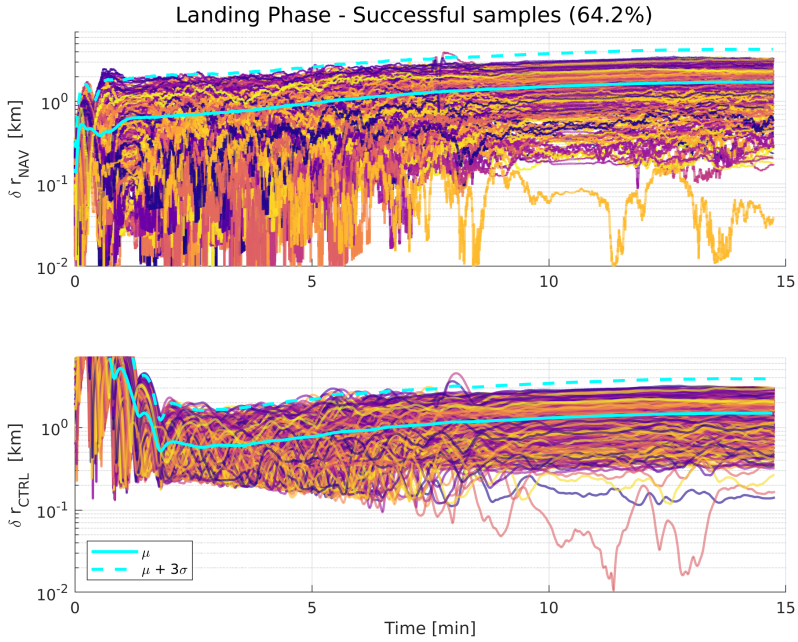

Figure 5.17: Navigation (top) and control (bottom) errors of the successful landing trajectories, with average and upper 3σ bound in logarithmic scale.

The landing starting time t_S is sampled from a uniform distribution in the range $3000 \div 5000$ s, recalling that the nominal scenario had t_S equal to 3400 s. In practice, this is imposed by shifting the initial true anomaly of the orbit backward in time, such that at the $t = t_S$ the lander is at the periselene at 15 km of altitude and the landing can start. The error dispersion in the initial condition is instead introduced as additive zero-mean white Gaussian terms with standard deviation of 500 m and 0.5 m s^{-1} in magnitude per each position and velocity component respectively. The simulations are stopped when the 1 km altitude is reached and, considering a threshold of 3 km of horizontal error, the samples are classified into successful and failed one.

Figures 5.17 and 5.18 provide the logarithmic evolution of navigation (upper plot) and control (lower plot) position error for the successful and failed samples during the thrusted arc only. The colour of the lines reflect the value of t_S, from the lowest in dark violet to the highest in yellow. The green lines represent the average (solid) and the 3σ upper bound (dashed), considering the represented lines.

A success rate of 64.2% is reached with the proposed architecture. As we can understand by looking at the line colour distribution, there is not a specific correlation between the landing start time t_S and the navigation and control errors δr_{NAV} and δr_{CTRL}. The best results among the successful case, are comparable to the nominal case, with few samples that even outperform it, with control errors slightly below 200 m. Looking instead at the worst cases in the failed samples, the upper 3σ bound is higher than 5 km.

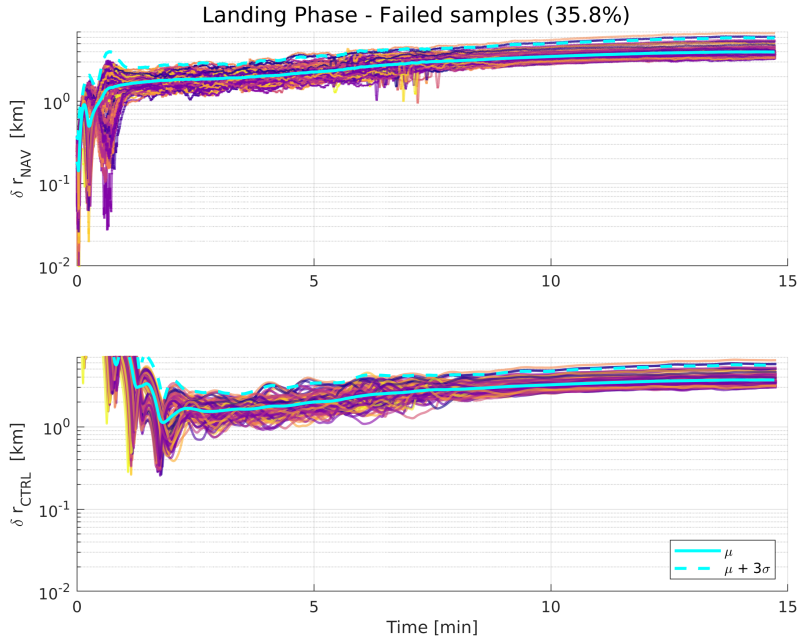

Figure 5.18: Navigation (top) and control (bottom) errors of the failed landing trajectories, with average and upper 3σ bound in logarithmic scale.

Additional insights are presented by Fig. 5.19, where cumulative distribution of both the average number of satellite in view (top) and average navigation error (bottom) evolutions are plotted for the two classes of samples.

Here we see a peculiar behaviour of the average number of GNSS servicers in view. First of all, the relative number of samples that never see a lander during the propelled leg are more than doubled in the *failed* class. This difference in relative number is recovered by the *successful* class in the range from 0 to ∼0.4 of the abscissae, while in the rest of the range from 0.5 to 0.8 the two evolutions are similar. This means that the average number of satellite in view is not a sufficient nor a necessary condition to complete successfully the landing. Looking instead ad the mean navigation error of the bottom plot, it is possible to notice a more or less constant population of samples up to the abscissa of 2.5 km for the successful samples, with no points at all above this value. For the failed ones instead more than two thirds of the trajectories are above

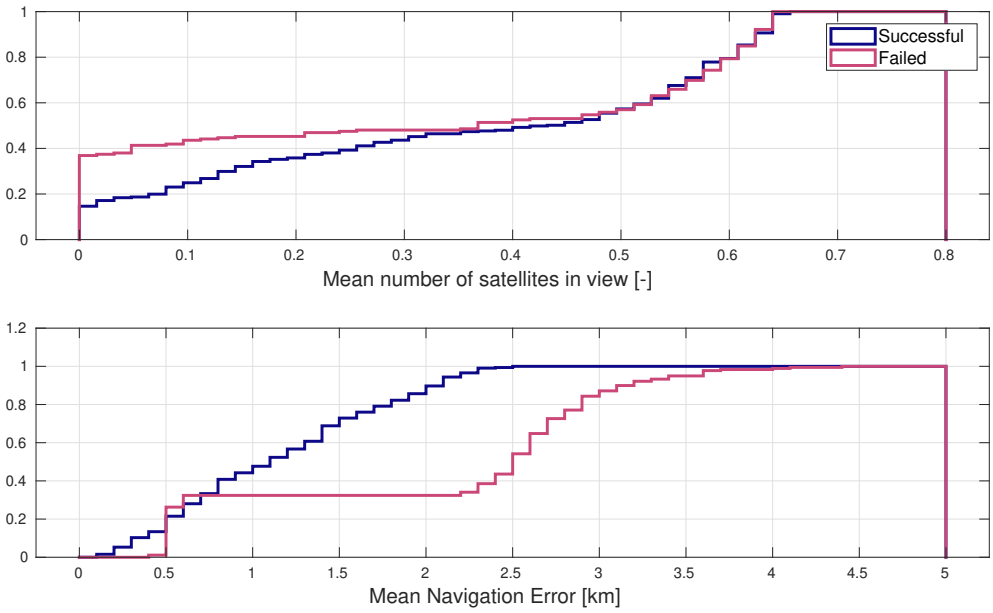

Figure 5.19: Cumulative distributions of the average number of satellites in visibility.

2.5 km. There is a minor part of failed samples with average errors around 500 m, whose failure is likely caused by highly perturbed initial conditions due to the imposed dispersion.

An interesting visualisation of the successful trajectory is obtained by looking at the final points observed on the horizontal plane at 1 km altitude. This is what the scatter plot in Fig. 5.20 represents together with two sets of covariance ellipses.

The grey ellipse represent the 3σ covariance of the estimated trajectory in the nominal scenario, while the remaining three ellipses represent the three sigma levels of the successful Monte-Carlo samples. It is remarkable to see that the nominal scenario covariance ellipse (the grey one) encloses the vast majority of the samples, thus providing a sensible estimation of the landing mission dispersion. The 3σ uncertainty ellipse of these sample is characterised by a semi-major and semi-minor axes of 1.51 km and 0.57 km, the former mostly aligned with the $X_{\text{IAU\_MOON}}$ axis, the latter with the $Y_{\text{IAU\_MOON}}$. The same preponderance of the error on the $X_{\text{IAU\_MOON}}$ axis is present also in the nominal scenario covariance ellipse, which encloses practically all the obtained samples. This elongation is caused by the geometry involving the user and the only servicer that is visible in this specific time-frame. Its LoS with respect to the South Pole (where the lander practically is placed) during the few minutes of thrusted arc has a relatively large variation along the $Y_{\text{IAU\_MOON}}$ axis and

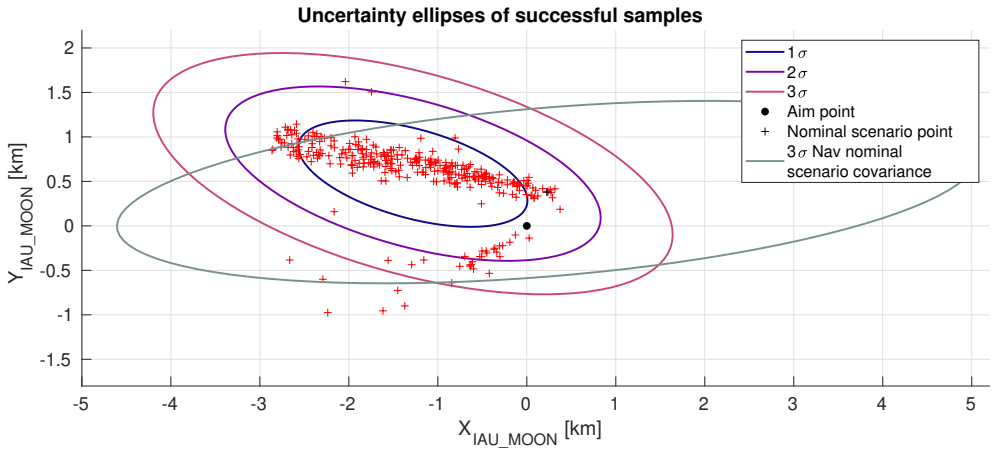

Figure 5.20: Covariance ellipses of the successful Monte-Carlo sample, taken on the 1 km altitude horizontal plane.

practically null one along the $X_{\text{IAU\_MOON}}$ axis, causing the y component to be much more observable, thus with a reduced error.

A last remark on the samples reported here is that there is a clear pattern of points that deviate partially from the main ellipses, aligned in a different direction with respect to the semi-major axes. To understand their nature, we see that they all have negative error in the y component, δy.

Figure 5.21 reports different quantities recorded per each sample, as function of the landing start time t_S. The upper plot represents the final control error on y, δy, the middle the final navigation error δr_{NAV} and the lower the average number of satellite in visibility during the thrusted arc. From the upper plot we can see a clear correlation between t_S and the final error on y, since all the sample with $\delta y < 0$ are confined in the range of $t_S > 4800\,\text{s}$. Then, from the lower plot, the cause of the different orientation of such reduced number of samples can be found in the fact that all of them performed the whole landing with no GNSS servicer visible. This means that their navigation solution does not benefit from the radiometric data during the new filter convergence procedure, leading thus to a different navigation solution, biased by the errors before starting the controlled phase.

From the middle plot, instead it is possible to notice that the final value of the estimation error δr_{NAV} is not particularly correlated with t_S. To validate also numerically these effects, Pearson's linear correlation coefficients are computed to provide a simple estimate on the correlation that the start time t_S has with both the final δy and δr_{NAV}. The resulting values are

- $\rho(t_S, \delta y) = -0.431$

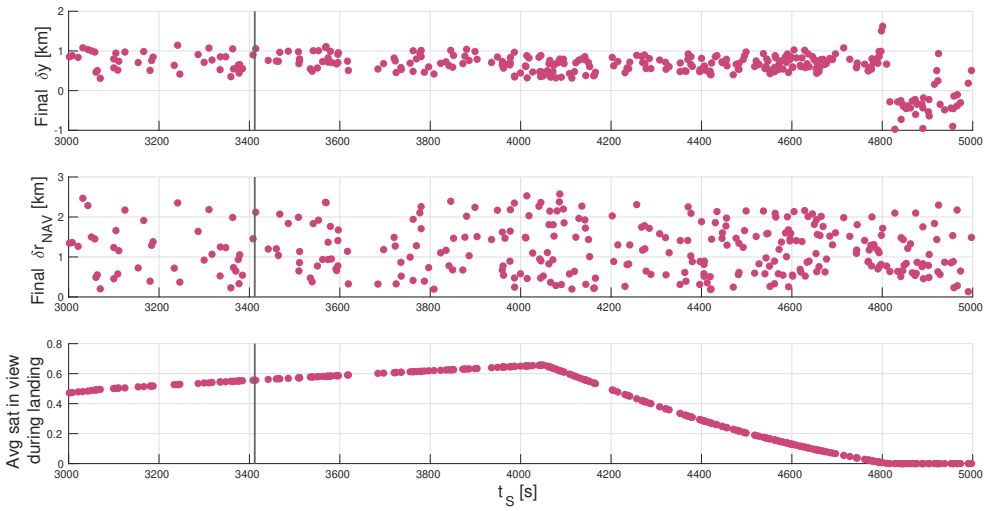

Figure 5.21: Plots representing final control error on the y component (top), the final overall navigation error (middle) and the average servicers in view during the thrusted arc (bottom) as function of the landing start time t_S. The vertical line indicates the value of t_S associated to the nominal scenario

- $\rho(t_S, \delta r_{\mathrm{NAV}}) = -0.045$

which confirm that the starting time influences the extent of the y component control error, but not the total position estimation error.

With such Monte-Carlo analysis, we gained clear insights on the statistical behaviour of the landing GNC strategy, which provided an acceptable success rate, but that may be increased with a precise start time scheduling, aiming at precise higher visibility windows.

5.4 Filter comparison and PIL testing

The last analysis performed in this chapter is represented by the comparison of different navigation filters exploited by a polar LLO user with the `llo_sgl` 6A constellation. Two different standpoints are focused here: the navigation performance and the computational complexities.

The filters considered are a total of six, i. e. three EKFs and three UKFs, differing in the integration method employed for the propagation step. The three integration methods evaluated are:

- *Forward Euler* method: the simplest and less computationally demanding one, requiring a single dynamical function evaluation.

- *Heun* method: a slight modification of the Euler method, belonging to the class of Runge-Kutta solvers with 2 steps, requiring two functions evaluations.
- *Runge-Kutta-Fehlberg 7(8) (RKF78)*: a $7/8^{th}$ order solver of the Runge-Kutta family with adaptive stepsize. Its implementation requires 13 functions evaluations.

The RKF78 method is considered as the high accuracy and reliable solver. It is also the same method employed by the filters used in the previous analyses of the chapter.

These six filters have been used to estimate the LLO state for a 48 h simulation time starting from the same initial conditions and with the same filter initialisation. Table 5.4 collects relevant statistics for all the six simulations, while Fig. 5.22 reports the time evolution per each filter.

Table 5.4: Collection of navigation performance for the six different filter formulations, considering maximum, minimum, average and root-mean-squared error of the position estimation error δr.

Filter	ODE solver	max(δr) [km]	min(δr) [km]	$\mu_{\delta r}$ [km]	RMSE(δr) [km]
EKF	Euler	19.03	0.015920	4.1010	5.1260
	Heun	10.93	0.001115	0.2975	0.4363
	RKF78	10.93	0.001151	0.2977	0.4367
UKF	Euler	19.03	0.015940	4.1	5.1250
	Heun	10.92	0.001112	0.2975	0.4363
	RKF78	10.93	0.001148	0.2977	0.4367

The results show that the performance obtained with the Heun and the RKF78 methods is in practice the same, for both the EKF and the UKF, while the performance of the forward Euler scheme is not acceptable, with errors during blind windows after the filter convergence reaching values even higher than 10 km. Moreover we see also that there is no noticeable difference in performance among the EKFs and the UKFs. This fact highlights that for the system under study, in its natural uncontrolled motion the state estimation process does not present relevant non-linearities, whose role could have caused the UKF to perform better.

5.4.1 Processor-In-the-Loop tests

To compare the computational demand of a flight-ready algorithm and to validate the on-board implementation of the prototyped code, a PIL test campaign has been put in place, considering a Raspberry Pi 4 single-board

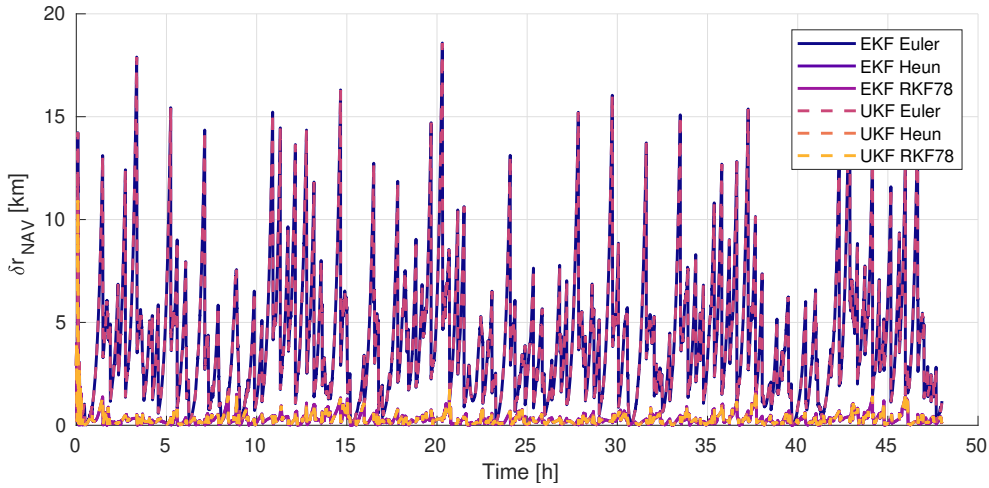

Figure 5.22: Evolution of the position navigation error for the six filters under study for the simulation time-span of 48 h.

computer as reasonable target hardware. The most relevant characteristics of such elements are reported in the following.

- Broadcom BCM2711 System on Chip (SoC)
- Quad-core Cortex-A72 ARM-based processor
- 64-bit architecture
- 1.5 GHz clock maximum frequency
- LPDDR4 SDRAM of 4 GB

With such features the Raspberry Pi 4 can be considered as a representative piece of hardware considering general on-board computer for medium to high size spacecraft, while they are quite high for CubeSat specific processors.

The *porting procedure* to embed the developed software on the Raspberry Pi board takes advantage of the autocoding features provided by the MATLAB/Simulink environment, following the general workflow exploited for the GNC flight software generation [101]. The Simulink Embedded Coder applicative provides a simple and reliable manner to generate ANSI C-code directly runnable on the specific hardware under test, i. e. the Raspberry Pi in this context.

Figure 5.23 represents the Simulink schematics employed to perform the validation and profiling of the auto-generated software. The filter under test, e. g. the EKF with Heun integration in he figure, runs parallelly on the Simulink desktop environment, representing the Model-In-the-Loop (MIL) simulation, and on the target hardware in PIL mode. Both filter implementations receive the same

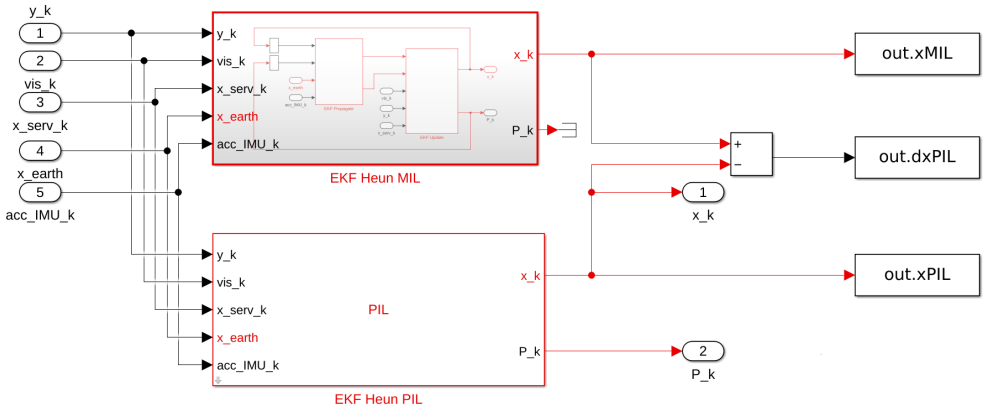

Figure 5.23: Simulink schematics of the MIL-PIL parallel simulation for the EKF filter with the Heun propagation.

inputs from the simulation of the real world dynamics, while the outputs of the PIL filter only are fed back to the real world simulator. By running the two models in parallel with the same inputs it is possible to correlate directly the execution errors of the PIL implementation and validate the autocoding procedure, while recording also the profiling statistics.

All the filters have been run singularly on the embedded environment for a simulated time of 10h and the performance and execution times have been recorded. Figure 5.24 represent the evolution of the position and velocity x-components and the clock bias relative errors between the PIL and MIL simulations, defined for a generic quantity w as $\varepsilon_w = (w_{\text{MIL}} - w_{\text{PIL}})/w_{\text{MIL}}$. The relative errors are plotted alongside the total number of satellite in visibility. From the plots it is possible to see that the relative errors are in general always negligible, with values for the position and velocity errors in the order of 10^{-8} for most of the simulation time, except some isolated spikes in the order of 10^{-4} during the blind windows, where the filter is only propagating the state. Values are slightly higher for the clock bias, but not providing any complexity in the overall estimation procedure. The evolution of the navigation errors are practically identical both in trend and statistics.

Looking at the profiling analysis, Fig. 5.25 reports the box-plot of the execution times for a single filter step for the six compared cases. As expected, we can see that each integration method in the EKF formulation compared to the associated UKF one is faster, with a particular speed increment for the RKF78 case, where a factor of more than $5\times$ is present among the two. Also, we can see that a relevant time gain is obtained between the RKF78 and the Heun case, which, provides the exact same performance. Additionally, we may see that the cost increment passing from the Euler method to the Heun one is very reduced.

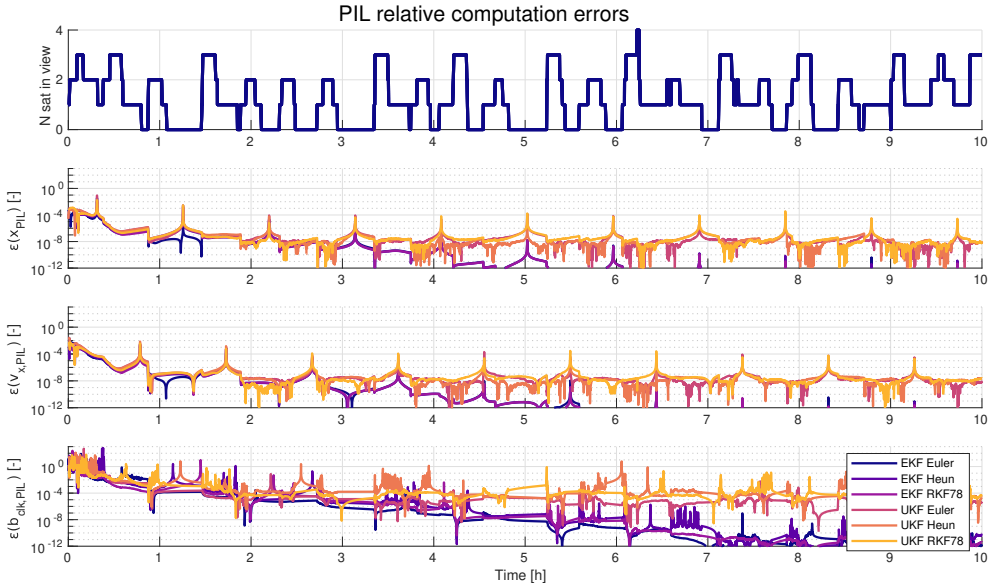

Figure 5.24: Time evolution of the relative errors between the PIL filter outputs and the MIL ones, plotted along with the total number of satellite in visibility. Position and velocity x-components and clock bias relative errors are plotted.

By looking at the absolute values of the execution time for the filters, the worst case of the UKF-RKF78 couple reports a single step time of 0.5 ms. Considering also a worst case of the filter execution frequency of 10 Hz, the associated duty-cycle is about 0.5%, which is perfectly compliant with the execution of the task without incurring in computational time saturation, thus validating the feasibility of employing these algorithms safely.

All these PIL analyses prove that the EKF-Heun filter-propagation couple is the most suited one for such application, providing the second best speed performance at equal navigation error with respect to the other more computationally demanding counterparts.

5.5 Closing Remarks

This chapter presented a complete framework for supporting the preliminary phase design of a satellite constellation to provide communication and navigation services to both South Pole and Low Lunar Orbit users. The developed system is capable to provide the flexibility requested by such early stages of the mission analysis, where the overall requirements are not completely defining a specific performance index. In such cases, exploiting Multi Objective Optimisation (MOO) is a good choice to combine different objectives which

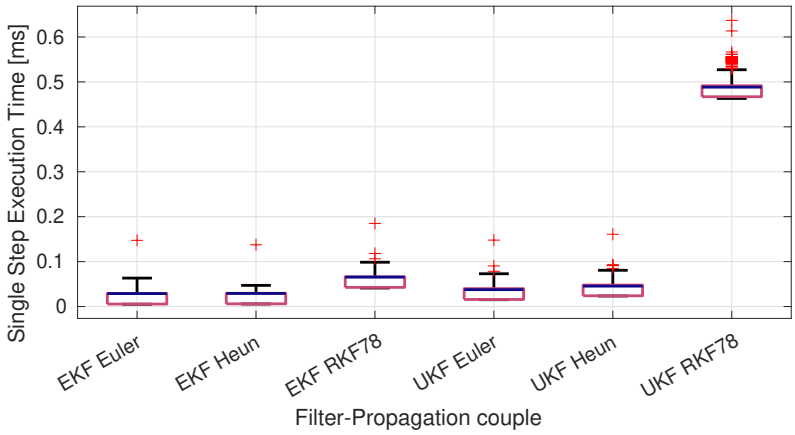

Figure 5.25: Box-plot indicating execution time of a single step for the navigation filter in the different filter-propagation couples.

may be clashing among themselves or may be uninfluenced. Moreover, such multi-objective scheme outputs a whole population of solutions, a subset of which represents usually a Pareto front, from which we can understand the boundaries of feasibility and then pick the solutions that fit our needs the most.

The optimisation has been exploited to cast together objectives associated to either the surface users or the LLO ones. In particular three different cost functions are taken into consideration with or without the South Pole related objectives, each one run for three different constellation sizes. The resulting populations of solutions have been inspected through various Pareto plots and a total of 16 possible candidates are extracted with optimal related performance.

A subset of these candidates has been then analysed in terms of the navigation performance, when simulated with an LLO polar user at an altitude of 50 km at `ran` values of 0 and 90°. The navigation filter employed here considers a tightly coupled GNSS/INS formulation, where the servicers pseudorange and pseudorange-rate measurements are fused to the ones of an accelerometer. The presented architecture provided an alternating behaviour of regions with extremely good performance in state reconstruction and regions of loss of GNSS support, where the accelerometer inertial navigation starts loosing accuracy leading in some cases to acceptable levels (< 1 km) and unacceptable in some others (> 10 km). The comparison of the obtained navigation filter results correlated to cost function and constellation size provides some useful insights, such as the increment in performance looking at the minimisation of the combined position error average and standard deviation values, `LLO_musigma`, against the minimisation of cumulative 2-fold blind windows. Moreover the robustness of optimising for a wide variety of LLO users orbital plane has

been proved, by comparing the `llo_sgl` with `llo_mlt` cost functions. In the latter, even though lower performance are obtained in general for the optimised orbital planes, a higher resilience of the results is present when looking at non-optimised solutions for orbital planes.

The analyses highlighted also that the small benefits that the addition of optical measurements from the servicers are not worth the complexities required by such solution, providing practically a negligible estimation enhancement.

An additional scenario of a landing spacecraft has also been presented, whose GNC chain comprises also an offline optimised guidance to be used as setpoint for a reference tracking PID controller. The nominal results provide very good performance, with final navigation and control errors around 200 m and 400 m respectively. The following Monte-Carlo analysis provided a success rate of 64% considering a 3 km accuracy threshold in the horizontal plane at 1 km altitude. Such rate is acceptable, but it may be even increased with a precise start time scheduling, targetting precise high visibility windows.

The final analyses comparing the EKFs and UKFs with the different propagation methods provided the following remarks. The errors obtained with the simple Forward Euler method are not acceptable, while no difference was noted between the Heun and Runge-Kutta-Fehlberg 7(8) one. Moreover the EKFs and UKFs provided the same results, highlighting that the nonlinearities do not have a major impact in this scenario. After that the PIL tests were effective in validating the architecture from a hardware implementation point of view and providing the computational time profiling to perform a comparison. As expected the EKFs are faster than the UKFs, particularly for the RKF78 where the increment is higher than a factor of 5×. The Heun method was found to be not much slower than Euler one, but much faster than RKF78, resulting as a consequence the most suited implementation coupled with the EKF: it is the second best in speed, with the same performance of the most complex formulation.

CHAPTER 6

Conclusions

This final chapter tries to wrap up the results obtained through all the thesis works. The goal is to provide an overview of the advancements that this work made in the context of enhancing the autonomy of spacecraft to support the great exploration of the Moon which will invest the next decades of the space ecosystem. Such exploration roadmap entails, among others, two important infrastructures, that will help the operations to be performed in the lunar environment, supporting the both the scientific activities and the engineering demonstrations to advance in the future human stable outposts. These two infrastructures consist in the LOP-G and a GNSS constellation, the former developed to become a stable space station to host astronauts and to assist the future missions directed to the surface, the latter instead fundamental to provide the two major services of communication and navigation with much higher performance than those obtainable by un-aided users.

To exploit at their maximum these two huge projects, a deep understanding of the GNC algorithms needed for spacecraft to interoperate with these systems is necessary, in order to define the boundary of feasibility and of resource optimisation in which such spacecraft will move. In particular the navigation

task in scenarios of reduced observability is something that, if achieving good performance, can unlock many different mission concepts considering also smaller assets, which are generally equipped with limited sensor suites.

Recalling the questions that were posed in Chapter 1, after having presented the relevant analyses, it is possible here to provide the associated answers per each one of the three scenarios analysed.

In Scenario A, presented in Chapter 4, the problem of performing an autonomous rendezvous with a cooperative agent representing the LOP-G has been analysed. In this scenario the only sensor considered to be available to the chaser is an optical camera, able to retrieve LoS bearing-angles only. The concept of BO guidance and navigation that had been proposed and tested only in the simpler two-body LEO scenario has been proved also for the more dynamically complex non-Keplerian environment. The obtained navigation accuracies are driven below 1% of the relative range to the target, which means providing metres-level errors at the end of the rendezvous, perfectly compatible with a safe execution of the mission. The already presented quadratic formulation showed a behaviour that drives the spacecraft to force a range reduction, which is a not so good feature, considering that the relative range error drops below the threshold only near the end of the transfer. The proposed variation of employing a nonlinear constraint directly on the observability angle provides instead a much smoother relative distance reduction with a threshold crossing occurring much sooner in the transfer, providing a more effective alternative. The computational demand required by this modification is however increased by the introduction of this nonlinear term.
The additional investigation performed was to prove the concept of BO guidance in the scenario of heterogeneous orbits, where the imposition of performing a thrusting action that overall does not change the final resulting trajectory was posed to enhance the state observability. This scenario proved to be effective, providing a relative range navigation error less than 1%, consisting to the order of less than 100 km in the cases considered. A performance deterioration is however caused by linearisation of the dynamics employed in the filter, which is accurate for small ratios between the chaser-target distance and the target-Moon distance. The test cases analysed showed that a ratio higher than 10% prevents a stable navigation error.

The second scenario investigated the best GNC strategy to accomplish rephasing manoeuvres in the proximity of the LOP-G as well, but keeping a bounded motion with respect to it. The analysis conducted, defined the guidance and control strategy as a reference tracking problem, where the target trajectory to be followed has been expressed as the interpolation of precomputed relative trajectories defined as belonging to Quasi Periodic Tori. The most suitable G&C formulation for this problem has been deemed the receding-horizon MPC

strategy, which is able to foresee the dynamics evolution in a short enough window to adapt correctly to the environment and yet remaining relatively computationally light. A relevant addition of the overall algorithm has been done by employing an updating weight tuning approach, in order to provide a more flexible and adaptive scheme, that can be exploited for many different transfers within this framework. Additionally, the capability of the MPC to entail constraints in its optimisation step, increases its versatility, which has been proved by the inclusion of maximum thrust value and collision avoidance. After that the capability of the BO strategy to keep a navigation performance within the identified requirements was investigated. Unfortunately, in this scenario the BO guidance was found to be ineffective, since the required transfer geometry already drove the observability angle to its optimal value in the middle of the transfer. The BO guidance is not acting in this scenario and the exact same results are obtained without including it in the MPC. Introducing instead radiometric data, range first and also Doppler afterwards, the capability to finalise the transfer is recovered, obtaining a navigation error down to around 1 km in the best condition.

Finally the last scenario was useful to prove the concept of employing MOO procedure to design a GNSS constellation around the Moon, to serve both surface and LLO users. Different constellation sizes and objective functions have been considered and their results compared. In particular the test of these navigation concept in the filter implemented for the orbital users showed a common behaviour of the different optimisation solutions. The continuous alternation of windows with visibility and blind ones, provided an oscillation of the navigation errors even below 100 m to slightly above 1 km in the blind windows where the propagation is performed assisted only by the IMU measurements. Overall these performance is acceptable if stringent errors are needed for reduced windows (e. g. roughly < 1 h). The investigation of adding optical measurements proved instead that even in the most favourable condition (thus more demanding from a platform implementation point of view) the increments in the performance were not relevant to justify the added complexity.
The utilisation of these filtering and navigation strategy was proved also on a landing scenario, where the full GNC chain is under test. In the analysed case, considering a low visibility window, very good results are obtained with final control errors around 400 m, reducing down to less than 200 m under good visibility conditions. A Monte-Carlo in the reduced visibility conditions highlighted that around 65% of the tested cases obtained a final control error lower than 3 km, considered an acceptable rate, which may be increased with a precise start time scheduling, targetting precise high visibility windows. When comparing different filter algorithm–propagation couples, the EKF with a Heun integration scheme stood-out as the most suitable formulation, second best in speed and equivalent in performance to the more complex RKF78 propagation.

Finally, the proposed navigation algorithms have been tested and validated in embedded hardware, providing no relevant downsides in the execution time also for more complex filtering techniques.

The initially posed research question can be considered to be only partially answered. Indeed, first of all, the analysed techniques do not cover all the scenarios where spacecraft may be operating autonomously from Earth in reduced observability conditions. As such obviously the presented research approaches only a small part of the global problem under investigation. Secondly, also within the proposed scenarios there are possible research extension to consolidate even more the approaches.

In particular for the BO technique, the performed analysis considered directly the availability of the optical angles Az and El. However, as also pointed out in Chapter 3, the optical observable is obtained as output of a large processing procedure, which has the role of identifying the target on the camera and translate its pixel coordinates in the camera frame into the two angles. This process includes thus both IP techniques and attitude estimation steps, which are not included in this research work. An interesting future work may entail a more advanced implementation of the whole processing chain, including a complete 6DOF GNC loop and the inclusion of the IP techniques or at least a performance model of its application.
In addition, this promising technique may be investigated also in different conditions, in another environment or mission scenario, to enlarge even more its application region.

In the GNSS scenario instead the number of possible study extension is even larger. First of all, a formalisation of the MOO problem with a different set of cost function can lead to even more performing constellations. Another interesting aspect to analyse may consider an inter-operability of this constellation with the LOP-G, adding it to the set of available servicers. It is possible that its specific location in the cislunar space may serve as a sort of beacon which remains visible to a very wide space volume for much longer periods as the faster orbiting ELFO satellites.
From the filter implementation point of view, in order to provide an even higher fidelity to the scenario, it could be possible to entail more accurate accelerometer models in the simulation framework and adding also its bias and drift in the filter state to be estimated. If then, also in this case the 6DOF GNC is fully introduced, the same precise modelling may be used also for the gyroscope. Concerning the attitude profile, it could be useful to consider a specific attitude guidance for the user to maximise the visibility of the servicers, and thus to increase the duration of the visibility windows, still keeping some possible pointing constraints, such as nadir pointing of a certain face or Sun pointing.

Concerning the GNC validation through embedded PIL testing, the proposed analyses considered just the navigation filter to be tested, in order to provide a comparison medium for the different formulations investigated. However validating the complete GNC loop could increase even more the reliability of the proposed algorithms in all the three scenarios. Moreover, as already pointed out in Chapter 5, the Raspberry Pi is quite a powerful Single Board Computer related to the space domain, in particular if looking at the CubeSat family. As such the execution of such validation tests on less performing hardware could provide an additional solidity to the proposed GNC scheme also for small-sized systems.

Bibliography

[1] F Scala *et al.*, "The hermes mission: A cubesat constellation for multi-messenger astrophysics", in *5th IAA Conference on University Satellite Missions and CubeSat Workshop*, vol. 173, 2020, pp. 57–73.

[2] V. Kapila, A. Sparks, J. Buffington, and Q. Yan, "Spacecraft formation flying: Dynamics and control", English (US), *Journal of Guidance, Control, and Dynamics*, vol. 23, no. 3, pp. 561–564, 2000, ISSN: 0731-5090. DOI: 10.2514/2.4567.

[3] W. Wang, C. Li, and Y. Guo, "Relative position coordinated control for spacecraft formation flying with obstacle/collision avoidance", *Nonlinear Dynamics*, vol. 104, no. 2, pp. 1329–1342, 2021. DOI: https://doi.org/10.1007/s11071-021-06348-9.

[4] S. Silvestrini and M. Lavagna, "Neural-aided gnc reconfiguration algorithm for distributed space system: Development and pil test", *Advances in Space Research*, vol. 67, no. 5, pp. 1490–1505, 2021, ISSN: 0273-1177. DOI: https://doi.org/10.1016/j.asr.2020.12.014.

[5] K. Coderre *et al.*, "Concept of operations for the gateway", in *Space Operations: Inspiring Humankind's Future*, H. Pasquier, C. A. Cruzen, M. Schmidhuber, and Y. H. Lee, Eds., Cham: Springer International Publishing, 2019, pp. 63–82. DOI: 10.1007/978-3-030-11536-4_4.

[6] R. Whitley and R. Martinez, "Options for staging orbits in cislunar space", in *2016 IEEE Aerospace Conference*, IEEE, 2016, pp. 1–9.

[7] C. R. Short and K. C. Howell, "Lagrangian coherent structures in various map representations for application to multi-body gravitational regimes", *Acta Astronautica*, vol. 94, no. 2, pp. 592–607, 2014, ISSN: 0094-5765. DOI: https://doi.org/10.1016/j.actaastro.2013.08.020.

[8] G Zanotti and M Lavagna, "Science opportunities in the Didymos binary: The role of post-impact ejecta long-term dynamics in the proximity operations definition", in *71st International Astronautical Congress (IAC 2020)*, 2020, pp. 1–15.

[9] F. Ferrari and M. Lavagna, "Periodic motion around libration points in the elliptic restricted three-body problem", *Nonlinear Dynamics*, vol. 93, no. 2, pp. 453–462, 2018. DOI: https://doi.org/10.1007/s11071-018-4203-4.

[10] A. Colagrossi and M. Lavagna, "Dynamical analysis of rendezvous and docking with very large space infrastructures in non-keplerian orbits", *CEAS Space Journal*, vol. 10, no. 1, pp. 87–99, 2018. DOI: https://doi.org/10.1007/s12567-017-0174-4.

[11] A. Colagrossi, V. Pesce, L. Bucci, F. Colombi, and M. Lavagna, "Guidance, navigation and control for 6dof rendezvous in cislunar multi-body environment", *Aerospace Science and Technology*, vol. 114, p. 106 751, 2021, ISSN: 1270-9638. DOI: https://doi.org/10.1016/j.ast.2021.106751.

[12] V. Muralidharan *et al.*, "Hardware-in-the-loop proximity operations in cislunar space", *Proceedings of the International Astronautical Congress, IAC-2022*, 2022.

[13] K. C. Laurini *et al.*, "An international strategy for human exploration of the moon: The international space exploration coordination group (ISECG) reference architecture for human lunar exploration", in *Proceedings of the 61st International Astronautical Congress*, International Astronautical Federation (IAF) Paris, 2010, pp. 1–9.

[14] D. E. Wilhelms, K. A. Howard, and H. G. Wilshire, *Geologic map of the south side of the Moon*. Department of the Interior, US Geological Survey, 1979.

[15] J. Flahaut *et al.*, "Regions of interest (ROI) for future exploration missions to the lunar south pole", *Planetary and Space Science*, vol. 180, p. 104 750, 2020.

[16] J. J. Parker *et al.*, "The lunar gnss receiver experiment (lugre)", in *Proceedings of the 2022 International Technical Meeting of The Institute of Navigation*, 2022, pp. 420–437. DOI: 10.33012/2022.18199.

[17] G. Impresario, G. D'Amore, C. Stallo, L. Ansalone, and A. Tuozzi, "Gnss and galileo for cis-lunar and moon navigation", in *2018 IEEE 4th International Forum on Research and Technology for Society and Industry (RTSI)*, 2018, pp. 1–5. DOI: 10.1109/RTSI.2018.8548504.

[18] E. Mikrin, M. Mikhailov, I. Orlovskii, S. Rozhkov, and I. Krasnopol'skii, "Satellite navigation of lunar orbiting spacecraft and objects on the lunar surface", *Gyroscopy and Navigation*, vol. 10, no. 2, pp. 54–61, 2019.

[19] E. E. Zini, "Precise orbit determination techniques for a lunar satellite navigation system", Ph.D. Dissertation, Ph. D. dissertation, Politecnico di Torino, 2021.

[20] D. C. Woffinden and D. K. Geller, "Optimal orbital rendezvous maneuvering for angles-only navigation", *Journal of guidance, control, and dynamics*, vol. 32, no. 4, pp. 1382–1387, 2009.

[21] J. Grzymisch and W. Fichter, "Optimal rendezvous guidance with enhanced bearings-only observability", *Journal of Guidance, Control, and Dynamics*, vol. 38, no. 6, pp. 1131–1140, 2015.

[22] C. H. Acton Jr, "Ancillary data services of NASA's navigation and ancillary information facility", *Planetary and Space Science*, vol. 44, no. 1, pp. 65–70, 1996.

[23] V. Szebehely, *Theory of orbits: the restricted problem of three bodies*. Yale univ New Haven CT, 1967, ISBN: 978-0-12-395732-0. DOI: 10.1016/B978-0-12-395732-0.X5001-6.

[24] W. MacMillan, *The Theory of the Potential*. McGraw-Hill book Company, Inc., 1930.

[25] H. Schaub and J. L. Junkins, *Analytical mechanics of space systems*. American Institute of Aeronautics and Astronautics, 2005.

[26] A. Pasquale, S. Silvestrini, A. Capannolo, P. Lunghi, and M. Lavagna, "Small bodies non-uniform gravity field on-board learning through hopfield neural networks", *Planetary and Space Science*, p. 105 425, 2022.

[27] R. A. Werner and D. J. Scheeres, "Exterior gravitation of a polyhedron derived and compared with harmonic and mascon gravitation representations of asteroid 4769 castalia", *Celestial Mechanics and Dynamical Astronomy*, vol. 65, no. 3, pp. 313–344, 1996.

[28] A. Capannolo, "Nanosatellites formation flying in binary asteroids systems", M.S. thesis, Politecnico di Milano, Dipartimento di Scienze e Tecnologie Aerospaziali, Milano, Italy, 2016.

[29] D. A. Vallado, *Fundamentals of astrodynamics and applications*. Springer Science & Business Media, 2001, vol. 12.

[30] L. Bucci, A Colagrossi, and M. Lavagna, "Rendezvous in lunar near rectilinear halo orbits", *Advances in Astronautics Science and Technology*, vol. 1, no. 1, pp. 39–43, 2018.

[31] V. Pesce, A. Colagrossi, and S. Silvestrini, *Modern Spacecraft Guidance, Navigation, and Control, From System Modeling to AI and Innovative Applications*, 1st ed. Elsevier, 2022, ISBN: 9780323909167.

[32] M. Lombardo *et al.*, "Design and analysis of the cis-lunar navigation for the argomoon cubesat mission", *Aerospace*, vol. 9, no. 11, 2022, ISSN: 2226-4310. DOI: 10.3390/aerospace9110659.

[33] E. Dotto *et al.*, "Liciacube - the light italian cubesat for imaging of asteroids in support of the nasa dart mission towards asteroid (65803)

didymos", *Planetary and Space Science*, vol. 199, p. 105 185, 2021, ISSN: 0032-0633. DOI: https://doi.org/10.1016/j.pss.2021.105185.

[34] A. Capannolo *et al.*, "Challenges in licia cubesat trajectory design to support dart mission science", *Acta Astronautica*, vol. 182, pp. 208–218, 2021, ISSN: 0094-5765. DOI: https://doi.org/10.1016/j.actaastro.2020.09.023.

[35] P. Antreasian *et al.*, "Orbit determination processes for the navigation of the cassini-huygens mission", in *SpaceOps 2008 Conference*. DOI: 10.2514/6.2008-3433. eprint: https://arc.aiaa.org/doi/pdf/10.2514/6.2008-3433.

[36] K. D. Hicks and W. E. Wiesel, "Autonomous orbit determination system for earth satellites", *Journal of Guidance, Control, and Dynamics*, vol. 15, no. 3, pp. 562–566, 1992. DOI: 10.2514/3.20876.

[37] J. Yim, J. Crassidis, and J. Junkins, "Autonomous orbit navigation of interplanetary spacecraft", in *Astrodynamics Specialist Conference*, 2000, p. 3936.

[38] H. Jung and M. L. Psiaki, "Tests of magnetometer/sun-sensor orbit determination using flight data", *Journal of Guidance, Control, and Dynamics*, vol. 25, no. 3, pp. 582–590, 2002. DOI: 10.2514/2.4920.

[39] S. I. Sheikh, D. J. Pines, P. S. Ray, K. S. Wood, M. N. Lovellette, and M. T. Wolff, "Spacecraft navigation using x-ray pulsars", *Journal of Guidance, Control, and Dynamics*, vol. 29, no. 1, pp. 49–63, 2006. DOI: 10.2514/1.13331. eprint: https://doi.org/10.2514/1.13331.

[40] R. Raymond Karimi and D. Mortari, "Interplanetary autonomous navigation using visible planets", *Journal of Guidance, Control, and Dynamics*, vol. 38, no. 6, pp. 1151–1156, 2015. DOI: 10.2514/1.G000575. eprint: https://doi.org/10.2514/1.G000575.

[41] K. Hill and G. H. Born, "Autonomous interplanetary orbit determination using satellite-to-satellite tracking", *Journal of Guidance, Control, and Dynamics*, vol. 30, no. 3, pp. 679–686, 2007. DOI: 10.2514/1.24574. eprint: https://doi.org/10.2514/1.24574.

[42] D Barberi Spirito and M Lavagna, "Mars-phobos multi-body regime exploitation for martian navigation light constellation design", in *SpaceOps 2021 Virtual Edition-16th International Conference on Space Operations*, 2021, pp. 1–20.

[43] D. Barberi Spirito, "Martian assets navigation service through Mars-Phobos multi-body regime exploitation for constellation design", M.S. thesis, Politecnico di Milano, Dipartimento di Scienze e Tecnologie Aerospaziali, Milano, Italy, 2021.

[44] S. G. Hesar, J. S. Parker, J. M. Leonard, R. M. McGranaghan, and G. H. Born, "Lunar far side surface navigation using linked autonomous interplanetary satellite orbit navigation (liaison)", *Acta Astronautica*,

vol. 117, pp. 116–129, 2015, ISSN: 0094-5765. DOI: https://doi.org/10.1016/j.actaastro.2015.07.027.

[45] S. Silvestrini *et al.*, "Optical navigation for lunar landing based on convolutional neural network crater detector", *Aerospace Science and Technology*, vol. 123, p. 107 503, 2022.

[46] S. Silvestrini, M. Piccinin, G. Zanotti, A. Brandonisio, P. Lunghi, and M. Lavagna, "Implicit extended kalman filter for optical terrain relative navigation using delayed measurements", *Aerospace*, vol. 9, no. 9, 2022, ISSN: 2226-4310. DOI: 10.3390/aerospace9090503.

[47] D. C. Woffinden and D. K. Geller, "Observability criteria for angles-only navigation", *IEEE Transactions on Aerospace and Electronic Systems*, vol. 45, no. 3, pp. 1194–1208, 2009.

[48] J. Grzymisch and W. Fichter, "Observability criteria and unobservable maneuvers for in-orbit bearings-only navigation", *Journal of Guidance, Control, and Dynamics*, vol. 37, no. 4, pp. 1250–1259, 2014.

[49] J. Grzymisch and W. Fichter, "Analytic optimal observability maneuvers for in-orbit bearings-only rendezvous", *Journal of Guidance, Control, and Dynamics*, vol. 37, no. 5, pp. 1658–1664, 2014. DOI: 10.2514/1.G000612.

[50] S. Mok, J. Pi, and H. Bang, "One-step rendezvous guidance for improving observability in bearings-only navigation", *Advances in Space Research*, vol. 66, no. 11, pp. 2689–2702, 2020.

[51] P Giordano *et al.*, "Moonlight navigation service-how to land on peaks of eternal light", in *Proceedings of the 72nd International Astronautical Congress*, 2021, pp. 1–14.

[52] A. Grenier *et al.*, "Positioning and velocity performance levels for a lunar lander using a dedicated lunar communication and navigation system", *NAVIGATION: Journal of the Institute of Navigation*, vol. 69, no. 2, 2022, ISSN: 0028-1522. DOI: 10.33012/navi.513. eprint: https://navi.ion.org/content/69/2/navi.513.full.pdf.

[53] H. Curtis, *Orbital mechanics for engineering students*. Butterworth-Heinemann, 2013.

[54] A. Pasquale, G. Zanotti, J. Prinetto, M. Ceresoli, and M. Lavagna, "Cislunar distributed architectures for communication and navigation services of lunar assets", *Acta Astronautica*, 2022, ISSN: 0094-5765. DOI: https://doi.org/10.1016/j.actaastro.2022.06.004.

[55] E. D. Kaplan and C. Hegarty, *Understanding GPS/GNSS: principles and applications*. Artech house, 2017.

[56] B. D. O. Anderson and J. B. Moore, *Optimal Control: Linear Quadratic Methods*. USA: Prentice-Hall, Inc., 1990, ISBN: 0136385605.

[57] P. Montagnier, R. J. Spiteri, and J. Angeles, "The control of linear time-periodic systems using floquet–lyapunov theory", *International Journal of Control*, vol. 77, no. 5, pp. 472–490, 2004.

[58] Y. Lian, G. Gómez, J. J. Masdemont, and G. Tang, "Station-keeping of real earth–moon libration point orbits using discrete-time sliding mode control", *Communications in nonlinear science and numerical simulation*, vol. 19, no. 10, pp. 3792–3807, 2014.

[59] K. M. Drozd, R. Furfaro, and F. Topputo, "Application of zem/zev guidance for closed-loop transfer in the earth-moon system", in *2018 Space Flight Mechanics Meeting*. DOI: 10.2514/6.2018-0958.

[60] T. Çimen, "State-dependent riccati equation (sdre) control: A survey", *IFAC Proceedings Volumes*, vol. 41, no. 2, pp. 3761–3775, 2008.

[61] E. F. Camacho and C. Bordons, "Introduction to model predictive control", in *Model Predictive control*, London: Springer London, 2007, pp. 1–11. DOI: 10.1007/978-0-85729-398-5_1.

[62] F. Gavilan, R. Vazquez, and E. F. Camacho, "An iterative model predictive control algorithm for uav guidance", *IEEE Transactions on Aerospace and Electronic Systems*, vol. 51, no. 3, pp. 2406–2419, 2015. DOI: 10.1109/TAES.2015.140153.

[63] R. Vazquez, F. Gavilan, and E. F. Camacho, "Model predictive control for spacecraft rendezvous in elliptical orbits with on/off thrusters", *IFAC-PapersOnLine*, vol. 48, no. 9, pp. 251–256, 2015, ISSN: 2405-8963. DOI: https://doi.org/10.1016/j.ifacol.2015.08.092.

[64] S. Silvestrini, J. Prinetto, G. Zanotti, and M. Lavagna, "Design of robust passively safe relative trajectories for uncooperative debris imaging in preparation to removal", in *2020 AAS/AIAA Astrodynamics Specialist Conference*, Virtual Lake Tahoe, United States, 2020, pp. 1–18.

[65] R. E. Kalman, "A New Approach to Linear Filtering and Prediction Problems", *Journal of Basic Engineering*, vol. 82, no. 1, pp. 35–45, Mar. 1960, ISSN: 0021-9223. DOI: 10.1115/1.3662552. eprint: https://asmedigitalcollection.asme.org/fluidsengineering/article-pdf/82/1/35/5518977/35_1.pdf.

[66] U. Spagnolini, *Statistical Signal Processing in Engineering*. John Wiley & Sons, 2018, ISBN: 978-1-119-29397-2.

[67] E. A. Wan and R. van der Merwe, "The unscented kalman filter", in *Kalman Filtering and Neural Networks*. John Wiley & Sons, Ltd, 2001, ch. 7, pp. 221–280, ISBN: 9780471221548. DOI: https://doi.org/10.1002/0471221546.ch7. eprint: https://onlinelibrary.wiley.com/doi/pdf/10.1002/0471221546.ch7.

[68] E. Wan and R. Van Der Merwe, "The unscented kalman filter for nonlinear estimation", in *Proceedings of the IEEE 2000 Adaptive Systems for Signal Processing, Communications, and Control Symposium (Cat. No.00EX373)*, 2000, pp. 153–158. DOI: 10.1109/ASSPCC.2000.882463.

[69] J. R. Carpenter and C. N. D'Souza, "Navigation filter best practices", Tech. Rep., 2018.

[70] J. L. Crassidis and J. L. Junkins, *Optimal estimation of dynamic systems*. Chapman & Hall/CRC, London, 2004, ISBN: 1-58488-391-X.

[71] F. L. Markley and J. L. Crassidis, *Fundamentals of spacecraft attitude determination and control*. Springer, 2014, vol. 1286, ISBN: 978-1-4939-0801-1.

[72] P. Lunghi, M. Lavagna, and R. Armellin, "A semi-analytical guidance algorithm for autonomous landing", *Advances in Space Research*, vol. 55, no. 11, pp. 2719–2738, 2015, ISSN: 0273-1177. DOI: https://doi.org/10.1016/j.asr.2015.02.022.

[73] D. Grebow, "Generating periodic orbits in the circular restricted three-body problem with applications to lunar south pole coverage", *MSAA Thesis, School of Aeronautics and Astronautics, Purdue University*, pp. 8–14, 2006.

[74] S. Silvestrini, J. Prinetto, G. Zanotti, and M. Lavagna, "Design of robust passively safe relative trajectories for uncooperative debris imaging in preparation to removal", in *2020 AAS/AIAA Astrodynamics Specialist Conference*, Virtual Lake Tahoe, United States, 2020, pp. 1–18.

[75] Hartley, Edward N, "A tutorial on model predictive control for spacecraft rendezvous", in *2015 European Control Conference (ECC)*, IEEE, 2015.

[76] A. Colagrossi and M. Lavagna, "Cislunar non-keplerian orbits rendezvous & docking: 6dof guidance and control", in *69th International Astronautical Congress (IAC 2018)*, International Astronautical Federation, IAF, Bremen, Germany, 2018, pp. 1–18.

[77] M. Ceresoli, G. Zanotti, and M. Lavagna, "Bearing-only navigation to support proximity operations on cislunar non-keplerian orbits", in *SpaceOps 2021 Virtual Edition-16th International Conference on Space Operations*, 2021, pp. 1–16.

[78] K. C. Howell and H. J. Pernicka, "Numerical determination of lissajous trajectories in the restricted three-body problem", *Celestial mechanics*, vol. 41, no. 1, pp. 107–124, 1987. DOI: https://doi.org/10.1007/BF01238756.

[79] A Capannolo, A Pasquale, and M Lavagna, "High-order polynomial continuation method for trajectory design in non-keplerian environments", *Celestial Mechanics and Dynamical Astronomy*, vol. 133, no. 10, pp. 1–21, 2021. DOI: https://doi.org/10.1007/s10569-021-10046-4.

[80] Z. P. Olikara, "Computation of quasi-periodic tori in the circular restricted three-body problem", Ph.D. Dissertation, Purdue University, 2010.

[81] Z. P. Olikara and D. J. Scheeres, "Numerical method for computing quasi-periodic orbits and their stability in the restricted three-body problem", *Advances in the Astronautical Sciences*, vol. 145, no. 911-930, 2012.

[82] N. Baresi, Z. P. Olikara, and D. J. Scheeres, "Fully numerical methods for continuing families of quasi-periodic invariant tori in astrodynamics", *The Journal of the Astronautical Sciences*, vol. 65, no. 2, pp. 157–182, 2018. DOI: https://doi.org/10.1007/s40295-017-0124-6.

[83] A. Capannolo and M. Lavagna, "Minimum cost relative dynamics in cislunar environment", in *Proceedings of the 71st International Astronautical Congress*, 2020, pp. 1–11.

[84] P. Berthe, A. P. Over, M. Gronowski, and B. Richard, "Orion european service module (esm) development, integration and qualification status", in *2018 AIAA SPACE and Astronautics Forum and Exposition*. DOI: 10.2514/6.2018-5146.

[85] A. Mannava, S. N. Balakrishnan, L. Tang, and R. G. Landers, "Optimal tracking control of motion systems", *IEEE Transactions on Control Systems Technology*, vol. 20, no. 6, pp. 1548–1558, 2012. DOI: 10.1109/TCST.2011.2168608.

[86] S. Strano and M. Terzo, "A sdre-based tracking control for a hydraulic actuation system", *Mechanical Systems and Signal Processing*, vol. 60-61, pp. 715–726, 2015, ISSN: 0888-3270. DOI: https://doi.org/10.1016/j.ymssp.2015.01.027.

[87] B Chachuat, "Nonlinear and dynamic optimization", *From Theory to Practice, Laboratoire dmAutomatique, Ecole Polytechnique Federale de Lausanne*, 2007.

[88] D. Morgan, S. J. Chung, and F. Y. Hadaegh, "Model predictive control of swarms of spacecraft using sequential convex programming", *Journal of Guidance, Control, and Dynamics*, vol. 37, no. 6, pp. 1725–1740, 2014, ISSN: 15333884. DOI: 10.2514/1.G000218.

[89] A. Capannolo and M. Lavagna, "Adaptive state-dependent riccati equation control for formation reconfiguration in cislunar space", *Journal of Guidance, Control, and Dynamics*, vol. 45, no. 5, pp. 982–989, 2022. DOI: 10.2514/1.G006540.

[90] T. Nie and P. Gurfil, "Lunar frozen orbits revisited", *Celestial Mechanics and Dynamical Astronomy*, vol. 130, no. 10, pp. 1–35, 2018.

[91] G. Acciarini, D. Izzo, and E. Mooij, "MHACO: A multi-objective hypervolume-based ant colony optimizer for space trajectory optimization", in *2020 IEEE Congress on Evolutionary Computation (CEC)*, 2020, pp. 1–8. DOI: 10.1109/CEC48606.2020.9185694.

[92] F. Biscani and D. Izzo, "A parallel global multiobjective framework for optimization: Pagmo", *Journal of Open Source Software*, vol. 5, no. 53, p. 2338, 2020. DOI: 10.21105/joss.02338.

[93] X. Li, "A non-dominated sorting particle swarm optimizer for multiobjective optimization", in *Genetic and Evolutionary Computation — GECCO 2003*, E. Cantú-Paz *et al.*, Eds., Berlin, Heidelberg: Springer Berlin Heidelberg, 2003, pp. 37–48, ISBN: 978-3-540-45105-1.

[94] K. Deb, A. Pratap, S. Agarwal, and T. Meyarivan, "A fast and elitist multiobjective genetic algorithm: NSGA-II", *IEEE transactions on evolutionary computation*, vol. 6, no. 2, pp. 182–197, 2002.

[95] A. S. Konopliv, A. B. Binder, L. L. Hood, A. B. Kucinskas, W. L. Sjogren, and J. G. Williams, "Improved gravity field of the moon from lunar prospector", *Science*, vol. 281, no. 5382, pp. 1476–1480, 1998. DOI: 10.1126/science.281.5382.1476.

[96] G. Falco, M. Pini, and G. Marucco, "Loose and tight gnss/ins integrations: Comparison of performance assessed in real urban scenarios", *Sensors*, vol. 17, no. 2, p. 255, 2017.

[97] C. Pernechele, "Hyper hemispheric lens", *Opt. Express*, vol. 24, no. 5, pp. 5014–5019, 2016. DOI: 10.1364/OE.24.005014.

[98] C. Pernechele *et al.*, "Hyper hemispheric lens applications in small and micro satellites", *Advances in Space Research*, vol. 62, no. 12, pp. 3449–3461, 2018, Advances in Technologies, Missions and Applications of Small Satellites, ISSN: 0273-1177. DOI: https://doi.org/10.1016/j.asr.2018.02.025.

[99] P. Lunghi, P. Di Lizia, R. Armellin, and M. Lavagna, "Semi-analytical adaptive guidance computation for autonomous planetary landing", *Acta Astronautica*, vol. 195, pp. 265–275, 2022, ISSN: 0094-5765. DOI: https://doi.org/10.1016/j.actaastro.2022.03.005.

[100] K. J. Åström and R. M. Murray, *Feedback systems: an introduction for scientists and engineers*. Princeton university press, 2021.

[101] A Pellacani, M Graziano, and M Suatoni, "Design, development, validation and verification of gnc technologies", *EUCASS2019*, 2019.

Colophon

This thesis was typeset with LaTeX and BibTeX, using a typographical look-and-feel created by Giovanni Zanotti. The style was inspired by S. Silvestrini, A. Colagrossi, D.A. Dei Tos `PhD_Dis` and by J. Stevens, L. Fossati `phdthesis` styles.